Synthesis and Characterization of Multiband Neutral Radicals

by

Joanne Wong

A thesis
presented to the University of Waterloo
in fulfillment of the
thesis requirement for the degree of
Master of Science
in Chemistry

Waterloo, Ontario, Canada, 2014

Authors Declaration

I hereby declare that I am the sole author of this thesis. This is a true copy of the thesis, including any required final revision, as accepted by my examiners.

I understand that my thesis may be made electronically available to the public.

Abstract

The notion that an array of free radicals might behave like metallic sodium was first suggested by McCoy and Moore in 1911. While the hypothesis represents an important historical landmark, there are many synthetic challenges associated with designing a conductive radical, such as the high propensity for these materials to dimerize and thus quench the free spin. Considerable advances have been made to overcome spin-pairing, including incorporation of heteroatoms such as sulfur and nitrogen atoms. Over the last 20 years, the Oakley group has used thiazyl radicals as a building block for multifunctional materials. While the early frameworks possessed a high barrier to charge transport, *U*, trapping the materials in Mott insulating states, the development of resonance-stabilized oxobenzene-bridged bisdithiazolyl radicals has led to a significant decrease in *U*, and metallic conductivity under mild pressure have also been observed.

The focus of this thesis is on the design, synthesis, and characterization of new oxobenzene-bridged radicals, and the effects of pressure on these systems. One particularly interesting system is the prototypal-oxobenzene-bridged radical, in which compression from 0 – 13 GPa afforded two additional phases and a significant increase in conductivity, peaking at 2 S cm^{-1} at 6 GPa with a concomitant decrease in E_{act} to zero, consistent with formation of a metallic state. Density functional theory (DFT) calculations were used to probe the electronic structure of these oxobenzene-bridged radicals, and these revealed the multiband electronic structure which is the source of the superior physical properties of these materials compared to previous generations of thiazyl radicals.

The intrinsically low *U* values and diverse structural variety exhibited by these oxobenzene-bridged radicals prompted the study of other substituents at the basal site. Studies on the early monocyclic DTDA systems were explored in pursuit of structure-directing ligands which can alter the solid-state packing to improve the bandwidth *W*. To this end, a pyridyl moiety was incorporated onto the DTDA framework, in which molecular ribbons laced together laterally by S---N intermolecular contacts was observed. However, these radicals crystallize as diamagnetic dimers, and are insulators. Nevertheless, it was established that nitrogen can be used as a structure directing ligand. Consequently, incorporation of a pyridine-quinone core into the oxobenzene-bridged framework was pursued in hopes of generating a more tightly bound structure with improved bandwidth, *W*. While the synthesis of the radical was not achieved, a variety of new synthetic procedures and novel species were developed.

The last and most recent work involves the incorporation of a π-acceptor (i.e. NO_2) at the basal site of the oxobenzene-bridged framework, and the resulting material displays the lowest E_{cell} (*U*) = 0.45 V ever observed for a neutral radical. While this is still ongoing work, preliminary results on the synthesis,

crystallography, magnetic and conductive properties are presented. To date, two different solvated phases have been isolated (incorporating acetonitrile and proponitrile) and both have been characterized by single X-ray crystallography. Both phases show room temperature conductivities near 10^{-2} S cm^{-1}.

Acknowledgements

I would like to thank, first and foremost, my supervisor Richard Oakley, where my career as a chemist initially began after taking your second year inorganic class, which prompted me to switch into chemistry. You have provided endless support and guidance as a mentor and a friend since that very first day. Throughout the years, I especially enjoyed listening to the numerous “back-in-the-day” stories and life conversations, which meant a great deal to me.

I would also like to thank my coworkers, Aaron Mailman, Steve Winter, Kristina Lekin, Karinna Yu, Rob Claridge, Adrian Maclean and Adam Mihailov for all their help and encouragement, which have made this a very memorable experience.

I would also like to thank my supervisory committee, Prof. Holger Kleinke and Prof. Sonny Lee for being a part of this journey with me.

I would like to acknowledge our collaborators, Dr. Paul Dube (Brockhouse), and Dr. Muralee Murugesu (Ottawa) for magnetic measurements, Prof. John Tse (Saskatoon) and Prof Richard Secco for transport property measurements and Dr. Craig Robertson for crystallography. Thank you for your support and contributions.

I would also like to thank all of my family and friends for their support throughout my degree and in my life. Thank you to those who made an effort or pretended to understand what I was doing. I’d like to make a special mention to my dearest friend and confident, Carmen. Thank you for your unlimited support and encouragement even if you’re on the other side of the world.

In memory of my hamster.

Table of Contents

References

List of Tables

List of Captioned Figures

List of Abbreviations

6-31G(d,p)	a split valence plus polarization basis set
a	crystallographic unit cell axis; hyperfine coupling constants
AFM	antiferromagnetism
Å	Angstrom
Anal.	analysis
b	crystallographic unit cell axis
B3LYP	hybrid B3 including an HF exchange term and the LYP correlation functional
BEDT	*bis*(ethylenedithio)
br	broad (IR peak descriptor)
BSS	broken symmetry singlet
C	Curie constant
^{o}C	degree centigrade
c	crystallographic unit cell axis
calcd.	calculated
cm^{-1}	reciprocal centimeters
CT	charge transfer
CV	cyclic voltammetry
d	doublet (NMR peak descriptor)
D	dimensionality, as in 1D or 3D
DAC	diamond anvil cell
DCE	dichloroethane
DCM	dichloromethane
dec.	decomposition
deg	degrees
DFT	Density Functional Theory
DMFc	*bis*(pentamethylcyclopentadienyl)iron
DTA	dithiazolyl
DTDA	dithiadiazolyl
DSDA	diselenadiazolyl
$E_{1/2}$	half-wave potential
E_{act}	activation energy

EA	electron affinity
E_{cell}	peak to peak potential separation
EHT	Extended Hückel Theory
emu	electromagnetic unit
E_{pa}	anodic peak potential
E_{pc}	cathodic peak potential
EPR	electron paramagnetic resonance
ET	*bis*(ethylenedithio) tetrathiafulvalene
ESI	electrospray ionization
EtOH	ethanol
eV	electron volt
f	fraction of band filled
FM	ferromagnetism
g	gram
g	Landé factor (g-factor)
GPa	gigapascal, unit of pressure
GSAS	General Structure Analysis System
^{1}H	proton
h	hour
H	magnetic field
ΔH_{disp}	disproportionation enthalpy
ΔH_{diss}	bond dissociation enthalpy
HOAc	acetic acid
HOMO	highest occupied molecular orbital
Hz	Hertz
IP	ionization potential
IR	infrared
K	Kelvin
kJ	kilojoule
L	litre
LUMO	lowest unoccupied molecular orbital
M	molarity, magnetization
m	multiplet (NMR descriptor)

min	minute
MIT	metal-to-insulator transition
Me	methyl
MeCN	acetonitrile
MeOH	methanol
mL	millilitre
mmol	millimole
MO	molecular orbital
mol	mole
mp	melting point
MS	mass spectrometry
mT	millitesla
NMR	nuclear magnetic resonance
Oe	Oersted
OMFc	*bis*(tetramethylcyclopentadienyl)iron
OTf	triflate (trifluoromethanesulfonate) anion
param.	parameters
Ph	phenyl group
PLY	phenalenyl radical
ppm	parts per million
PXRD	powder X-ray diffraction
r	radius, van der Waals radius, distance (Å)
R	general substituent group
R	agreement index (crystallography)
rem	remanent
ref.	referenced
restr.	restraints
RIC	radical ion conductor
ROTf	alkyl triflate
R_p	agreement index- profile (crystallography)
RT	room temperature
R_w	weighted agreement index
s	strong (IR peak descriptor); singlet (NMR peak descriptor); second
S	Siemens ($1S = 1\Omega^{-1}$); singlet state

S	spin
S^2	overlap density integral
$<S>^2$	expectation value
SCE	saturated calomel electrode
SHMO	Simple Hückel Molecular Orbital Theory
SOMO	singly occupied molecular orbital
SMM	single molecule magnet
SIM	single ion magnet
t	triplet (NMR peak descriptor)
T	temperature; triplet state
T_c	Curie temperature
TCNQ	tetracyano-*p*-diquinomethane
TCNE	tetracyano ethylene
TDAE	tetrakis(dimethlyamino)ethylene
temp	temperature
TEMPO	2,2,6,6-tetramethylpiperidine-N-oxyl
TMPDA	N,N,N',N'-tetramethyl-*p*-phenylenediamine
T_N	Néel temperature
Torr	unit of pressure = 133.32 Pa
TMS	trimethylsilyl group
U	on-site Coulomb repulsion energy
V	Volt
V	volume
VB	valence bond
vs	very strong (IR peak descriptor)
vs	versus
vw	very weak (IR peak descriptor)
w	weak (IR peak descriptor)
W	bandwidth
wR_p	weighted agreement index - profile (powder crystallography)
x	Cartesian coordinate
y	Cartesian coordinate
Z	number of asymmetric units per unit cell
z	Cartesian coordinate

^{o}	degree
α	crystallographic axis angle; coulombic parameter
β	crystallographic axis angle; resonance parameter
γ	crystallographic axis angle
δ	chemical shift in ppm; mean separation of molecules in a slipped stack
μ	absorption correction
τ	angle between the mean plane of the heterocyclic backbone and the stacking axis
υ	frequency
ρ	electrical resistivity; spin density
σ	electric conductivity; orbital symmetry
σ_{RT}	room temperature conductivity
λ	wavelength
χ	magnetic susceptibility

Chapter 1

Introduction to Neutral Radicals as Conductors and Magnetic Materials

1.1 – Stable Radicals as Multifunctional Materials

Radicals, by definition, are open-shell molecular systems containing one or more unpaired electrons, making them thermally unstable and/or highly reactive intermediates in chemical reactions.[1] Molecular radicals tend to decompose *via* dimerization, hydrogen or alkyl abstraction, and redox reaction pathways. In the case of dimerization, the free spin is quenched affording diamagnetic dimers.

The degree of stability of a molecular radical can be classified into two categories: persistent radicals and stable radicals. Persistent radicals are those that cannot be isolated, but have sufficiently long half-lives due to steric crowding (kinetic control) allowing them to be viewed spectroscopically.[2] On the other hand, molecular radicals that can be isolated by conventional methods and stored for prolonged periods of time without further decomposition from oxygen and moisture are termed stable radicals. To date, in the last 20 years, design strategies for imparting stability have improved dramatically, as a result of which numerous families of stable radicals have been characterized,[3] which will be discussed in subsequent sections of this chapter.

The inherent properties associated with an unpaired electron present in radicals foster applications in numerous fields including spin labeling,[4] spin trapping,[5] electron paramagnetic resonance (EPR) imaging,[6] and living free radical polymerization catalysis.[7] They can also, in theory, display metallic properties associated with metals as quoted from McCoy and Moore[8] in 1911:

"*If the electron theory of the metallic state is as fundamental as it seems to be, there would be little reason to doubt that an aggregate of free radicals would be a body having metallic properties; for such a hypothetical body would be made up of radicals which, analogous to metallic atoms, could easily lose electrons.*"

In hindsight, this hypothesis provides great historical value, but there are many synthetic challenges that come with an array of free radicals, such as the high propensity for these materials to dimerize and quench the free spin. Considerable advances have been made to prevent the formation of covalently bonded dimers, but metallic conductivity requires a second criteria: the need for a conduction pathway. That is, electrons must be able to move freely across many radical sites, which can be understood within

the context of the Hopping Model of Conduction.[9] The mobility of an electron in the solid-state is a direct function of the Coulomb repulsion energy barrier *U*. For a half-filled (*f* = ½) system, such as [Li][TCNQ], migration of an electron to an adjacent orbital results in a doubly occupied site and thus a high energy barrier *U*, as seen in Figure 1.1a. These materials are trapped in Mott insulating ground states unless the solid-state bandwidth, *W*, is large enough to overcome this barrier. In many cases where the Mott insulating states prevails (*U* > *W*), a broad range of magnetic properties is observed between the localized unpaired electrons. In contrast, in a partially-filled system (*f* = ¼), the electrons can migrate freely onto adjacent empty orbitals, minimizing *U* (Figure 1.1b). One particular example is [NMP][TCNQ]$_2$, a 1:2 charge transfer salt where there is an electron for every 2 sites, affording a bandfilling of *f* = ¼ and a room temperature conductivity of $\sigma_{RT} \sim 10^6$ S cm^{-1}.[10]

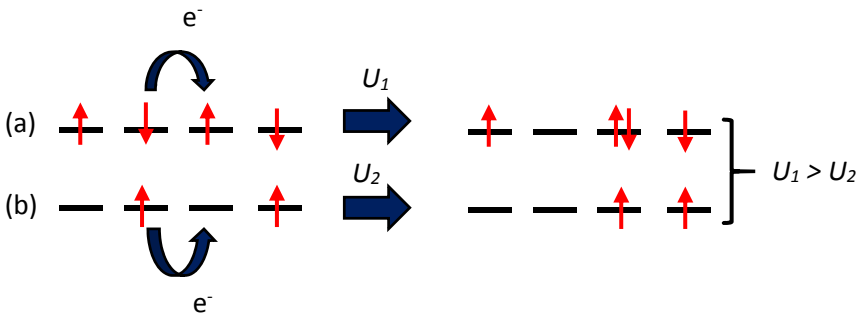

Figure 1.1 - On-site Coulomb repulsion energy (*U*) for a (a) *f* = ½ system and (b) *f* = ¼ system.

In the study of radical-based conductors, many years of research have been devoted to finding factors that affect both the bandwidth *W* and the barrier to electron transfer *U*. Recent developments by the Oakley group have breached the realm where *U* ~ *W*, marking the Mott insulator-to-metal transition. While this area remains to be completely understood in solid-state physics, it holds many technologically promising materials including high-temperature superconductors and colossal magnetoresistance materials. At a fundamental level, it is imperative to understand the unusual properties, as well as the design of these new materials for future synthetic targets. For this reason, the focus of this thesis will be on recent developments from the Oakley group on the design and characterization of new multifunctional heterocyclic radicals. However, prior to discussion of my graduate's work, I will provide a brief overview of theory relating to molecular magnetism and conductivity, followed by a historical review on stable radicals leading to thiazyl radicals.

1.2 – Principles of Conductivity & Magnetism

Magnetism originates from the interactions between localized electrons on atoms or molecules and their neighbouring centers. Two minimal requirements, unpaired electrons and a magnetic exchange pathway may give rise to numerous different types of magnetic communications including ferromagnetic (FM, ↑↑) and antiferromagnetic (AFM, ↑↓) interactions. With respect to the phenomenological Heisenberg[11] Hamiltonian given in equation **1**, *S* is the total spin operator and the coupling constant, *J,* is positive for ferromagnetic interactions and negative for antiferromagnetic coupling.

$$H_{ij} = -2J \sum_{ij} S_i S_j \tag{1}$$

The multiplicity of the ground state (singlet or triplet) is determined by the type and degree of orbital overlap defined by equation **2**, where strong orbital overlap ($S_{ab} \neq 0$) favours AFM coupling, while orthogonal overlap ($S_{ab} \cong 0$) typically suggests ferromagnetic interactions. All organic radicals are paramagnetic at ambient temperatures, that is, their spins are randomly oriented, but may display weak FM or AFM coupling at lower temperatures. These transition temperatures for ordered states are known as the Curie temperature, T_C, for FM coupling and the Néel temperature,T_N, for AFM coupling.

$$S_{ab} = \int \Phi_a^* \Phi_b \tag{2}$$

$$H = -\sum_{<ij>,\sigma} t_{i,j} C_{i,\sigma}^{\dagger} C_{j,\sigma} + U \sum_i n_{i,\uparrow} n_{i,\downarrow} \tag{3}$$

The Hubbard model described by a two term Hamiltonian given in equation **3**, can be used to understand molecular conductivity and magnetism. The first term represents the kinetic energy required for electrons to "hop" between adjacent orbitals typically referred to as the hopping integral, *t* (otherwise referred to as the resonance integral β). The second term symbolizes the Coulomb repulsion energy *U*, discussed in the previous section. In theory, a metallic state for a $f = ½$ system can be achieved if the hopping integral *t* is large and the Coulomb repulsion term *U* is small. In practice, however, many of these materials end up as Mott insulators, where the Coulomb repulsion energy dominates resulting in localization of the electrons. While conductivity is compromised, interesting magnetic behavior can be observed.

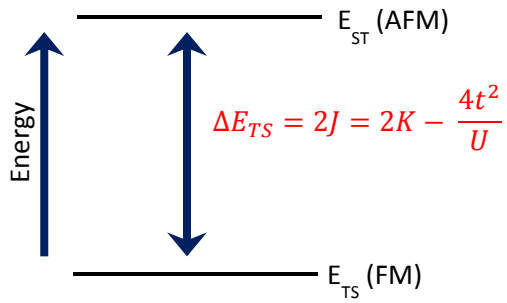

(4)

Figure 1.2 - Energy difference between the singlet (AFM) and triplet (FM) states.

Considering the Hubbard model in the limit of $U >> t$ for two sites, the ground stable multiplicity (triplet or singlet) can be determined using a simple two orbital model, where the singlet state (E_{ST}), with two electrons occupying the same site, are much higher in energy than the triplet states (E_{TS}). The energy gap between the singlet and triplet state is given in equation **4**, where *J* is the coupling constant, and K is the electronic exchange integral (**5**). Consequently, the magnitude of *K*, *t*, and *U* determine whether a material exhibits FM (+*J*) or AFM (-*J*) coupling.

$$K = \int \phi_1(1)\phi_2(2)(H')\phi_a(2)\phi_b(1)d\tau_1 d\tau_2 \tag{5}$$

Although one-dimensional and even two-dimensional FM ordering are commonly observed, long-range FM ordering in three-dimensions is rare and difficult to come by. The bulk magnetic susceptibility of a molecular material can be viewed as the sum of all the individual pairwise exchange interactions, *J*, which can be estimated using Density Functional Theory (DFT) methods.[12] For magnetically active organic radicals, we have employed the broken-symmetry singlet method,[13] which bypasses the need to calculate the energy of the open-shell singlet by calculating the energy of the hypothetical broken-symmetry singlet (E_{BSS}) instead. The relative energies and equation (**5**) used to calculate the exchange energy *J* are given in Figure 1.3. In this equation, the energies of the triplet (E_T) and broken-singlet symmetry (E_{BSS}), as well as the total spin operator, S, are determined by DFT.

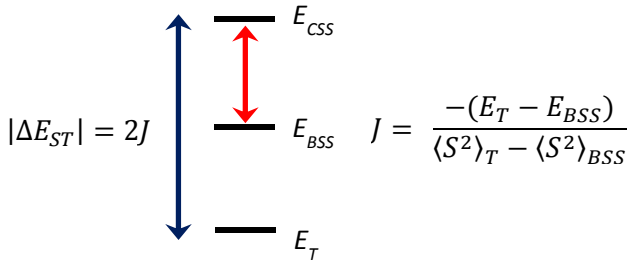

(5)

Figure 1.3 – Relative energies of the closed-shell singlet (E_{CSS}), broken-symmetry singlet (E_{BSS}), and open shell triplet (T), as well as the equation to calculate the exchange energy *J* using the broken symmetry method.

1.2.1 – Radicals as Molecular Magnets

Traditional molecular magnets have been derived from inorganic materials consisting of *d*-block transition metals as well as the lanthanide metals.[14] In these systems, the unpaired electron(s) reside on the metal itself, which is advantageous in its own way. In principle, it is possible to increase the number of spin-bearing metals to form large clusters of isolated spins to form bulk magnets comprising of an infinite array of isolated spins. This field holds rich potential especially in the realm of single-molecule magnets (SMM)[15] and single chain magnets (SCM).[16] One classic example of an SMM, which fueled the start of this field, is "Mn_{12}-acetate", $Mn_{12}O_{12}(O_2CMe)_{16}(H_2O)_4$, consisting of 12 $Mn^{III, IV}$ ions and with a spin of S = 10.[17,18] While a measurable hysteresis and blocking temperature were reported below 2 K, modification of this compound with various ligands and Mn clusters afforded marginal improvement in ordering temperatures in recent years.

The notion that molecular magnets can be made using organic building blocks first began around the late 1970s. However, room temperature organic ferromagnets are much more difficult to come by; the challenge lying in the organization of the molecules in a three-dimensional (3D) network, a criteria critical for spontaneous magnetization. Nevertheless, magnetic ordering has been observed without the use of transition metals, such as [BBDTA][$GaCl_4$] **1-1**, a radical cation salt, at 6.7 K by Awaga.[19] While this compound initially crystallizes as a diamagnetic acetonitrile solvate, removal of the solvent in *vacuo* afforded a small hysteresis. Not long after, the charge transfer (CT) salt, TDAE-C_{60} **1-2**, was isolated, displaying one of the highest ordering temperatures in its class of 16.1 K.[20] However, a crystal structure was never obtained from the microcrystalline powder.

As an alternative to transition metals and charge transfer salts, neutral radicals, with their intrinsic spins, hold great potential as bulk molecular magnets. Prior to 2007, the majority of organic radicals display ferromagnetic ordering temperatures below 2 K. For instance, ferromagnetic ordering in a nitronyl nitroxide radical **1-3** was reported at 0.65 K by Kinoshita,[21] followed shortly by a nitroxide diradical **1-4** by Chiarelli ordering at 1.48 K.[22] Ferromagnetic ordering of thiazyl radicals **1-5** (R = NO_2) was demonstrated by Rawson ordering at 1.3 K.[23] Interestingly, a derivative of this thiazyl radical (R = CN) orders as a canted antiferromagnetic with an unusually high T_N of 36 K.[24]

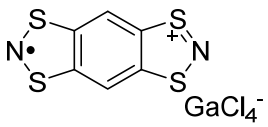

1-1

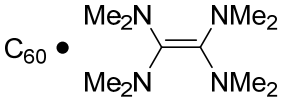

1-2

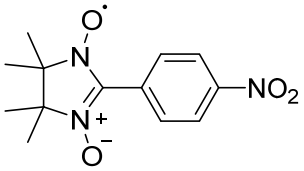

1-3

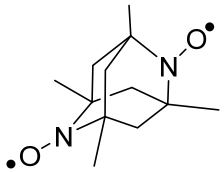

1-4

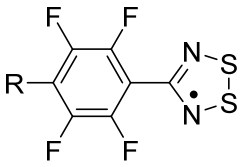

1-5

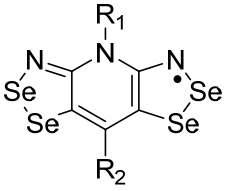

1-6

While the majority of the above materials exhibit negligible hysteresis, the Oakley group have synthesized bisdiselenazolyl radicals **1-6**, which showed remarkable improvement in the magnetic properties.[25] A new record high T_c was recorded at 17 K for the all-selenium derivative (R_1 = Et, R_2 = Cl) and an peculiar large coercive field of 1370 Oe (at 2 K) was observed. This phenomenon can be rationalized as a result of spin-orbit effects and the larger, more diffused orbitals of selenium.

1.3 – Mott insulating and Metallic States

In the previous section, we discussed the scenario in which the Coulomb repulsion energy is large and the bandwidth is small, affording localization of the electrons and thus interesting magnetic responses. However, on the other end of the spectrum where the bandwidth is large enough to offset the Coulomb barrier, a metallic state can be achieved. Accordingly, the relationship between *U* and *W*, and hence metallic and insulating states, can be addressed in reference to the Hubbard model given in equation **2** (section 1.2).

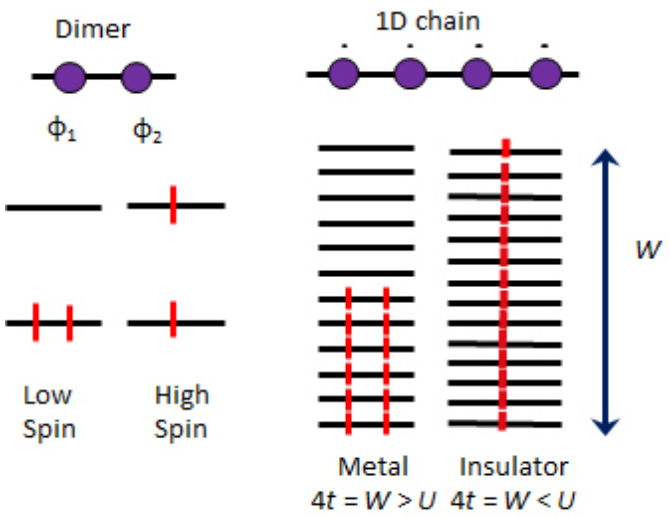

Figure 1.4 –The low-spin and high-spin state of a radical dimer and the corresponding metal and insulator states of a one-dimensional (1D) chain.

The relationship between the resonance integral β and the bandwidth *W* can be understood by the differences between the low-spin and high-spin states using a simple diatomic molecule, such as H_2. In Simple Hückel molecular orbital (SHMO) theory, the energy difference between the two molecular orbitals (ϕ_1, ϕ_2) is given by 2β, where β is the resonance integral given in equation **6**. Moreover, there are only two possibilities the orbitals can be occupied, either a triplet (high spin) state or a singlet (low spin) state, and thus the singlet-triplet gap is given by $\Delta E_{ST} = -2|\beta|$.

$$\beta = \langle \phi_1 || \mathrm{H} | \phi_2 \rangle \tag{6}$$

However, if one replaces the effective Hamiltonian to include electron repulsion effects, the singlet-triplet gap becomes $\Delta E_{ST} = U/2-2|\beta|$. Whether the ground state is the singlet or triplet state is determined by the magnitude of ΔE_{ST}, such that when $\Delta E_{ST} < 0$, the singlet (low-spin) state is the ground state and when $\Delta E_{ST} > 0$ and the triplet (high-spin) state is the lowest in energy.

If we extend this theory to an infinite band of dimers (in this case, a chain of H_2 molecules), the difference between the high-spin state and low-spin state is given by $\Delta E_{ST} = 4\beta + U$. Going back to the Hubbard Hamiltonian given in Equation **2**, a large resonance integral β, analogous to the bandwidth *W* ($4\beta = W$), must be large and the Coulomb repulsion energy *U* must be minimized ($W > U$) for a metallic state to prevail. Since β is a function of SOMO-SOMO overlap, a high degree of orbital overlap is needed to achieve a large *W*, which was the primary focus of the design of neutral radical conductors for the last few

decades. The use of bandwidth enhancement to achieve a metallic state has been an ongoing challenge for the Oakley group and will be discussed after a historical review on organic conductors.

1.3.1 – Charge Transfer Salts as Molecular Conductors

As with molecular magnetism, the notion of electronic conductivity in molecular materials was established as early as the 1900s, but it wasn't until the 1950's that the first highly conductive organic charge transfer salt was synthesized.[26] This sparked the emergence of numerous other organic conductors including conducting polymers (for which a Nobel Prize was awarded in 2000 to Heeger, MacDiarmid, and Shirakawa),[27] radical ion conductors (RIC),[28] closed-shell conductors,[29] and neutral radical conductors (NRC).[30]

The aforementioned materials all possess charge carriers and a conduction pathway, two criteria essential for metallic conductivity. In the case of closed-shell organic conductors, these materials composed of two components, consisting of a donor and acceptor molecule combined together to form a charge transfer (CT) complex. While individually they are insulators, together, charge-transfer complexes have achieved remarkable metallic conductivity and have been the essence of organic conductors for the last 40 years. The first of these CT salts was discovered in 1973, consisting of tetrathiafulvalene (TTF) **1-7** acting as the electron donor (D) and tetracyanoquinodimethane (TCNQ) **1-8** as the electron acceptor (A). Co-crystallization of these two organic solids achieved metallic conductivity down to 60 K,[31] fueling the preparation of over 400 TCNQ-based CT salts.[32,33]

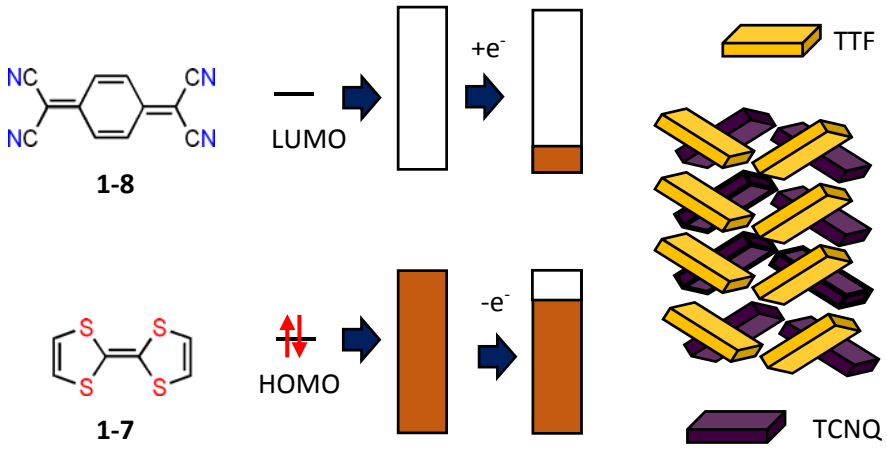

Figure 1.5 - Charge transfer salt TTF-TCNQ (left), partial charge transfer from the HOMO of the donor to the LUMO to the acceptor generating partially filled bands (middle), and the solid-state packing (right).

Exceptionally high conductivity of these charge transfer complexes materializes from the segregated π-stacks between the donor and acceptor, providing good intrastack orbital overlap. Partial charge transfer from the highest occupied molecular orbital (HOMO) of the donor to the lowest unoccupied molecular orbital (LUMO) of the acceptor affords a partially filled band allowing the electron to freely traverse along the stacks. Another variant of charge transfer complexes, radical ion conductors (RIC), were studied comprising of π-molecular donors and inorganic counterions. Two principle donors have been studied: TMTSF **1-9**[34] with various anions such as PF_6^-, AsF_6^-, NO_3^- and BEDT-TTF (bis(ethylenedithio)tetrathiafulvalene or ET) **1-10**[35] with monovalent anions such as I_3^-. The latter ET salts typically take the form of $[ET]_2X$, where oxidation of the donor species in the presence of the anion affords a bandfilling of f = ¾, allowing for metallic conductivity and even superconductivity at low temperatures.

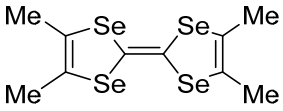

1-9

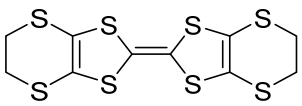

1-10

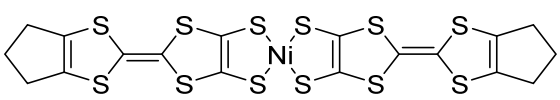

1-11

Although metallic and even superconductivity have been observed in many charge transfer salts, a true metallic conductor derived from a single-component molecular system was not made until 2001. Utilizing the conduction strategy of charge transfer salts, a single-component system having both donor and acceptor like properties was made by Kobayashi. This internal charge transfer salt,$[Ni(tmdt)_2]$ (tmdt = trimethylenetetrathiafulvalenedithiolate) **1-11**, exhibited a room temperature conductivity of 400 S cm^{-1} down to 0.6 K.[36] The unprecedented high conductivity arises from the small separation between the highest occupied molecular orbital (HOMO) and LUMO energy levels, allowing electrons to migrate freely between the bands. Other variations in ligands and transition metals have also been studied.[37]

1.3.2 – Neutral Radical Conductors

As an alternative to charge transfer salts, Robert Haddon proposed the use of neutral radicals as building blocks for molecular conductors in 1975.[38] In principle, an array of radicals each possessing one unpaired electron should generate a half-filled energy band and display metallic conductivity like sodium metal. However, as mentioned in the previous sections, radicals are susceptible to a Pierels[39] distortion (*i.e.* dimerization), which will inevitably cause an opening in the band gap at the Fermi level (Figure 1.6a) and quenching of the unpaired spin. In cases where dimerization can be suppressed, a half-filled energy band (f = ½) possesses a very high on-site Coulomb repulsion energy in which a large bandwidth W must be achieved to offset the large U to obtain a metallic state (Figure 1.6b). In many cases, the bandwidth is

insufficient to overcome this barrier in organic radicals and these materials remain trapped in Mott insulating states (1.6c).

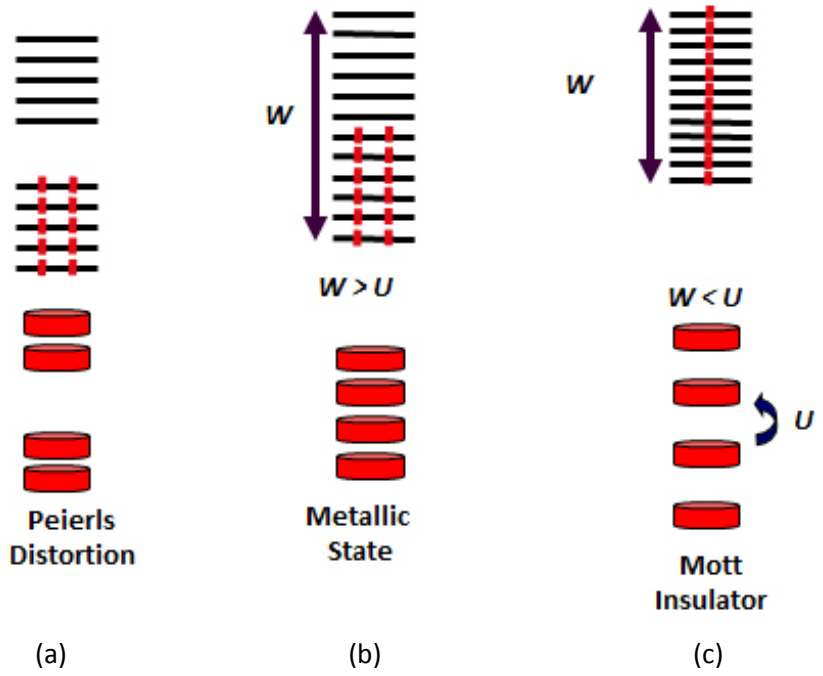

Figure 1.6 - Energy levels of (a) a Peierls distorted π-stack (b) a metallic state and (c) a Mott insulating π-stack.

In order to prepare neutral radicals that satisfy the above criteria ($W > U$), a method of measurement of U and W must be determined. While W can be approximated by Extended Hückel Theory, U is a solid-state property which is not easily accessed. However, U can be approximated computationally in the gas phase by calculating the difference between the energy needed to remove an electron (IP) and the energy needed to add an electron (EA). The overall process can be described as the disproportionation enthalpy, $\Delta H_{disp} = U = IP - EA$. We can also determine U experimentally in solution using electrochemistry, in which the cell potential, E_{cell}, given by the difference between the half-way potential of the oxidation and reduction pathway, can be related to U in the form of $U \sim E_{cell} = E_{½}(ox) - E_{½}(red)$. While these relationships are not exact, the trends exhibited by ΔH_{disp} and E_{cell} are effective in determining changes in U in the solid-state. That is, materials with lower ΔH_{disp} and E_{cell} values have a lower U and are thus better candidates for neutral radical conductors.

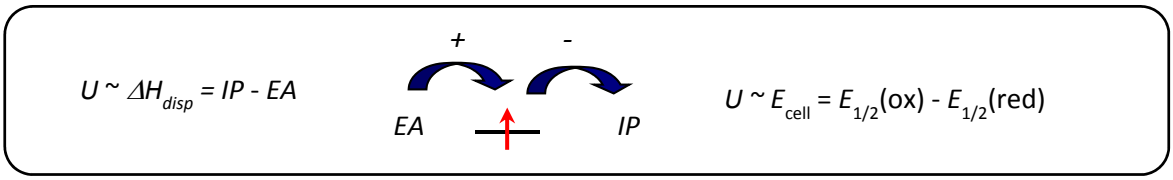

Figure 1.7 - Indirect ways to measure the solid-state property *U* through the disproportionation enthalpy ΔH_{disp} and E_{cell} potential.

1.4 – The First Organic Radicals

The first stable radical **1-12** was characterized in 1901 by Moses Gomberg, where the molecular radical is resonance stabilized by the three phenyl rings.[40] However, it was later discovered triphenylmethyl **1-12** actually exists in equilibrium with its σ-dimer,[41] a typical outcome for sterically unhindered carbon-centered radicals.[42] Further attempts to isolate stable carbon-centered radicals such as **1-13**[43] also afforded insoluble dimers as a result of full π-delocalization. Another class of organic radicals, the phenalenyls **1-14**, also exist in solution in equilibrium with their σ-dimer.[44] However, in deoxygenated solutions, the monomer persists indefinitely as a result of the high resonance delocalization.[45] Although the unpaired electron is typically drawn on the central carbon, analysis of the spin distribution indicates the spin resides predominately on the peripheral α-carbons, rationalizing the ease of the formation of carbon-carbon σ-dimers.[46]

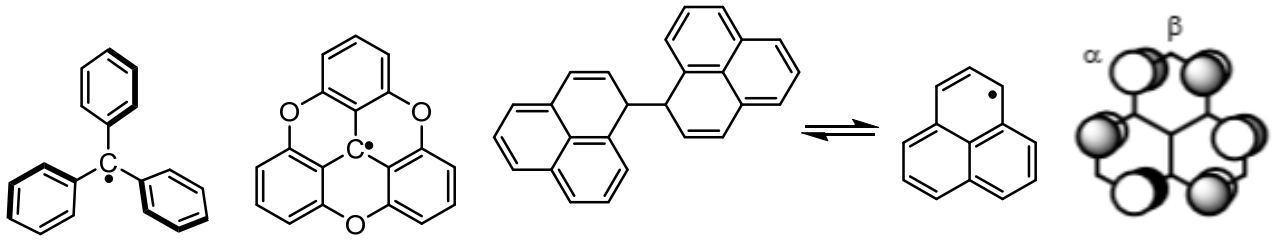

1-12 **1-13** **[1-14]$_2$** **1-14** **1-15**

Various methods to prevent carbon-carbon dimerization in these radicals, the most common being incorporation of steric bulk, as seen in the perchlorinated compound **1-16**.[47] Other substituents have also been used, including *t*-butyl groups **1-17**[48] as well as isopropyl groups (R = *i*-Pr) for the cyclopentadienyls **1-18**.[49] Although **1-17** does not form σ-dimers, it associates in another form, as π-dimers, where the two radicals form superimposed π-stacks with the *t*-butyl group eclipsed to minimize steric congestion.

Interestingly, in the case of **1-18**, smaller substituents such as methyl groups (R = Me) do not provide enough steric hindrance, and these form σ-dimers in solution.

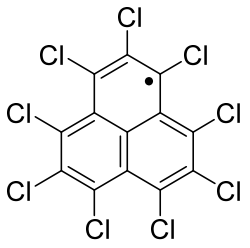

1-16

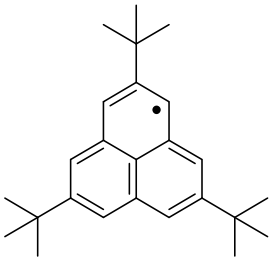

1-17

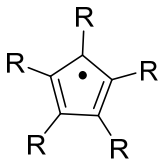

1-18

The ease for carbon-based radicals to associate as σ and π-dimers, even with careful kinetic and thermodynamic control, naturally led to the incorporation of other elements, namely nitrogen, oxygen, and sulfur, into the organic framework to provide additional stability.

1.4.1 – Organic Heteroatom Radicals

The idea of light heteroatom radicals stemmed from the existence of well-known atmospherically stable radicals such as nitric oxide (NO), nitrogen dioxide (NO_2), and molecular oxygen (O_2). The electron-richness in these systems, which may be related to Coulson's "alpha effect",[50] inhibits formation of σ-dimers. For example, N-N and O-O bonds are typically weak (150-250 kJ mol^{-1}) compared to a C-C bond (~370 kJ mol^{-1}), as a result of the repulsion between lone pairs of the neighbouring atoms.

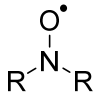

1-19

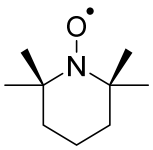

1-20

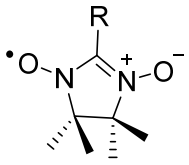

1-21

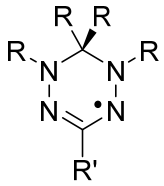

1-22

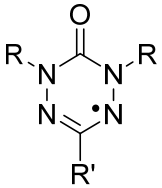

1-23

Over the years, many well-known families of N- and O-containing stable radicals have been characterized with various properties and stabilities, including the nitroxyls **1-19**, nitronyl nitroxides **1-21**, verdazyls **1-22**, and oxoverdazyls **1-23**. One of the most notable nitroxyls is TEMPO (2,2,6,6-tetramethylpiperidine-N-Oxyl) **1-20**, which is highly stable and has been used extensively for spin-labelling studies.[51] Incorporation of resonance delocalization into the framework across two NO units afford the nitronyl nitroxides **1-21**, while resonance stabilization across nitrogen atoms forms the verdazyls **1-22**[52] and the related oxoverdazyls **1-23**.[53] In the case of the resonance stabilized hydrazyl radicals **1-22** and **1-**

23, steric congestion is not required as a result of the increase in stability supported by an electron-rich ring system.

The intrinsic open-shell nature of these nitroxyl radicals allow for interesting magnetic properties, observed in the nitronyl nitroxide radical **1-3** and the nitroxide diradical **1-4** mentioned in section 1.2.1. As of today, numerous magnetic properties of nitroxide-based radicals have been studied.

1.4.2 – Heavy Heteroatom Radicals

Incorporation of heavier heteroatoms such as sulfur into organic frameworks can also be used to impart softness (lower *U*) and suppress dimerization. Although sulfur and oxygen reside in the same group on the periodic table, the much larger and more polarizable sulfur atom increases the tendency for sulfur radicals to associate as disulfide dimers at room temperature. One of the earliest examples were explored by Haddon, in which sulfur atoms were incorporated into and around the phenalenyl framework. In the latter case **1-24**, no C-C σ-dimers were present, but the crystal structure revealed rupturing of one of the rings to form S-S σ-dimers **[1-24]**$_2$.[54] On the other hand, isolation of **1-25** revealed the absence of C-C as well as S-S σ-dimers, representing the first stable radical without the use of bulky substituents. However, the structure is based on π-dimers and thus conductivity is still compromised, with $\sigma_{RT} < 10^{-6}$ S cm^{-1}.[55]

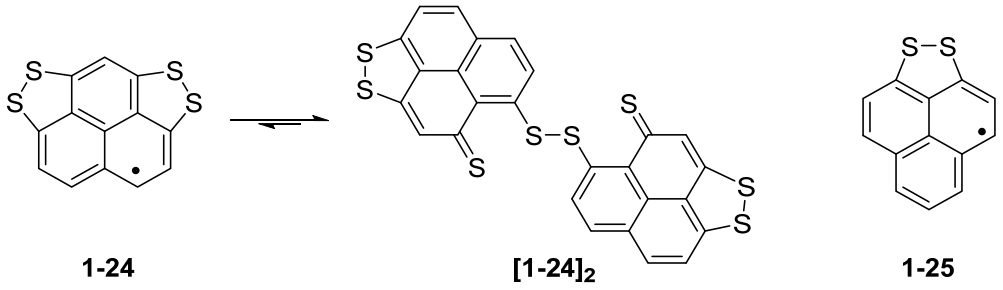

1-24 **[1-24]$_2$** **1-25**

Despite the increase in propensity of sulfur-based radicals to dimerize, numerous molecular systems have been developed since the 1970s displaying remarkable physical properties. One particularly famous example is the compound poly(sulfur nitride)$(SN)_x$, the first example of a synthetic metal exhibiting superconductivity below a critical temperature of 0.3 K.[56] It was initially prepared by solid-state polymerization of molecular S_2N_2, crystallizing as fibrous golden needles. The crystal structure consists parallel chains of covalently linked SN units in a *cis-trans* fashion allowing close interactions between the sulfur atoms.

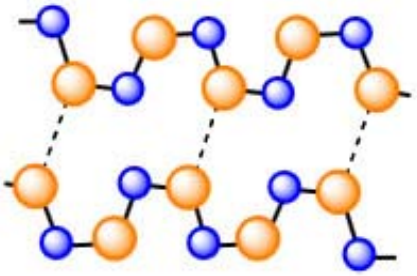

Figure 1.8 - Schematic drawing of (SN)x illustrating the S-N covalent bonds and interchain interactions (dashed lines).

The remarkable properties of poly(sulfur nitride)(SN)x fueled the development of radical heterocycles containing –S=N- subunits. The initial building blocks were the 1,2,3,5-dithiadiazolyl radicals (DTDA) **1-26**, discovered in the 1970s,[57] the related 1,2,3,5-diselenadiazolyls (DSDA) **1-27**,[58] and various dithiazolyl (DTA) isomers, **1-28** and **1-29**.[59] The most appealing feature of the DTDA **1-26** and DSDA **1-27** molecular systems lies, in part, to the nature of the electronic structure where the singly-occupied molecular orbital (SOMO) is nodal at the carbon, allowing various R-substituents to be incorporated into the ring without affecting the electronic properties. In other words, various R-groups can be included to fine-tune the solid-state packing to improve *W*. In contrast, electronic communication between the R-substituents are allowed for 1,3,2-DTA **1-28a** (*via* R_1 and R_2) and **1-29a** (*via* R_1) as the carbon atoms possess some spin density.

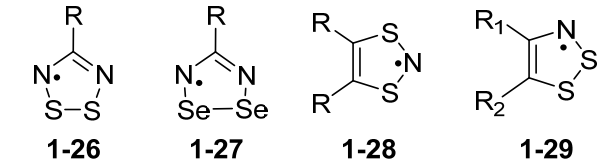

In many cases, the majority of the spin density resides on the sulfur and nitrogen atoms making these compounds prone to associate as π-dimers in the absence of steric protection.[60] The symmetry of the SOMO, which is antibonding in nature, allows for various mode of dimerization as shown in Figure 1.8. The dimerization enthalpy has been estimated to be ~ 35 kJ mol^{-1} and calculations[61] have shown minimal differences between the different modes of dimerization (< 5 kJ mol^{-1}).[62] Consequently, the nature of the

mode of dimerization resides on the steric requirements for the R-substituent. The most common of these are the *cis*-cofacial dimer (Figure 1.8a) followed by the twisted cofacial structure (Figure 1.8b). The former is found for 4-phenyl-1,2,3,5-DTDA along with other simple aromatic variants,[63,64] while the latter is typically found where the R-substituent is nonplanar such as CF_3, Me, NMe_2, Cl and adamantyl.[65] The other two arrangements are not commonly observed (1.8c[66] and 1.8d[67]).

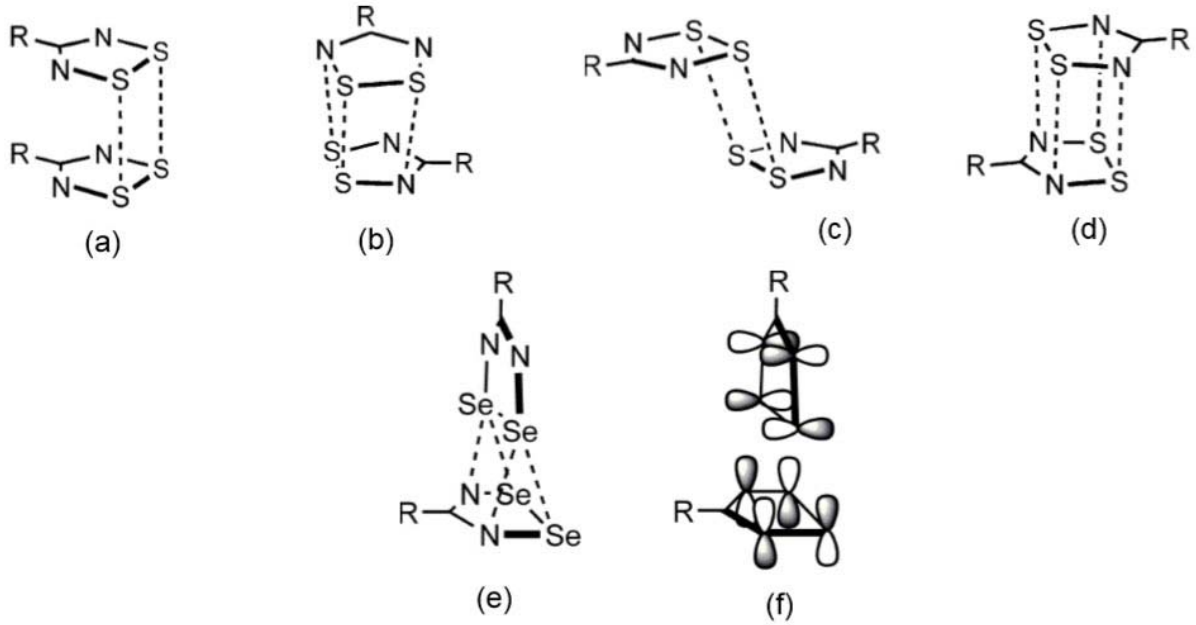

Figure 1.9 - Typical modes of dimerization of DTDA and DSDA radicals including (a) *cis*-cofacial, (b) twisted cofacial, (c) *trans*-antarafacial, (d) *trans*-cofacial, and (e) T-shaped with (f) corresponding π*-π* interactions. Adapted from Reference 3a.

The selenium analogues of DTDAs, the DSDAs, have also been studied extensively for their potential as conducting materials as a result of an increased bandwidth associated with the more diffuse Se orbitals.[68] At the same time, the DSDAs also typically form *cis*-cofacial dimers, although a unique T-shaped association motif was found when R = *p*-chloro and *p*-bromo-tetrafluorophenyl.[69] This peculiar structure arises as a result of the spin-paired spiroconjugated SOMOs shown in Figure 1.8f.

The high tendency for the DTDAs and DSDAs to dimerize in the solid-state results in spin-pairing, and consequently no magnetic properties are observed, although some DSDAs dimers behave as small band gap semiconductors. A great deal of effort has been made to prevent spin pairing, but there are few derivatives that are paramagnetic in the solid-state. In contrast, the 1,3,2-DTAs **1-28** possess a negligible dissociation enthalpy (ΔH_{diss} ~ 0 kJ mol^{-1}) and exist predominately as monomers in the solid-state.[70] Interestingly, some diamagnetic dimers of these types of radicals exhibit curious thermomagnetic

properties, undergoing thermally induced dissociation from the diamagnetic (*S* = 0) state to the paramagnetic radical (*S* = ½) state. In some case this process is hysteretic, and can give rise to materials displaying bistable behaviour.[71]

1.4.3 – Resonance Stabilized bisdithiazolyl Radicals

The next generation of thiazyl radicals, the 1,2,3-DTAs **1-29** were pioneered by the Oakley group. Similar to the other DTDA systems **1-26**, the SOMO is antibonding in character and nodal at the R_2-carbon. However, spin density can seep onto the R_1-substituent (**1-29a**) as the carbon possesses a small coefficient. Over the years, numerous DTA rings have been characterized, including the simple benzo-fused derivative **1-30**.[72] This particular compound has been identified in solution *via* EPR and cyclic voltammetry (CV), but its solid-state structure is not known. Incorporation of heavier chalcogens such as selenium and tellurium into **1-30** afforded strongly associated dications $\mathbf{[1\text{-}30]}_2^{2+}$ (E = Se, Te).[73] Radicals **1-32**[74] provided some steric congestions on the peripheries, however, still formed dimers in the solid-state. In contrast to the aforementioned 1,2,3-DTA radicals, dithiazolyl **1-33** is monomeric in the solid-state and display slipped π-stacked arrays. Although the room temperature conductivity is much higher than the DTDAs, it is still low at 10^{-7} S cm^{-1}, indicative of a Mott insulating state.[75]

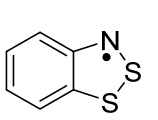

1-30

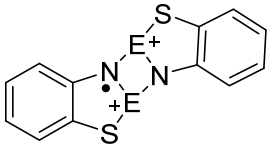

$[1\text{-}30]_2$

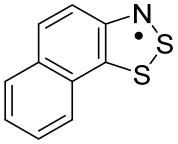

1-31

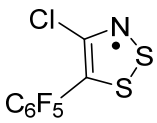

1-32

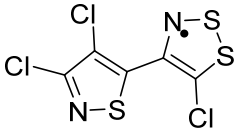

1-33

Not long after, the Oakley group revolutionized the thiazyl chemistry by exploring resonance stabilized bisdithiazolyl DTA radicals, consisting of two DTA rings fused across a pyridine bridged core **1-34**. The unpaired electron is delocalized throughout the entire π-system, with the majority of the spin centered on the thiazyl rings, as shown in the SOMO **1-34a**. Moreover, a large number of these radicals do not associate as σ- or π-dimers as a result of the increased resonance stabilization and the bulky R-substituents on the peripheries.

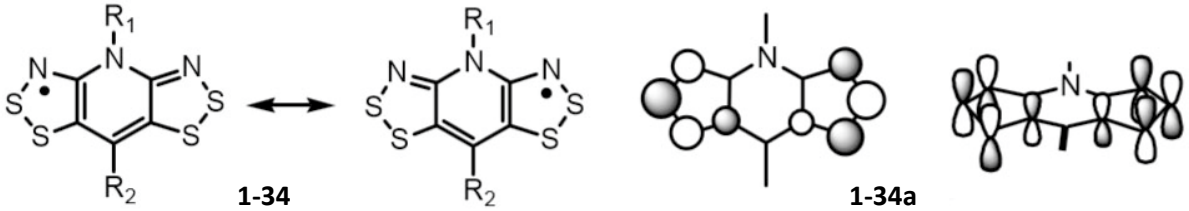

1-34 **1-34a**

These resonance-stabilized bisdithiazolyl radicals have exhibited interesting magnetic and conductive responses, which will be further discussed in the following sections and subsequent chapters. Moreover the diverse structural variety of these thiazyl radicals provide a means to fine-tune the electronic and solid-state properties required to pursue a metallic state.

1.5 – Thiazyls as Neutral Radical Conductors

For many years, goals of developing multifunctional materials that exhibit magnetic and/or conductive properties from neutral radicals have been pursued. The initial challenge lies in synthesizing monomeric free radicals in the solid-state since many of the early generation radicals associate as σ- and π-dimers. While a handful of these thiazyl radicals were characterized, small intermolecular overlap between the radicals result in a low *W* and remain as Mott insulating states as the Coulomb repulsion energy *U* remains high for a $f = ½$ system. Room temperature conductivities have improved for selenium analogues peaking at 10^{-5} S cm^{-1}, while the open-shell Mott insulators display room temperature conductivities around 10^{-7} S cm^{-1}.

The task of lowering *U* or increasing *W* for neutral radical conductors has been an ongoing challenge for the Oakley group. As mentioned in the earlier sections, the solid-state property *U* is approximated by the disproportion enthalpies (ΔH_{disp}) and E_{cell} values, in which a low ΔH_{disp} and E_{cell} suggest a low *U*. The computed gas-phase ion energetics and cell potentials for mono- and bis-DTA radicals are tabulated in Table 1.1. One method of minimizing *U* is to increase the resonance stabilization as seen with the pyridine-bridged bisdithiazolyl radicals **1-35**. Although the bisdithiazolyl radicals possess very low *U* values, conductivities are still activated as a result of the formation of slipped π-stacks, which reduces *W*. Consequently, various R-substituents were incorporated to pursue better packing motifs. The behavior of some these bisdithiazolyl radicals will be summarized in the next section, as many of the conclusions were used towards my research goals.

Table 1.1 – Computed Gas-Phase Ion Energetics[a] and Cell Potentials[b] for Thiazyl Radicals.

Compound	*IP*	*EA*	ΔH_{disp}[c]	$E_{½}^{(-1/0)}$	$E_{½}^{(0/1)}$	E_{cell}[d]
1-26	7.82	1.02	6.81	-0.94	0.59	1.53[e]
1-28	6.77	-0.41	7.18	-	-	-
1-29	7.01	0.34	6.67	-1.1[f]	0.38	1.48[g,h]
1-37	6.16	1.39	4.77	-0.95	-0.130	0.77[i]

[a]Adiabatic ΔSCF values at the B3LYP/6-31G(d,p) level, R = H for all systems, values in eV. [b]In MeCN, ref. SCE, values in V. [c]$\Delta H_{disp} = IP - EA$. [d]$E_{cell} = E_{½}^{(0/+1)} - E_{½}^{(-1/0)}$. [e]R = Me. [f]Irreversible behavior, E_{pc} value reported. [g]E_{cell} estimated as $E_{pc}^{(0/+1)}$-$E_{pc}^{(-1/0)}$. [h]R = Cl, R_1 = C_6F_5. [i]R = Me.

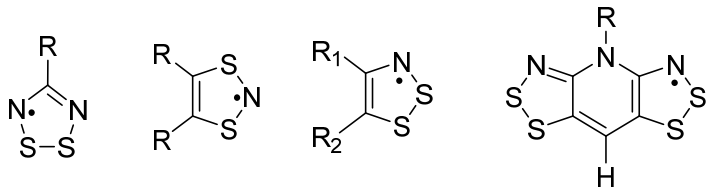

1-26 **1-28** **1-29** **1-37**

1.6 – Bisdithiazolyl Radicals

The development of resonance stabilized bisdithiazolyl radicals along with their selenium variants has enlightened this field significantly. A large number of derivatives have been synthesized and characterized in the last few years, displaying novel physical properties. Although the beltline R_1/R_2 substituents help suppress dimerization, a large number of these radicals pack in herringbone motifs (Figure 1.9a) which reduce the intermolecular interactions between the radicals along the π-stacks. Consequently, *W* is insufficient to overcome the Coulomb repulsion energy *U*, and thus the majority of these materials are trapped in Mott insulating states.

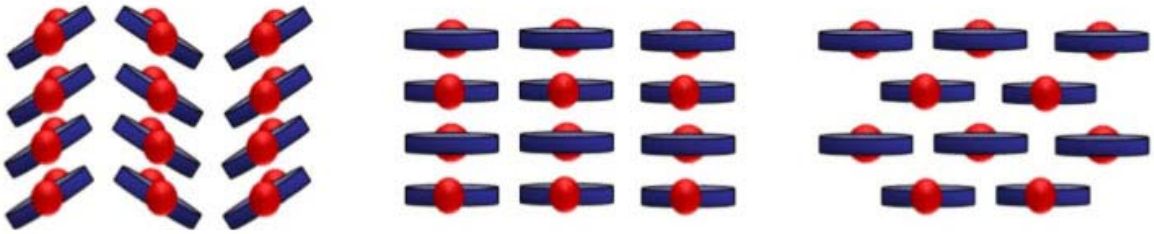

(a) (b) (c)

Figure 1.10 – π-stacking motifs exhibited by bisdithiazolyl radicals: (a) herringbone π-stacks, (b) superimposed ABAB π-stacks and (c) layered π-stacks.

One method to improve the molecular overlap is by incorporation of a much larger, softer chalcogen with more diffuse orbitals such as selenium into the framework **1-34**. Three new variants **1-38**, **1-39**, and **1-40,** have led to improved conductivity and gave rise to remarkable magnetic effects.[76] One particularly notable example is the all selenium radical **1-40** (R_1 = Et, R_2 = Cl), which orders as a bulk ferromagnet with T_c values of 17 K, one of the highest for bisdithiazolyl radicals. Moreover, application of pressure eventually generated enough bandwidth *W* to overcome the Coulomb repulsion energy barrier *U*, representing one of the first neutral radical insulator-to-metal transitions.[77] The effects of pressure on other bisdithiazolyl radicals will be discussed in the following chapters.

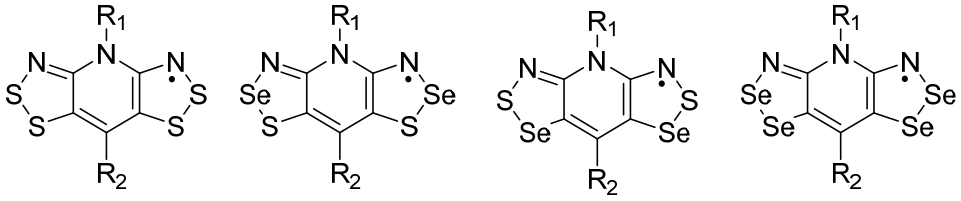

1-34 **1-38** **1-39** **1-40**

Another method to improve the molecular packing involved removal of the beltline ligands by replacement of the basal carbon with a nitrogen atom to produce the pyrazine-bridged radicals **1-41**. This reduces steric congestion, but the tendency to dimerize increases, as found with the ethyl derivative **1-41b.**[78] In contrast, the methyl derivative **1-41a** crystallizes as superimposed ABAB π-stacks (Figure 1.9b), which affords conductivity that rivals those of the selenium variants at 10^{-3} S cm^{-1} **1-40**. However the uniformly spaced ABABAB radical π-stacks collapse into diamagnetic dimers below 120 K.[79]

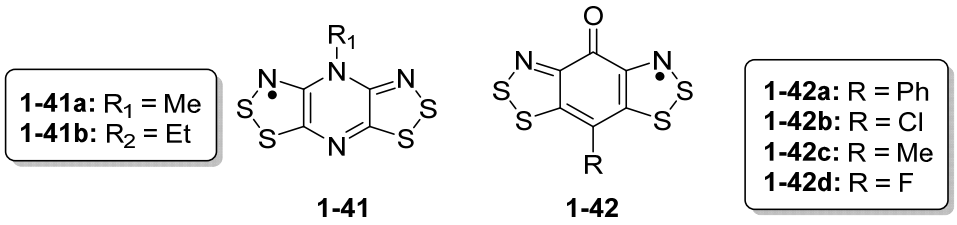

1-41a: R_1 = Me
1-41b: R_2 = Et

1-41 **1-42**

1-42a: R = Ph
1-42b: R = Cl
1-42c: R = Me
1-42d: R = F

To break away from the traditional herringbone packing exhibited by the majority of pyridine-bridged bisdithiazolyl radicals **1-34**, while at the same time avoiding the spin quenching dimerization found in the pyrazine radicals **1-41,** the Oakley group recently developed a new family of resonance stabilized bisdithiazolyl radicals by an isoelectronic replacement of the N-R fragment with a carbonyl moiety to form a new family of oxobenzene-bridged bisdithiazolyl (RBBO) radicals **1-42**.[80] Satisfyingly, the polarity of the carbonyl CO bond did indeed led to a new packing motif, where strong intermolecular S---O' and S---N' supramolecular synthons[81] gave rise to a more rigid, strongly-bound framework. To our initial surprise,

cyclic voltammetry measurements indicated a noticeably lower *U*, estimated in terms of E_{cell} at 0.5 - 0.7 V. The effects of the various basal substituents on the E_{cell} value will be discussed in Chapter 3 and 5. Overall, these changes afforded an improvement by several orders of magnitude in conductivity at ambient pressure.

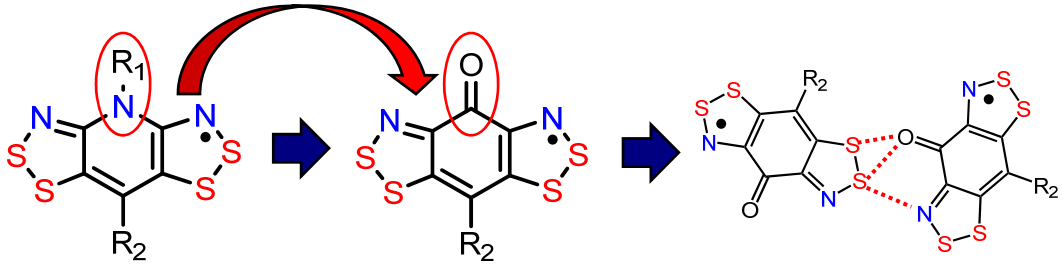

Figure 1.11 - Isoelectronic replacement of the NR group in **1-34** with a carbonyl moiety in **1-42** to form molecular ribbons.

Variations in conductivity within the family also arises in part from the diverse molecular arrangement as well as the associated with different R-groups (R = Ph, Cl, Me, F) at the basal site. For instance, incorporation of a phenyl ring (R = Ph) **1-42a**, crystallizes as alternating ABABAB superimposed π-stacks, reaching a conductivity of 3 x 10^{-5} S cm^{-1} at 300 K.[82] Its superiority to the pyridine-bridged can be recognized with the increase in orbital overlap of the superimposed π-stacks, opposed to the slipped π-stacks typically found for the pyridine-bridged systems. However, the bulky phenyl substituent prohibits lateral interactions, resulting in a strongly one-dimensional electronic structure.

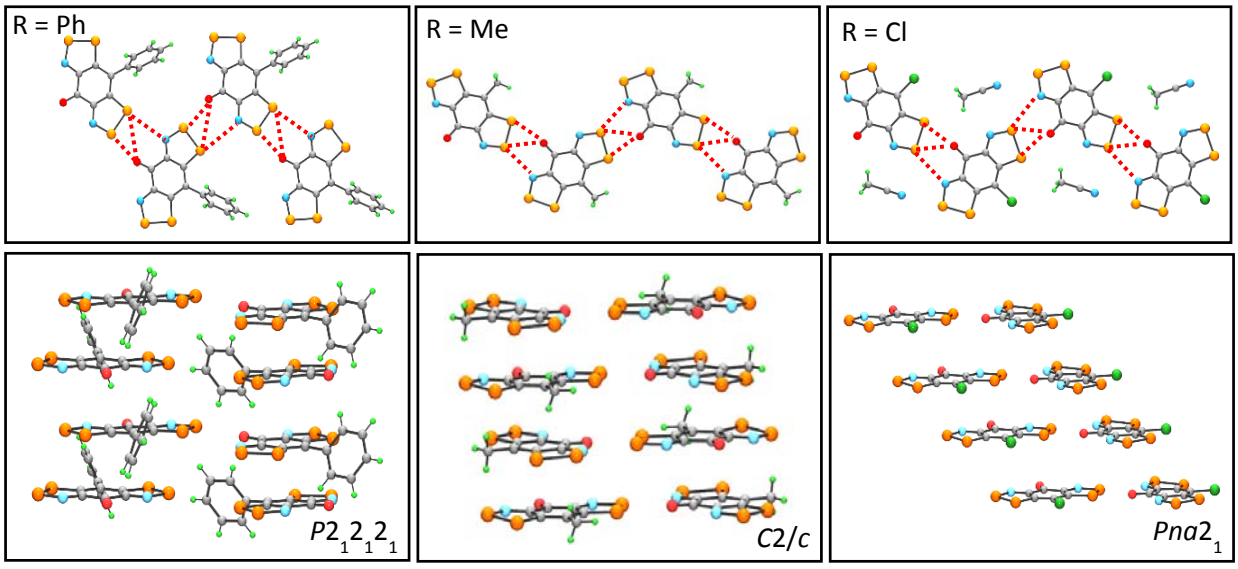

Figure 1.12 - Different packing motifs linked together by strong S---O' and S---N' supramolecular synthons for oxobenzene-bridged radicals **1-42a-d** (R = Ph, Me, Cl).

The chloro-substituted semiquinone-bridged (R = Cl) radical **1-42b** and its MeCN solvate[83] were also synthesized, both crystallizing with strong oxygen-to-sulfur interactions. Crystals of the MeCN solvate form regular (not alternating) slipped π-stacks along the *z*-direction, while the non-solvated radical displayed evenly slipped π-stacks along the *b*-axis. However, the most remarkable feature of these radicals lie with their charge transport properties, with σ_{RT} peaking at 10^{-3} S cm^{-1} and a satisfyingly low activation energy E_{act} of 0.11 eV. Whether this was the effect of better overlap along the slipped π-stacks, a softer core (lower *U*), or a combination of the two, will be discussed in detail in chapter 3.

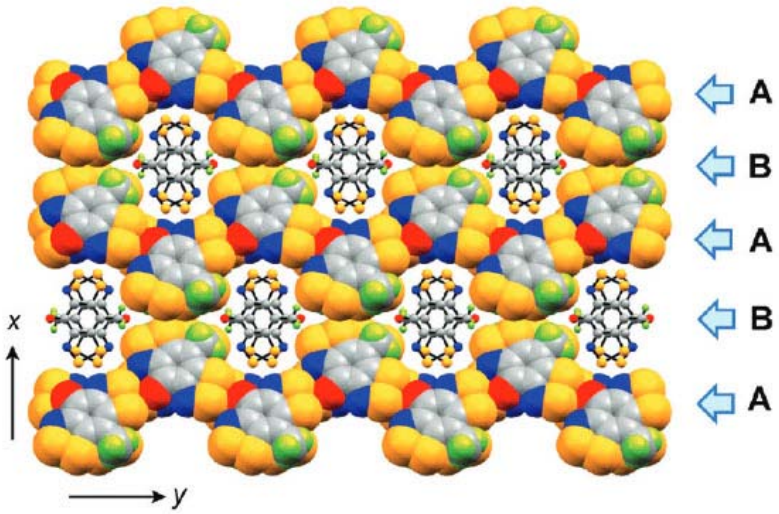

Figure 1.13 - Radical environments A and B of **1-42c** (R = Me) viewed parallel to the stacking axis. Radicals B are sequestered between the ribbon-like arrays of radicals A.

Incorporation of a methyl substituent **1-42c** at the basal site afforded the first bimodal neutral radical crystal structure, in which two distinct radical environments, A and B, are present. Radicals A crystallize in the conventional ribbon-like arrays along the *x*- and *y*- direction, while the other radicals B are sequestered in the cavities formed by the radical environment A. Like the other oxobenzene-bridged radicals, the methyl derivative **1-42c** enjoys a low *U* value but display a slightly lower conductivity of 10^{-4} S cm^{-1}. However, its activation energy of 0.13 eV rivals those of the chloro derivative **1-42b** (R = Cl).[84]

In the case of the fluoro-substituted radical **1-42d** (R=F),[85] the presence of a fluorine atom at the basal site provides an additional structure maker, interlacing the ribbon-like arrays with S---N, S---O, and S---F supramolecular synthons in both the *x*- and *y*- direction. This two-dimensional "brick-wall" architecture, illustrated in Figure 1.14, displays the highest ambient temperature conductivity of 10^{-2} S cm^{-1} within the family of oxobenzene-bridged radicals, with a thermal activation energy of 0.10 eV. Moreover,

metallization has been achieved by compression to just 3 GPa, which is considerably lower than the pressure required for Se-based derivatives **1-38** to **1-40**.[86]

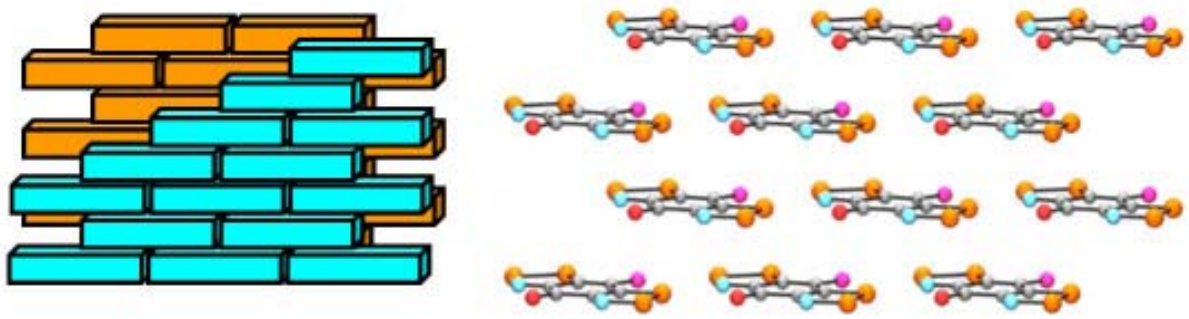

Figure 1.14 - "Brick-wall" architecture of **1-42d** (R = F) as a result of S---O, S---N, and S---F supramolecular synthons.

All of these oxobenzene-bridged radicals **1-42** enjoy an intrinsically low *U* and a large bandwidth *W* as a result of a more tightly packed structure. As a result, the conductivities of these materials are several orders of magnitude larger than the pyridine-bridged systems **1-34**. The rationale behind these physical properties will be discussed in chapter 3.

1.7 – Thesis Scope

For many years, the Oakley group focused on the pyridine-bridged bisdithiazolyl radicals **1-34** by varying the R_1/R_2 substituents in hopes to fine-tune the solid-state packing. However, the steric bulk typically buffers any electronic interactions resulting in a low bandwidth and Mott insulating states. Shortly before I began my graduate studies, the Oakley group had started synthesizing and characterizing many of these oxobenzene-bridged radicals **1-42** (R = Ph, Cl, Me, F). The diverse structural variety exhibited by these materials prompted the study of other substituents at the basal site (R = H, NO_2, CN), with goals of lowering the E_{cell} value and improving the molecular packing in the solid-state. The bulk of my graduate work spans several generations of radicals, with the primary focus on the synthesis and characterization of new oxobenzene-bridged radicals and the effect of pressure on these systems.

However, before launching into a discussion of the oxobenzene-bridged systems, the presentation of new work will begin (**Chapter 2**) with a small project dating back to the first DTDA systems. Over twenty years ago it was recognized that the solid state structures of radicals and radical dimers based on this

framework could be controlled by the use of cyano-functionalized R-groups, which tend to link the radical dimers into approximately coplanar ribbons held together by supramolecular CN---S′ supramolecular synthons. In Chapter 2, this idea for structural control is extended to include the use of pyridyl substituents as structure-makers. The solid-state packing of various pyridine-DTDA systems along with their selenium analogues will be examined.

In the pursuit of better molecular packing exhibited by the oxobenzene-bridged radicals, the synthesis, characterization, as well as pressure effects will be examined on the prototypal oxobenzene-bridged radical (R = H) in **Chapter 3**. While the hydrogen atom does not act as a supramolecular synthon, instead distorting the coplanarity of the crystal structure, metallization is still achieved under mild pressure. The rationale behind the improved physical properties of these oxobenzene-bridged radicals **1-42** to the pyridine-bridged radicals **1-34** will also be discussed.

In extension to the previous chapter, another derivative of the oxobenzene-bridged radical will be explored in **Chapter 4**. Once again, in pursuit for more tightly-packed molecular structures, the carbon atom at the basal site is replaced with a nitrogen atom, forming the so-called pyridone system. To our surprise, pyridine chemistry appears to be much more difficult than expected, and the anticipated material was never synthesized. However, a broad range of synthetic schemes have been tried and will be presented accordingly.

The latest work from the Oakley group will be presented in **Chapter 5**, which entails yet another derivative of the oxobenzene-bridged radical. This variant involves the incorporation of NO_2, a π-acceptor, at the basal site, which effectively lowers the *U* to 0.45, the lowest we have seen for any neutral radical conductor. While this is still ongoing work, the preliminary synthesis, crystal structures, and physical properties will be explored.

Chapter 2

Nitrogen as a Structure-Directing Atom in Pyridyl-dithiadiazolyl Radicals

2.1 – Introduction

Organic radicals have been prepared and studied extensively, especially for their importance in living organisms. However, it wasn't until the last century that applications of organic radicals have extended towards conductivity and molecular magnetism.[1] As mentioned in the previous chapter, in order for a material to behave as an electrical conductor or molecular magnet, it must contain unpaired electrons and a conduction pathway, which depends on the arrangement of the molecules in the solid-state. Consequently, to achieve magnetic or conductive properties, it is imperative to control, to some degree, the solid-state packing. For this reason, crystal engineers and magnetochemists have become interested in studying these types of systems.

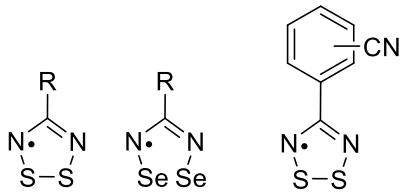

2-1 **2-2** **2-3**

The use of dithiadiazolyl (DTDA) radicals **2-1** as potential building blocks for neutral radical conductors has been well documented. As mentioned in the previous chapter, the SOMO of DTDA radicals is nodal at the carbon, allowing different supramolecular synthons to be incorporated in the R-substituent to fine-tune the solid-state packing without strongly affecting the electronic structure. However, 1,2,3,5-DTDA radicals are prone to Peierls[2] distortion, quenching the spin in the solid-state. Improved conductivity has been observed with isostructural replacement of sulfur with its heavier congener selenium, the so called 1,2,3,5-diselenadiazolyl (DSDA) radicals **2-2**, as a result of an increased bandwidth associated with the more diffuse Se orbitals.[3]

The first DTDA radical characterized was phenyl-1,2,3,5-DTDA[4] in 1980 (R = Ph), crystallizing as *cis*-cofacial dimers, followed by other variations including R = CF_3,[5] NMe_2[6], adamantyl,[7] which all adopted the twisted cofacial configuration. The need to incorporate structure directing groups to tailor the solid-state packing associated with magnetic and conductive properties became readily recognized. One particular example is the cyano moiety in which CN---X interactions have been well established in *p*-

iodobenzonitrile[8] and cyanogen halides.[9] For this reason, the 3'- and 4'-cyanophenyl 1,2,3,5-dithiadiazolyl radicals **2-3** were pursued. [10] Synthesis and characterization of these radicals revealed the cyano moiety functions as a structure directing group resulting in chains of molecules from CN---S supramolecular synthons. It was proposed that ribbon-like arrays are primed for better stacking and thus better conductivity, however, their propensity to dimerize also increases as seen in many of these DTDA molecular systems. In the case of 4'-cyanophenyl-1,2,3,5-dithiadiazolyl, it crystallizes as *cis*-dimers, whereas the 3-cyanophenyl-1,2,3,5-dithiadiazolyl radical is polymorphic, crystallizing as *cis*-dimers in the α-phase and *trans*-antarafacial dimers in the β-phase. More importantly, the common feature exhibited by all three structures lies in the chain of molecules interlaced by CN---S' supramolecular synthons to form ribbon-like arrays. Several other cyano-substituted materials were synthesized and shown to display similar CN---S' intermolecular interactions.[11]

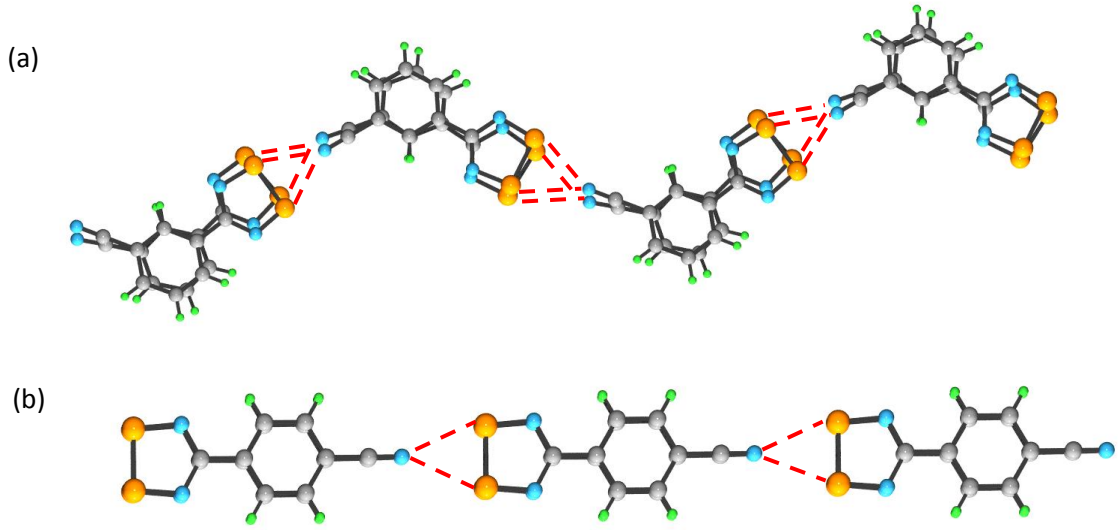

Figure 2.1 - Chains of molecules of (a) α-phase of 3-cyanophenyl-1,2,3,5-DTDA radicals and (b) 4-cyanophenyl-1,2,3,5-DTDA radicals linked by S---CN supramolecular synthons.[10]

In pursuit of molecular ribbons linked by N---S supramolecular synthons, the effect of incorporation of a pyridyl moiety to the DTDA ring was studied. The synthesis and characterization of 4 new variants: 3- and 4-pyridylDTDA (3-PyDTDa and 4-PyDTDA) radicals, **2-4a** and **2-4b**, along with their selenzyl counterparts (3-PyDSDA and 4-PyDSDA), **2-4c** and **2-4d**, will be described below.

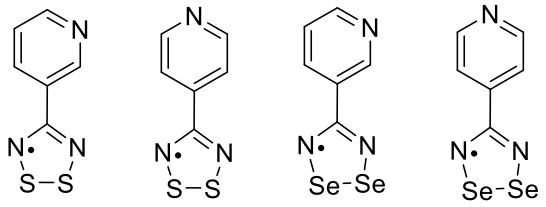

2-4a **2-4b** **2-4c** **2-4d**

2.2 – Results

2.2.1 – Synthesis

The synthesis for **2-4a-d** follows the synthetic procedure depicted in scheme 2.1. The synthesis for 3-PyDTDA and 4-PyDTDA are identical except for their respective starting material, thus, only the synthesis of 4-PyDTDA **2-4b** and 4-PyDSDA **2-4d** are shown.

Scheme 2.1

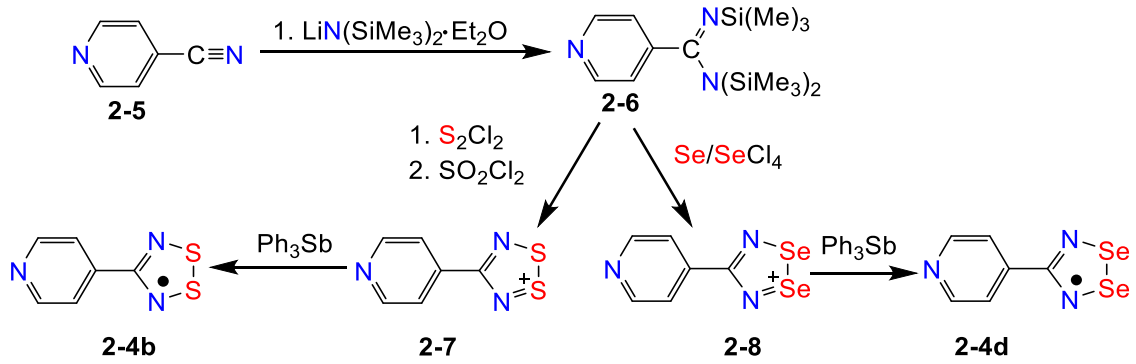

Both the sulfur and selenium variant commences with the amidination and silylation of **2-5** with lithium bis(trimethylsilyl)amide, affording a viscous yellow oil. Closure with sulfur monochloride followed by oxidation with sulfuryl chloride yields the corresponding cation **2-7**. Subsequently, the cation is reduced with triphenylantimony(III) to afford a dark purple powder. Lustrous green shards of 3-PyDTDA **2-4a** were obtained by vacuum sublimation in a three-zone furnace along a temperature gradient of 50 – 100 °C for single X-ray crystallography. However, single crystals were not obtained for 4-PyDTDA **2-4b**; instead irregular black nodules were obtained.

The selenium variants were synthesized by closure using selenium tetrachloride to afford a maroon powder **2-8**. The product was reduced with triphenylantimonyl(III) to afford the desired radical. Crystals suitable for single crystal X-ray crystallography were obtained for both 3-PyDSDA **2-4c** and 4-PyDSDA **2-4d** *via* sealed-tube sublimation in a three-zone furnace along a temperature gradient of 80-140 °C.

2.2.2 – Electron Paramagnetic Resonance

Electron paramagnetic resonance (EPR) on **2-4a** and **2-4b** illustrated a distinctive five line pattern, as expected for coupling between the two equivalent ^{14}N nuclei. Hyperfine coupling a_N of 0.5 mT and g values of 2.011 are nominal for molecular systems of this type. EPR on the selenzyl materials were not obtained due to solubility restrictions.

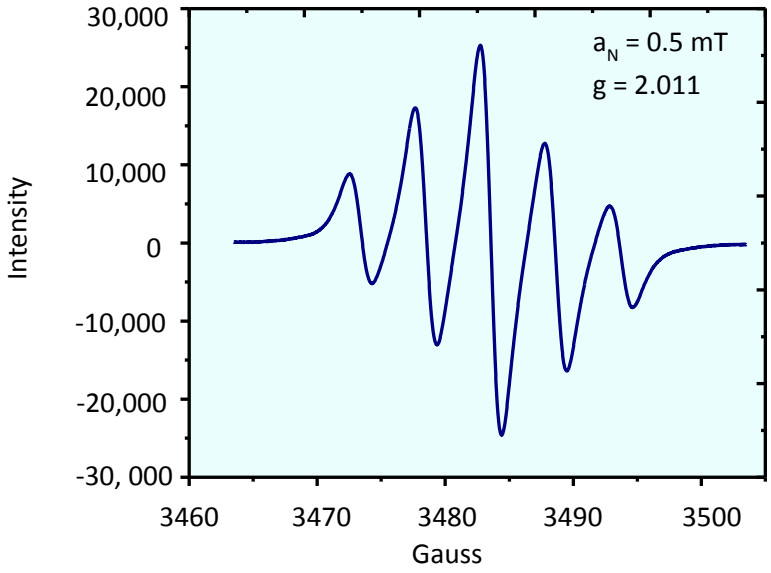

Figure 2.2 - EPR spectra of **2-4a** illustrating the distinctive 5-line pattern arising from coupling between the two nitrogen nuclei.

2.2.3 – Crystallography

Of the four sulfur and selenium PyDTDA radicals synthesized, three of the structures were determined by single X-ray crystallography (Figure 2.3). Crystal metrics obtained at 296 K are summarized in Table 2.1. Both radicals of 3-PyDTDA **2-4a** and 3-PyDSDA **2-4c** crystallized in the monoclinic space group $P2_1$ as *cis*-cofacial π-dimers aligning in a head-to-head fashion, consistent with one of the packing motifs typically exhibited by DTDA molecules described in Chapter 1. In contrast, **2-4d** crystallized in the monoclinic space group $C2/c$ as alternating *cis*-cofacial π-dimers, also frequently observed in selenzyl (DSDA) radicals.

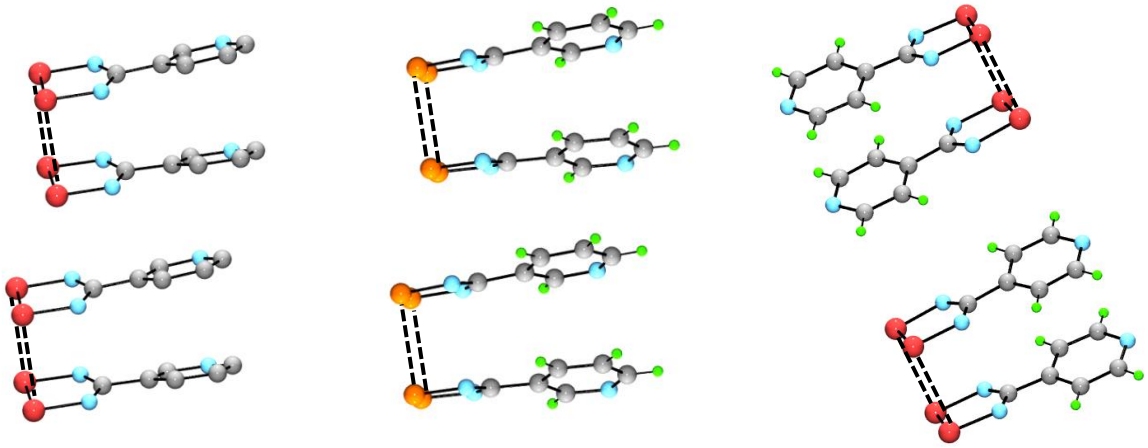

(a) (b) (c)

Figure 2.3 - Isostructural solid-state packing of (a) 3-PyDSDA **2-4c** and (b) 3-PyDTDA **2-4a** forming cofacial π-dimers in a head-to-head configuration. (c) Crystal structure of 4-PyDSDA **2-4d** illustrating π-dimers crystallizing in the head-to-tail fashion.

Table 2.1 – Crystal data of **2-4a**, **2-4c**, **2-4d**.

	$C_6H_4N_3S_2$ **2-4a**	$C_6H_4N_3Se_2$ **2-4c**	$C_6H_4N_3Se_2$ **2-4d**
M	182.24	276.04	276.04
a, Å	6.3132(4)	6.15170(10)	16.3854(12)
b, Å	15.8613(9)	16.5228(2)	9.4978(6)
c, Å	7.1082(4)	7.30130(10)	10.7059(8)
β, deg	95.801(3)	95.4320(10)	120.387(4)
V, Å	708.14(7)	738.796	1437.23
ρ_{calcd} (g cm^{-1})	1.709	2.482	2.551
space group	$P2_1$	$P2_1$	$C2/c$
Z	4	4	8
temp (K)	296	295(2)	296(2)
μ (mm^{-1})	0.622	4.968	10.214
λ (Å)	0.68890	0.71073	0.71073
data/restr./ parameters	2773/1/200	3553/1/200	2078/0/100
solution method	direct methods	direct methods	direct methods
R, R_w (on F^2)	0.0329, 0.0690	0.0226, 0.0664	0.0268, 0.0618

While all three structures form ribbon-like arrays interlaced by N---S intermolecular contacts (Figure 2.4), there are some differences between the 3- and 4-pyDTDA derivatives. Since 3-PyDTDA **2-4a** is

isostructural to 3-PyDSDA **2-4c**, only 3-PyDSDA **2-4c** and 4-PyDSDA **2-4d** are illustrated for simplicity. As can be seen from Figure 2.4, ribbons of 4-PyDSDA **2-4d** are much more coplanar than those observed for 3-PyDTDA **2-4a**.

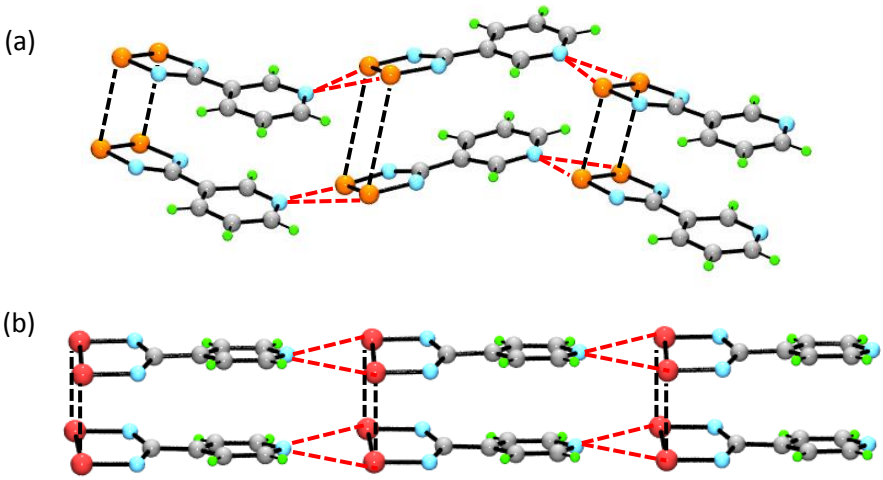

Figure 2.4 – (a) Molecular ribbons of 3-PyDTDA **2-4a** (isostructural to 3-PyDSDA) and (b) 4-PyDSDA **2-4d**. Intradimer contacts are shown in black and intermolecular S--N contacts are shown in red.

The different arrangement of molecular ribbons is a direct result of the position of the nitrogen atom. The nitrogen at the 3-position forces the ribbons to form in a sinusoidal pattern along the *a*-axis with dihedral angles between neighbouring rings of 24.48° and 19.29° for 3-PyDTDA **2-4a** and 24.02° and 26.88° for 3-PyDSDA **2-4c**. In contrast, a nitrogen atom at the 4-position allows S-N supramolecular interactions to be almost directly aligned with its neighbouring radicals affording coplanar π-stacks with a dihedral angle, ϕ, of 0° for 4-PyDSDA **2-4d**. Similar effects can be seen with the 3- and 4-cyanophenyl-DTDA shown in the earlier section. Consequently, inclusion of a nitrogen atom has a direct effect on the molecular packing of the crystal structure.

In the case of 4-PyDTDA **2-4b**, single crystals were not obtained and analysis was limited to powder X-ray diffraction obtained from Synchrotron Diamond Light Source. To our surprise, **2-4b** is not isostructural to its selenzyl cousin **2-4d**. Various solutions were obtained using DASH; the best structure obtained afforded a cell with a volume of 696 Å^3, crystallizing in the triclinic $P\bar{1}$ space group. Although a low χ factor was obtained (3.98%) using GSAS, fitting of the low angle data was quite poor using Rietveld and LeBail methods as shown in Figure 2.5.

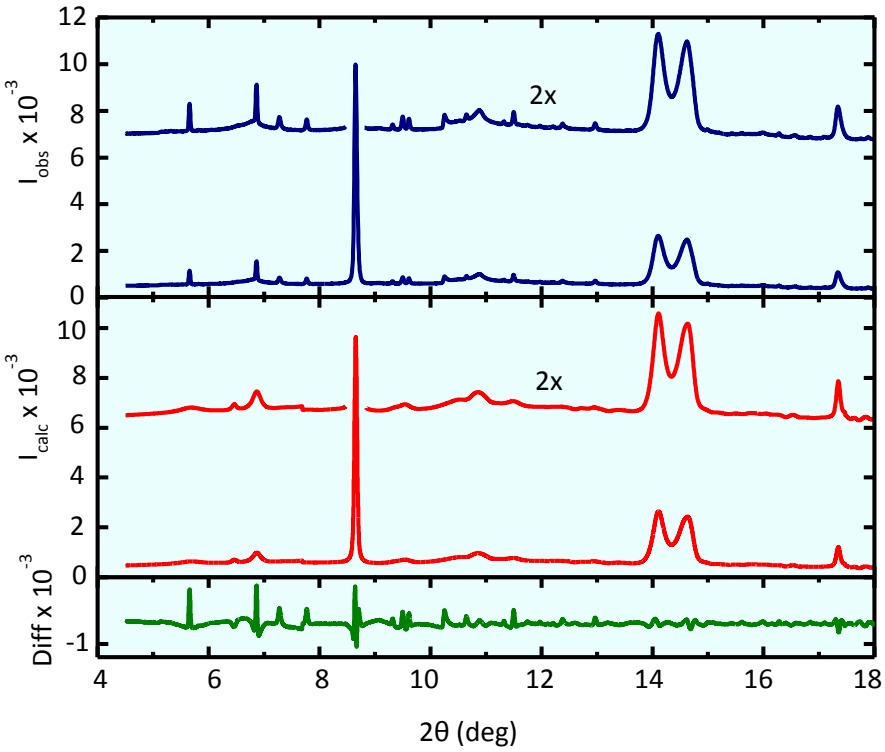

Figure 2.5 - Powder XRD of **2-4b** obtained from Synchrotron Diamond Light Source. The obtained data was refined using Rietveld methods in GSAS.

The crystal structure obtained from the Rietveld refinement indicated 4 molecules (2 dimers) in the unit cell. Crystal metrics are given in Table 2.2. Similar to the other DTDA radicals, **2-4b** associates as sulfur-sulfur dimers, arranging in a *trans*-antarafacial manner, nominally not observed in DTDA radicals. While typical S---S and S---N intermolecular contacts are seen in this structure, a large hole segregating the stacks are also observed. The experiment was repeated again with 3x sublimed material and to our surprise, a slightly -different powder pattern was obtained. However, attempts to solve the powder pattern yielded no solutions from DASH and further work must be done.

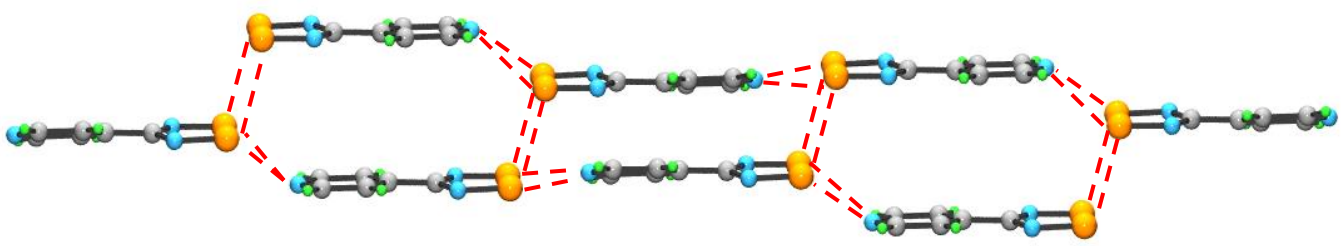

Figure 2.5 - Putative crystal structure of **2-4b** obtained from Rietveld refinement in GSAS (3.98%).

Table 2.2 – Crystal metrics of **2-4b** from Rietveld refinement in GSAS.

Formula	$C_6H_4N_3S_2$ **2-4b**
M	182.24
a, Å	7.6805(25)
b, Å	8.488(5)
c, Å	11.134(6)
α, deg	90.22(4)
β, deg	90.175(18)
γ, deg	76.80(5)
V, Å	692.8(4)
space group	$P\bar{1}$
Z	4
temp (K)	296
λ (Å)	0.82562
data/restr./parameters	2773/1/200
solution method	direct methods
R, R_w (on F^2)	0.0398, 0.0631

2.3 – Summary and Conclusion

We have successfully synthesized and characterized a new family of pyridyl-DTDA radicals **2-4a,c,d**. Satisfyingly, all three molecular systems exhibit N---S supramolecular synthons, interlacing neighbouring radicals into molecular ribbons, as predicted with the 3- and 4-cyanophenyl-DTDA radicals. All three analogues crystallize as diamagnetic dimers as a result of spin pairing, also typical for this class of radicals. In the case of 4-PyDTDA **2-4b**, further work must be pursued to obtain the crystal structure.

2.4 – Experimental Section

The same numbering scheme for the synthesis of 3- and 4-PyDTDA and PyDSDA derivatives are used in the following section.

Preparation of (*E*)-N,N,N'-tris(trimethylsilyl)isonicotinimidamide 2-6. Lithium bis-(trimethylsilyl)amide (18.0 g, 107.71 mmol) was added to a solution of 4-cyanopyridine **2-5** (10.4 g, 99.96 mmol) in 75 mL THF. The reaction was heated at reflux gently for 4 hours, cooled to rt and trimethylsilyl chloride (15 mL, 0.12 mmol) added to afford an orange precipitate. The reaction was heated at reflux for an additional 16 hours, THF subsequently removed and the obtained product purified by distillation (18.35 g, 54.42 mmol, 54% yield). ^{1}H NMR (δ, $CDCl_3$): 8.52 (d, 1H, Ar-H, *J* = 3.84 Hz), 8.49 (s, 1H, Ar-H), 7.51 (m, 1H, Ar-H), 7.19 (m, 1H, Ar-H), 0.02 (s, 9H, -Si(CH_3)$_3$). Anal. Calcd for $C_{15}H_{31}N_3Si_3$: C, 53.35; H, 9.25; N, 12.44. Found: C, 53.40; H, 9.28; N, 12.22.

Preparation of 3-(pyridin-4-yl)-1,2,3,5-dithiadiazol-1-ium 2-7. Sulfur monochloride (18.46 g, 137.72 mmol) was added to a solution of 3-PyADS **2-6** in 50 mL of freshly distilled ACE. The solution was heated at reflux for 2 hours, cooled to rt, washed with 3 x 20 mL ACE and dried in vacuo to give a bright orange solid. The product was redissolved in 20 mL of sulfuryl chloride and stirred at rt for 16 hours, washed 1 x 15 mL with DCE and pumped dry (2.45 g, 11.15 mmol, 82% yield). IR: 2072 (m), 1686 (m), 1630 (m), 1603 (m), 1421 (s), 1141 (s), 936 (m), 882 (m), 812 (s), 692 (s), 623 (m), 545 (m) cm^{-1}.

Preparation of 3-(pyridin-4-yl)-1,2,3,5-dithiadiazolyl 2-4a. Triphenylantimonyl (4.5 g, 12.75 mmol) was added to a solution of **2-7** (2.2 g, 10.11 mmol) in 30 mL of degassed ACE and stirred at rt for two hours. After the allotted reaction time, the purple precipitate was washed 3 x 10 mL with freshly distilled ACE and pumped dry to afford a dark purple powder (1.048 g, 5.78 mmol, 57% yield). Crystals suitable for crystallographic work, as well as transport property measurements, were obtained by vacuum sublimation of the bulk material at 10^{-4} Torr in a three-zone furnace along a temperature gradient of 50 to 100 °C. mp: dec > 150 °C; IR: 1587 (m), 1187 (w), 1146 (m), 1024 (m), 807 (s), 781 (s), 699 (m), 627 (w) cm^{-1}. Anal. Calcd for $C_6H_4N_3S_2$•: C, 39.54; H, 2.21; N, 23.06. Found: C, 39.36; H, 2.32; N, 23.17.

Preparation of (*E*)-N,N,N'-tris(trimethylsilyl)isonicotinimidamide 2-6. Lithium bis-(trimethylsilyl)amide (26.0 g, 155.59 mmol) was added to a solution of 4-cyanopyridine **2-5** (10.4 g, 99.96 mmol) in 75 mL THF. The reaction was heated at a gentle reflux for 4 hours, cooled to rt and trimethylsilyl chloride (15 mL, 0.118 mmol) added to afford an orange precipitate. The reaction was heated at reflux for an additional 16 hours. After the allotted reaction time, THF was removed and the obtained product purified by distillation (18.04 g, 53.50 mmol, 54% yield). mp: 45-46 °C; ^{1}H NMR (δ, $CDCl_3$): 8.55 (d, 1H, Ar-

H, *J* = 5.71 Hz), 7.13 (d, 1H, Ar-H, *J* = 5.61 Hz), 0.05 (s, 9H, -Si(CH_3)$_3$).[12] IR: 1633 (s), 1590 (m), 1548 (w), 1247 (s), 1131 (w), 997 (w), 840 (s), 757 (w) cm^{-1}. Anal. Calcd for $C_{15}H_{31}N_3Si_3$: C, 53.35; H, 9.25; N, 12.44. Found: C, 53.15; H, 9.12; N, 12.63.

Preparation of 4-(pyridin-4-yl)-1,2,3,5-dithiadiazol-1-ium 5 2-7. Sulfur monochloride (18.46 g, 137.72 mmol) was added to a solution of **2-6** in 50 mL of freshly distilled ACE. The solution was heated at reflux for 2 hours, cooled to rt, washed with 3 x 20 mL ACE and dried in vacuo to give a bright orange solid. The obtained product was redissolved in 25 mL of sulfuryl chloride and stirred at rt for 16 hours, washed 1 x 15 mL with DCE and pumped dry (2.45 g, 11.15 mmol, 82% yield). IR: 2097 (m), 1692 (w), 1633 (m), 1377 (s), 1254 (m) 1169 (m), 891 (m), 850 (s), 678 (m) cm^{-1}.

Preparation of 4-(pyridin-4-yl)-1,2,3,5-dithiadiazolyl 2-4b. Triphenylantimonyl (3 g, 8.50 mmol) was added to a solution of **2-7** (1.45 g, 6.60 mmol) in 25 mL of degassed ACE and stirred at rt for two hours. The purple precipitate was washed 3 x 10 mL with freshly distilled ACE and pumped dry to afford a dark purple powder (1.194 g, 5.48 mmol, 82% yield). Crystals suitable for crystallographic work, as well as transport property measurements, were obtained by vacuum sublimation of the bulk material at 10^{-4} Torr in a three-zone furnace along a temperature gradient of 50 to 100 °C. mp: dec > 150 °C; IR: 1597 (m), 1416 (m), 1138 (w), 1061 (w), 998 (w), 826 (w), 785 (m), 655 (m) cm^{-1}. Anal. Calcd for $C_6H_4N_3S_2\bullet$: C, 39.54; H, 2.21; N, 23.06. Found: C, 39.56; H, 2.33; N, 23.19.

Preparation of 3-(pyridin-4-yl)-1,2,3,5-diselenadiazol-1-ium 2-8 . 3-PyADS **2-6** (1.0 g, 2.96 mmol**)** was added to a solution of selenium powder (0.234 g, 2.96 mmol) and selenium tetrachloride[13] (0.654 mg, 2.96 mmol) to afford an immediate red-brown precipitate. The reaction was stirred for one hour, filtered, washed 3 x 15 mL ACE then dried in vacuo (0.860 g, 2.76 mmol, 93%). IR: 1678 (m), 1585 (w), 1187 (w), 1137 (w), 1039 (w), 1023 (w), 870 (w), 810 (w), 706 (m) cm^{-1}.

Preparation of 3-(pyridin-4-yl)-1,2,3,5-diselenadiazolyl 2-4c. Triphenylantimonyl(III) (1.2 g, 3.40 mmol) was added to a solution of **2-8** (0.860 g, 2.76 mmol) in 20 mL of bubble degassed ACE and stirred at rt under N_2 for 16 hours. After the allotted reaction time, the product was filtered, washed 3 x 15 mL freshly distilled ACE and dried in vacuo (0.754 g, 2.73 mmol, 99% yield). Crystals suitable for crystallographic work were obtained by vacuum sublimation of the bulk material at 10^{-4} Torr in a three-zone furnace along a temperature gradient of 60 to 140 °C. mp: dec > 150 °C; IR: 1584 (m), 1420 (s), 1320 (s), 1197 (m), 1129 (m), 1026 (w), 809 (w), 714 (s), 637 (m) cm^{-1}. Anal. Calcd for $C_6H_4N_3Se_2\bullet$: C, 26.11; H, 1.46; N, 15.22. Found: C, 26.18; H, 1.61; N, 15.40.

Preparation of 4-(pyridin-4-yl)-1,2,3,5-diselenadiazol-1-ium 2-8 . 2-6 (1.22 g, 3.61 mmol) was added to a solution of selenium powder (0.2345 g, 3.60 mmol) and selenium tetrachloride[14] (0.797 g, 3.61 mmol)

to afford an immediate red-brown precipitate. The reaction was stirred for one hour, filtered, washed 3 x 15 mL ACE then dried in vacuo (0.976 g, 3.13 mmol, 87%). IR: 3475 (w), 3429 (w), 3374 (w), 3322 (w), 2358 (w), 2151 (w), 1608 (m), 1235 (w), 992 (w), 721 (w) cm^{-1}.

Preparation of 4-(pyridin-4-yl)-1,2,3,5-diselenadiazolyl 2-4d. Triphenylantimonyl(III) (1.51 g, 4.23 mmol) was added to a solution of **2-8** (0.976 g, 3.13 mmol) in 20 mL of bubble degassed ACE and stirred at rt under N_2 for 16 hours. After the allotted reaction time, the product was filtered, washed 3 x 15 mL freshly distilled ACE and dried in vacuo (0.840 g, 3.04 mmol, 97% yield). Crystals suitable for crystallographic work were obtained by vacuum sublimation of the bulk material at 10^{-4} Torr in a three-zone furnace along a temperature gradient of 60 to 140 °C. mp: dec > 150 °C; IR: 1593 (m), 1412 (m), 1323 (w), 1204 (w), 1064 (w), 998 (m), 830 (m), 727 (m), 707 (w) cm^{-1}. Anal. Calcd for $C_6H_4N_3Se_2\bullet$: C, 26.11; H, 1.46; N, 15.22. Found: C, 26.24; H, 1.50; N, 15.20.

Chapter 3

Pressure Induced Phase Transitions and Metallization of a Neutral Radical Conductor

3.1 – Introduction

In the previous chapters, we discussed the use of structure-directing groups such as nitrogen in the DTDA radicals **3-1** (Chapter 2) to modify crystal packing. Also described was the use of different combinations of R_1/R_2 groups in the pyridine-bridged bisdithiazolyl radicals **3-2** to fine-tune the solid-state packing. However, the effect of these beltline ligands on bandwidth was somewhat detrimental, as their presence buffers intermolecular interactions, preventing direct superposition of the π-stacks and generating slipped π-stack architectures which compromise the bandwidth *W*. A new design strategy was therefore considered, in which the N-R fragment of **3-2** was replaced with a carbonyl moiety, to form the oxobenzene-bridged radicals **3-3** introduced in Chapter 1. A considerable number of these oxobenzene-bridged (RBBO) radicals have been reported (R = Ph, Cl, Me, F)[1] and have shown a significant improvement in conductivity relative to the pyridine-bridged radicals **3-2**.

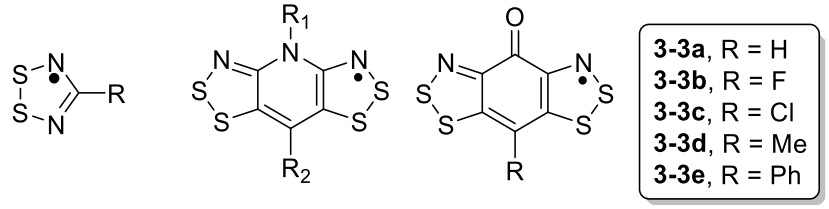

3-1 **3-2** **3-3**

As mentioned in Chapter 1, the fluorine in the fluoro-derivative **3-3b** (R = F) acts as a supramolecular synthon, interlacing the molecular ribbons in both the *x*- and *y*- direction. In pursuit of other structure-directing ligands, the prototypal radical (R = H) was considered. The use of protons as structure directing substituents, for example in hydrogen bonding,[2] is well known, and this possibility, coupled with its small size, suggested the potential for creating much more tightly bound structures.

The early oxobenzene-bridged radicals **3-3** (R = Ph, Cl, Me, F) were synthesized following the same synthetic procedure shown in scheme 3.1, commencing with the reduction of dinitrophenol **3-4** with the respective R-group to the diaminophenol **3-5** using tin(II) chloride in HCl, followed by a Herz cyclization with sulfur monochloride to give the oxobenzene-bridged framework **3-6**. Metathesis with silver

trifluoromethanesulfonate (AgOTf) and subsequent reduction with octamethyferrocene (OMFc) gave the desired radical **3-3**.

Scheme 3.1

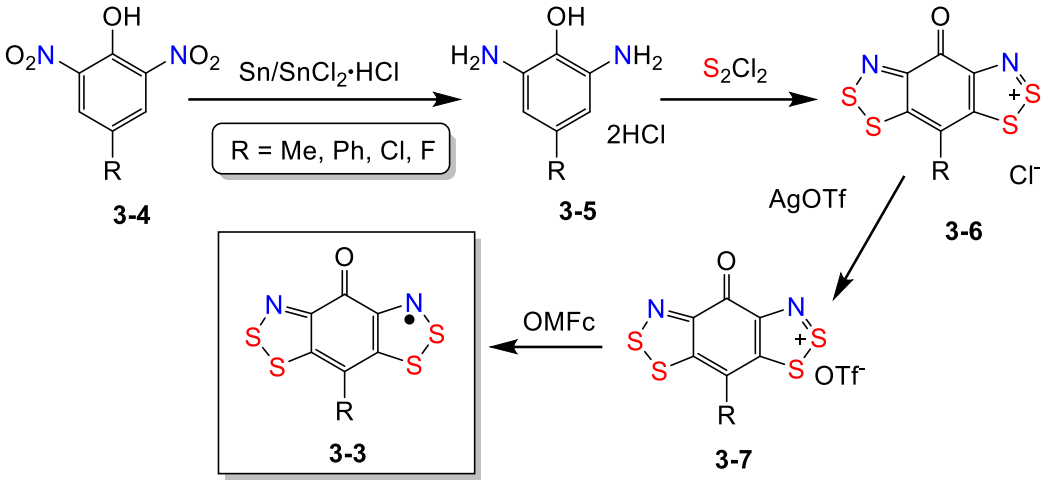

However, the synthesis and characterization of the prototypal radical remained elusive until recently, as a result of *partial* chlorination at the basal site, to afford a mixture of the proto-(**3-3a**) and chloro-variants (**3-3c**). Consequently, in the course of my thesis a new synthetic procedure was devised which bypassed this problem, and allowed the successful isolation of **3-3a**. Ambient pressure crystallography revealed a structural feature not present in the other RBBO radicals, that is, "tilted-T" or aryl C---H interactions. These interactions cause a ruffling of the ribbon-like arrays typically found for structures of this type. While this ruffling compromises bandwidth and hence conductivity, its effects could be eliminated by the application of physical pressure, which transforms the ruffled ribbons into coplanar π-stacks, and leads to eventual metallization with relatively mild loadings, as seen with **3-3b** (R = F). Moreover, these pressure dependent crystallographic studies revealed two phase changes, near 4 and 8 GPa. As a result of the structural changes, a significant increase in conductivity and a decrease in activation energy afforded a metallic state at 4-5 GPa.

The focus of this chapter is on the new synthesis and structural characterization of the prototypal oxobenzene-bridged radical **3-3a** (R = H), and the exploration of the effects of pressure on its structure and transport properties. In addition, the results of DFT calculations on the electronic structure of **3-3a** are described. As will be seen, these provide a rationale for understanding of the exceptional charge transport properties of these oxobenzene-bridged radicals. The results presented have been recently published.[3]

3.2 Results

3.2.1 – Synthesis

To prepare the desired framework **3-3a** without chlorination at the basal site, a new synthesis was devised, as illustrated in Scheme 3.2.

Scheme 3.2

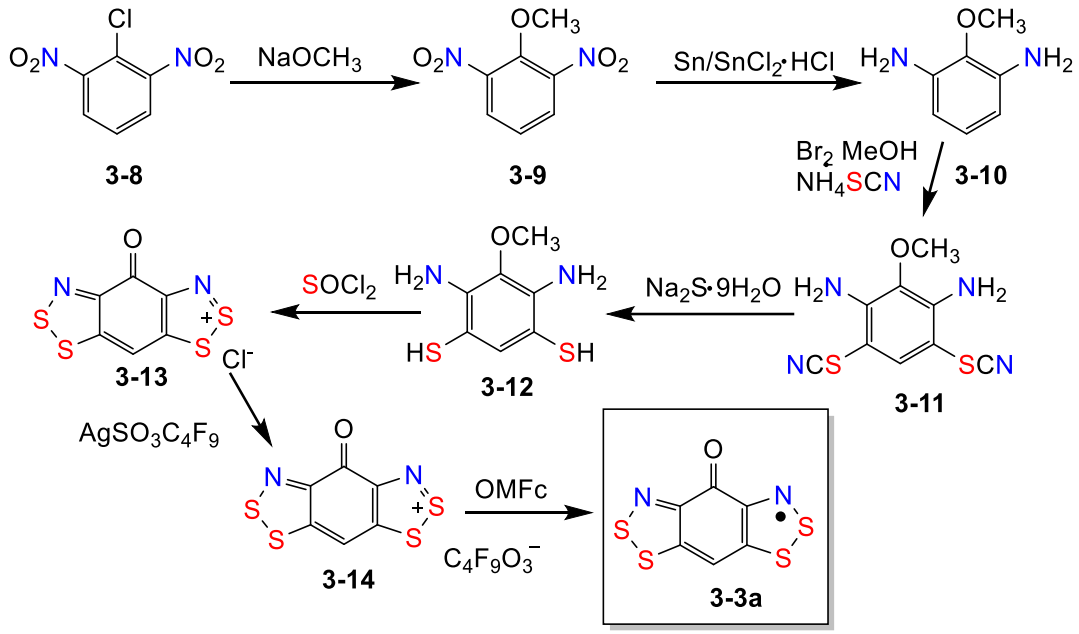

It commences with addition of sodium methoxide to a solution of 2-chloro-1,3-dinitrobenzene **3-8**, followed by a reduction with tin powder and tin(II) chloride to afford the diamino-anisole **3-10** as an orange-red oil, which solidified on standing. The product was converted to the bisthiocyanate **3-11** using ammonium thiocyanate and bromine solution, which was hydrolyzed to the dithiol **3-12** with sodium sulfide. Subsequent condensation using thionyl chloride yielded the desired framework **3-13** with no chlorination at the basal site. Metathesis with silver nonaflate (AgONf) followed by reduction with octamethylferrocene (OMFc) gave the desired radical **3-3a** (R = H). Bulk reductions were used for magnetic and conductive measurements and single crystals were obtained *via* slow diffusion H-cell techniques.

Scheme 3.3

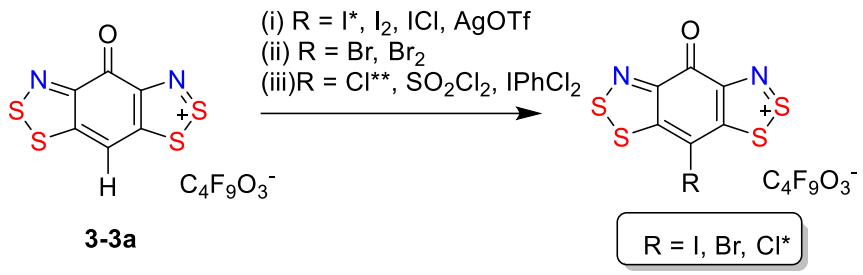

**The iodo-oxobenzene-bridged cation (R = I) was made as a triflate salt.*
***Reaction with SO_2Cl_2 and $IPhCl_2$ produced mixtures of the proto- and chloro-oxobenzene-bridged radical*

Given the availability of the prototypal bridged radical **3-3a**, we have started to explore its use as a synthetic precursor for the formation of halo-substituted derivatives, as shown in scheme 3.3. As a first step we tested the preparation, by standard electrophilic substitution procedures, of the already known bromo and chloro (R = Br, Cl) derivatives. Bromination with bromine solution yielded complete conversion, but chlorination with sulfuryl chloride and $PhICl_2$ resulted in mixtures based on infrared and mass spectroscopy. More significantly, the iodo-derivative (R = I) (which is inaccessible *via* other routes) could be cleanly synthesized using silver trifluoromethanesulfonate (AgOTf), iodochlorine (ICl) and iodine powder (I_2). These preliminary results suggest the possibility of incorporating other substituents at the basal site by electrophilic substitution of the C-H position (scheme 3.3). This work could eventually lead to the possibility of synthesizing new compounds, including the nitro and cyano (R = NO_2, CN) radicals discussed in Chapter 5.

3.2.2 – EPR and Cyclic Voltammetry

The electronic structure of **3-3a** was probed by EPR spectroscopy and cyclic voltammetry. The EPR spectrum was obtained on a sample of radical dissolved in CS_2. The appearance of the spectrum, consisting of a doublet of pentets with hyperfine coupling between the wing nitrogen atoms with a_N = 0.354 mT and to the basal hydrogen, a_H = 0.203 mT (Figure 3.1), suggests a highly delocalized spin distribution. Cyclic voltammetry was performed on a sample of **3-3a**[ONf] dissolved in MeCN, and afforded a reversible +1/0 couple with $E_{1/2}$ (0/+1) = +0.061 V *vs*. SCE and a quasi-reversible reduction wave with a cathodic peak potential, E_{pc}, at -0.525 V *vs* SCE. The difference between the E_{pc} couple provides an estimate of the cell potential, E_{cell}, of 0.56 V, a significant improvement compared to the pyridine-bridged **3-2** molecular systems at 0.7 V.

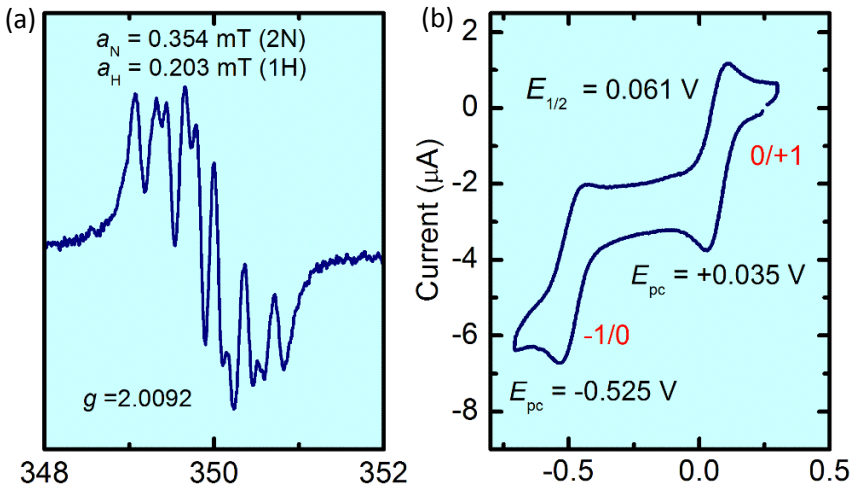

Figure 3.1 - (a) X-band EPR spectrum of **3-3a** in CS_2. (b) Cyclic voltammetry scan of [**3-3a**][ONf] with Pt electrodes, 0.1 M *n*-Bu_4NPF_6 electrolyte, scan rate 100 mV s^{-1}.

3.2.3 – Ambient Pressure Crystallography on HBBO

Single crystal X-ray diffraction data on microcrystals of **3-3a** were collected using Synchrotron radiation (Diamond Light Source, UK). The structural solution revealed an orthorhombic space group *F*dd2. The unit cell, shown in Figure 3.2, consists of 16 molecules (*Z* = 16), each of which forms the basis for a slipped π-stacked array running down the *c*-axis. Similar to the other RBBO derivatives (R = F, Cl, Ph), these form ribbon-like arrays held together by S---N and S---O intermolecular contacts.

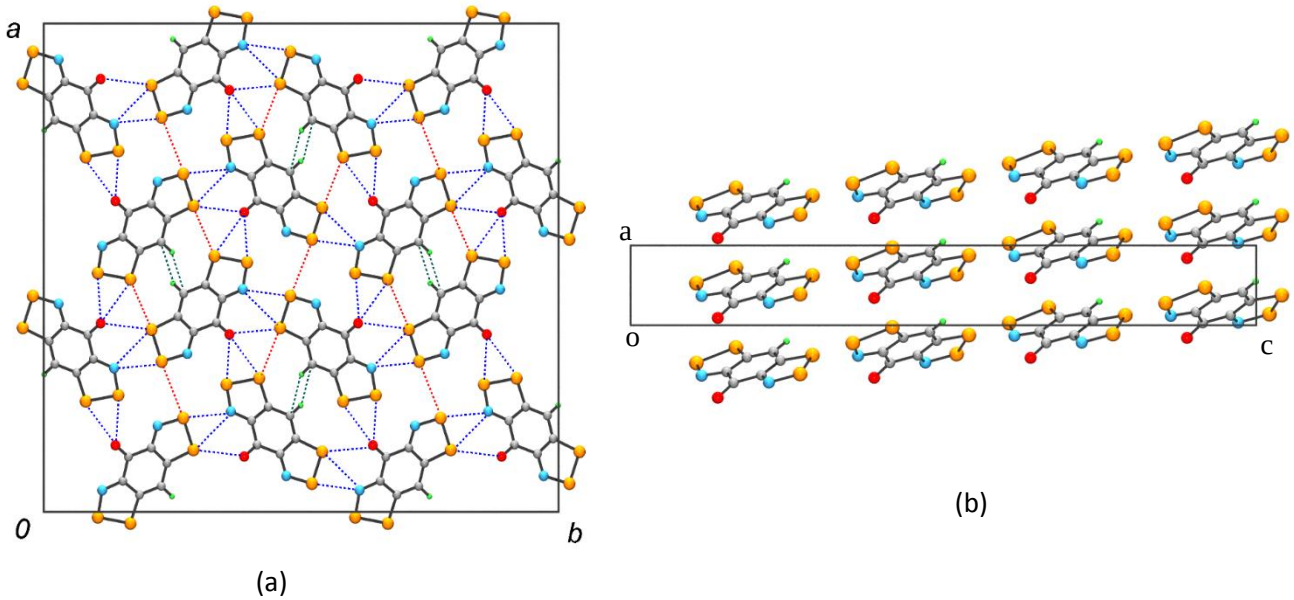

Figure 3.2 – (a) Unit cell of **3-3a**, with ribbon-like arrays of radicals following the d-glide planes. S ---O and S---N contacts are shown in blue, S---S contacts in red and CH---C contacts in green. (b) Slipped π-stacks running along the *c*-axis.

While the projection shown in Figure 3.2 suggests architectural similarities with other radicals of this type, that is, intersecting ribbon-like arrays, there are some new features, the most important of which are the edge-to-face or "tilted-T" CH---H interactions connecting radicals along the 2_1 axes, as seen in Figure 3.3. These interactions force the molecules out of coplanarity, causing a ruffling in the otherwise planar ribbons present in similar type radicals. The extent of the ruffling can be defined by the dihedral angles, ϕ_{bc} and $\phi_{ac,}$ formed perpendicular to both the *x*- and *y*-directions. Supramolecular metrics are given and discussed in section 3.2.6.

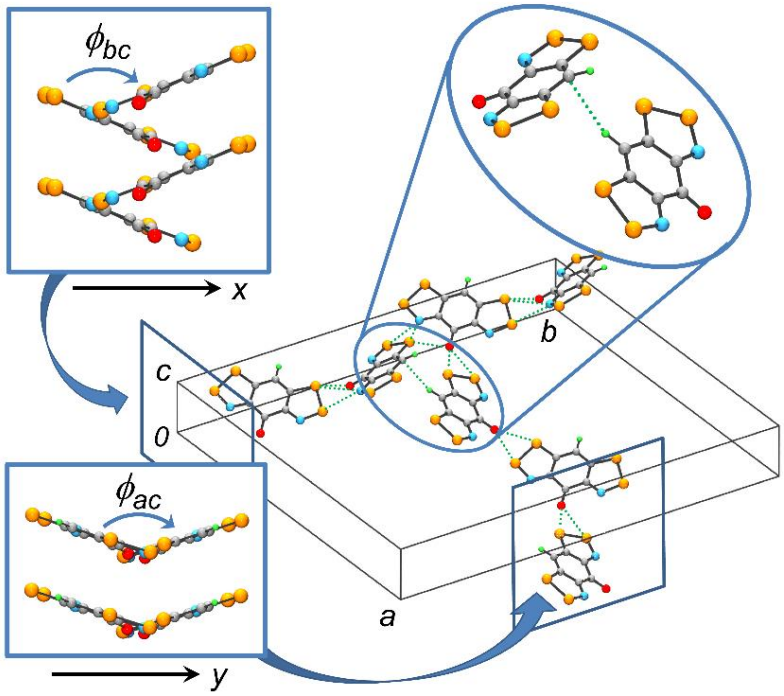

Figure 3.3 –Ruffling of the ribbons of **3-3a** as result of "Tilted-T" CH---H interactions perpendicular to the *x*- and *y*-directions.

In pursuit of a two-dimensional (2D) brick-wall packing motif similar to **3-3b** (R = F), and as such, a metallic state, **3-3a** was subjected to high-pressure studies which will be discussed in section 3.2.6.

3.2.4 – Magnetic Susceptibility

DC magnetic measurements were performed over the temperature range 2 – 300 K using a SQUID magnetometer. Initial field-cooled measurements at 1 kOe (Figure 3.4) indicated Curie-Weiss behavior, and a fit to the data from 30 – 300 K provided a C-constant of 0.364 emu mol^{-1} and a large FM θ value of +15.6 K. A sharp increase is seen in χ and χT at 10 K reaching a maximum around 5 K before declining, suggestive of spin-canted antiferromagnetic (AFM) behavior below this temperature.

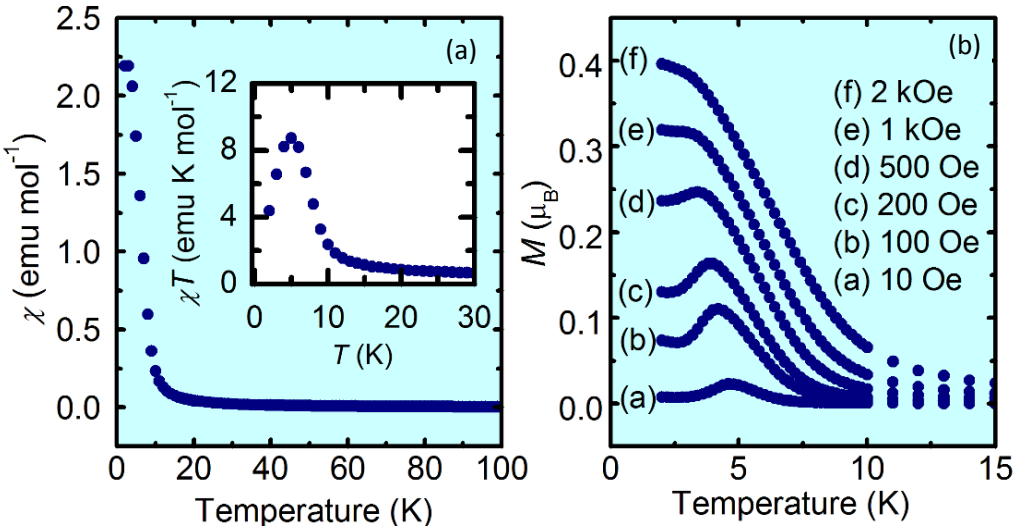

Figure 3.4 - (a) Magnetic susceptibility (χ) measurements of **3-3a** suggestive of antiferromagnetic ordering below 5 K. (b) Isothermal magnetization over a range of fields, with ferromagnetic ordering above 1 kOe.

Magnetization (*M*) measurements as a function of temperature over a range of magnetic fields were also analyzed. At fields below *H* = 1 kOe, the ground state is predominantly AFM coupled, while exposure to higher fields (*H* > 1 kOe) result in a field-induced realignment to produce a ferromagnetic (FM) state readily seen at a field of 2 kOe, consistent with metamagnetic[4] behavior. From the maximum of the magnetization (*M*) plot, an ordering temperature T_N was estimated to be 4 K, which was supported with AC magnetic susceptibility measurements.

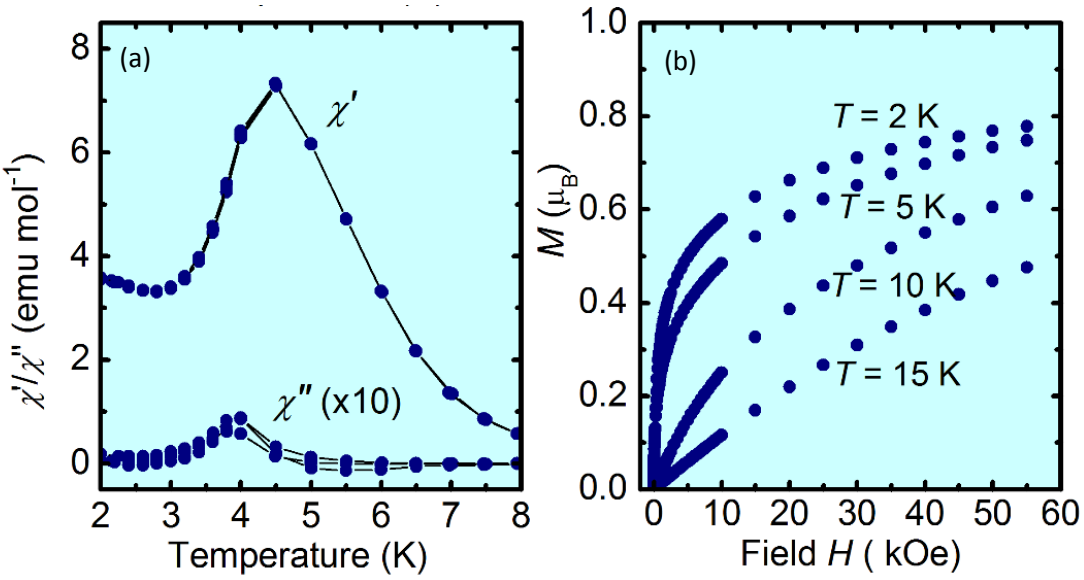

Figure 3.5 – (a) AC in-phase (χ) and out-of-phase (χ”) magnetic measurements of **3-3a** at 10, 100, 1000 Hz (b) Magnetization (M) plots as a function of field over a range of temperatures.

The in-phase (χ’) and out-of-phase (χ”) AC magnetic susceptibility measurements were conducted over frequencies of 0.1 – 1 kHz. A clear maximum at 4.5 K is observed for the in-phase χ’ and a much weaker response at 4 K from the out-of-phase χ’’ is shown. Nevertheless, both curves display similar ordering temperatures which are invariant to frequency.

Isothermal magnetization measurements revealed typical paramagnetic behavior above 15 K. However, temperatures below 15 K display a significant increase in magnetization similar to that seen in other radicals undergoing field-induced FM ordering.[5] However, full FM saturation M_{sat} = 1 μ_B was never achieved, even at temperatures as low as 2 K, where *M* reached only about 80% of the full saturation value. At first glance, this may seem unusual especially for a *S* = ½ system, but the complexity of the structure involving numerous magnetic exchange interactions along with a high T_N/θ value of 0.3 may be a result of a spin frustrated system, as seen in many organic charge-transfer salts.[6]

Based on the observed spin-canting behavior of **3-3a,** we can deduce three possible magnetic structures based on symmetry arguments, shown in Figure 3.6. In all cases, interactions between the radicals along the same π-stacks are ferromagnetic as a result of translational symmetry forming FM chains along the *c*-axis. Ferromagnetic coupling can also occur along the molecular ribbons following the *a*-axis (Figure 5.6a) or *b*-axis (Figure 5.6b). The last candidate consists of ferromagnetic coupling with

respect to a two-fold or a 2_1 axis. While we cannot infer on the correct mode of magnetization, the prominence of ferromagnetic interactions is consistent with a positive Weiss constant of +15.6 K.

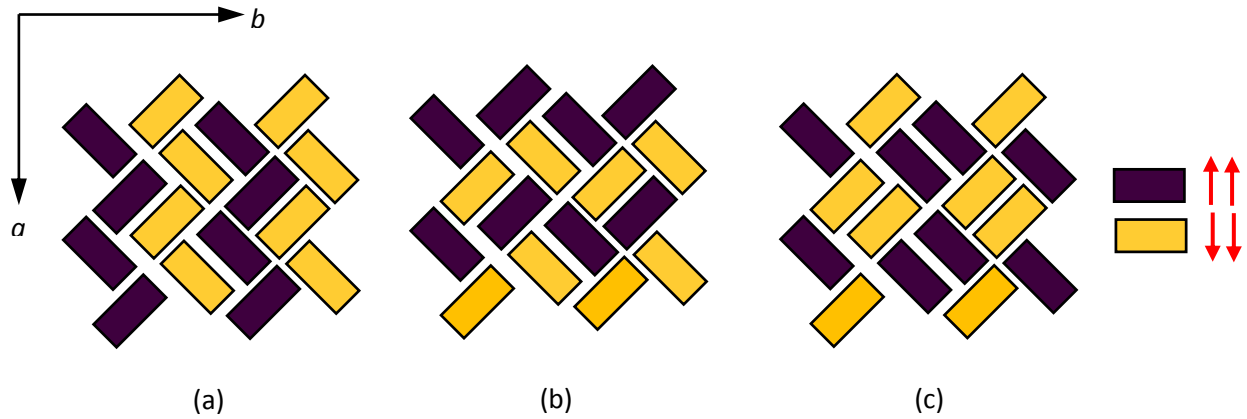

Figure 3.6 – Possible modes of magnetization of **3-3a**, where purple and yellow blocks represent spin-up and spin-down domains, respectively. (a) Ferromagnetic interactions along the *a*-axis, (b) along the *b*-axis, and (c) ferromagnetic coupling related by two-fold or a 2_1 axis.

3.2.5 – Variable Temperature Conductivity

Variable temperature conductivity (σ) measurements (Figure 3.7) were performed using the 4-probe method on cold-pressed pellets. Log σ versus 1/*T* plots of the RBBO family are plotted for comparison. As may be seen, the conductivity of the RBBO family is three orders of magnitude greater than that of the pyridine-bridged series, with [**3-3b**] (R = F) lying at the top of the pack, followed closely by [**3-3a**] (R = H) at 6 x 10^{-3} S cm^{-1}. However, the latter material possesses a thermal activation energy E_{act} of 0.16 eV, slightly higher than the average observed for other RBBO radicals. While **3-3b** (R = F) consist of a two-dimensional brick wall architecture with interactions both in the *x*- and *y*-direction, **3-3a** (R = H) consists of ruffled-ribbons which disrupt the ribbon coplanarity and result a more one-dimensional electronic structure, heralding a lower conductivity and higher activation energy. Nevertheless, a more two-dimensional network may be achieved by compressing the ruffled ribbons. The results of pressured dependent crystallographic and conductivity measurements designed to test this possibility will be discussed in the following section.

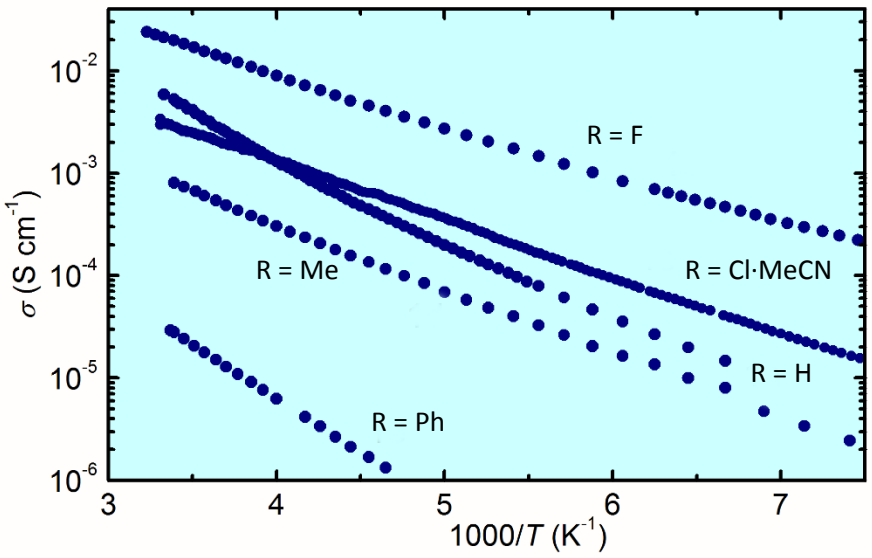

Figure 3.7 - Variable temperature conductivity of the oxobenzene-bridged radicals **3a-e**.

3.2.6 – High Pressure Crystallography

The effect of pressure on the structure of **3-3a** was examined using Diamond Anvil Cell (DAC) techniques and synchrotron radiation (Spring-8, Japan). Numerous powder diffraction data sets over the range of 0 – 13 GPa were collected and solved using DASH, revealing three distinct powder patterns suggestive of three different phrases (Figure 3.7). The first phase, or the α-phase, was solved by single crystal X-ray crystallography at ambient pressure discussed in the previous section. The structural solutions for the remaining two phases were refined in GSAS using Rietveld[7] and Le Bail[8] methods. Crystal data for each phase is given in Table 3.1.

Table 3.1 - Crystal Data for α-, β-, and γ-phase over 0 – 13 GPa.

P, GPA	0	1.8	4.4	6.0	9.8	11.1	13.0
Phase	α	α	β	β	γ	γ	γ
Formula	$C_6HN_2SO_4$	$C_6HN_2SO_4$	$C_6HN_2SO_4$	$C_6HN_2SO_4$	$C_6HN_2SO_4$	$C_6HN_2SO_4$	$C_6HN_2SO_4$
M	245.33	245.33	245.33	245.33	245.33	245.33	245.33
a, Å	27.873(3)	26.436(2)	13.211(3)	12.880(2)	13.063(2)	13.001(2)	12.919(2)
b, Å	1.252(3)	29.579(3)	15.162(4)	14.888(4)	14.945(3)	13.909(3)	13.842(2)
c, Å	4.004(5)	3.6728(2)	3.3733(6)	3.2737(5)	3.0230(3)	2.9950(3)	2.9619(3)
V, Å^3	3485.2(7)	2872.0(2)	675.7(2)	627.7(2)	590.2(1)	580.5(1)	567.9(1)
P_{calcd} (g cm^{-1})	1.870	2.270	2.412	2.596	2.761	2.807	2.870
Space group	*Fdd*2	*Fdd*2	*Pbn*2$_1$	*Pbn*2$_1$	*Pbn*2$_1$	*Pbn*2$_1$	*Pbn*2$_1$
Z	16	16	4	4	4	4	4
Temp(K)	296(2)	293(2)	293(2)	293(2)	293(2)	293(2)	293(2)
λ (Å)	0.6889	0.41337	0.41337	0.41337	0.41337	0.41337	0.41337
Solution method	Direct methods	Powder Data[a]	Powder Data[b]	Powder Data[b]	Powder Data[a]	Powder Data[a]	Powder Data[a]
R_f, R_w	0.235, 0.0524	0.0046, .0061	0.0063, .0111	0.0049, .0085	0.0059, 0.0083	0.0062, 0.0087	0.0056, 0.0076

[a]Rietveld refinement. [b]Le Bail refinement.

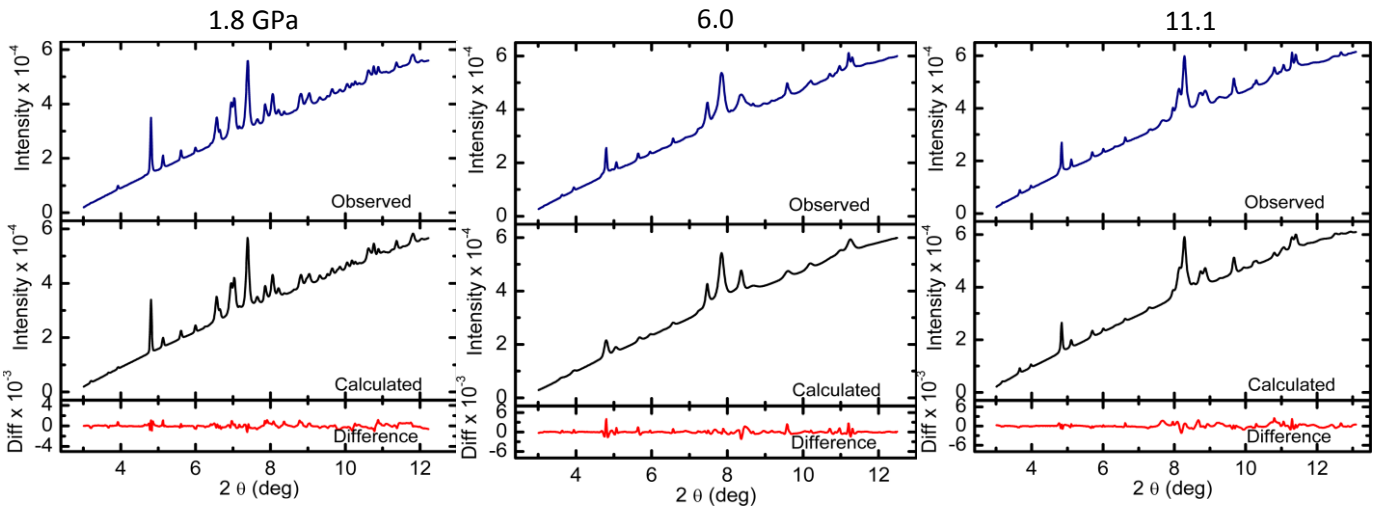

Figure 3.8 – Powder XRD on **3-3a** collected from 0 – 13 GPa illustrating the presence of three different phases.

To understand the structural transformations, the relative cell dimensions were analyzed as a function of pressure; the results are plotted in Figure 3.9. Upon compression, the unit cell volume decreases rapidly along with the *c*-axis in response to the ease of compressibility of the π-stacks. At 3-4 GPa, a substantially different powder pattern is observed, suggestive of the formation of a second, or β-phase. Initial cell indexing and structural refinement indicated the loss of *F*-centering, with two viable space groups, $Pbn2_1$ and $Pna2_1$. In both space groups the original *d*-glide found in the α-phase transforms into either an *n*-glide in $Pbn2_1$ or an *a*- or *b*-glide for $Pna2_1$, depending on the cell setting. The choice between these two space groups was determined from Le Bail refinements of all model solutions generated by DASH. Ultimately, successful solutions for all data sets were only obtained for the space group $Pbn2_1$.

The transition from a highly symmetric space group *Fdd*2 to $Pbn2_1$ follows a loss in *F*-centering and as such halving of both the *a*- and *b*-axis to afford $Z = 4$ from $Z = 16$ in the *α*-phase. A representative cell drawing at 6.0 GPa is shown in Figure 3.10. From 4 – 8 GPa, the β-phase undergoes a pancake-like collapse where the cell volume and *c*-axis declines and the *a*- and *b*-axis elongates.

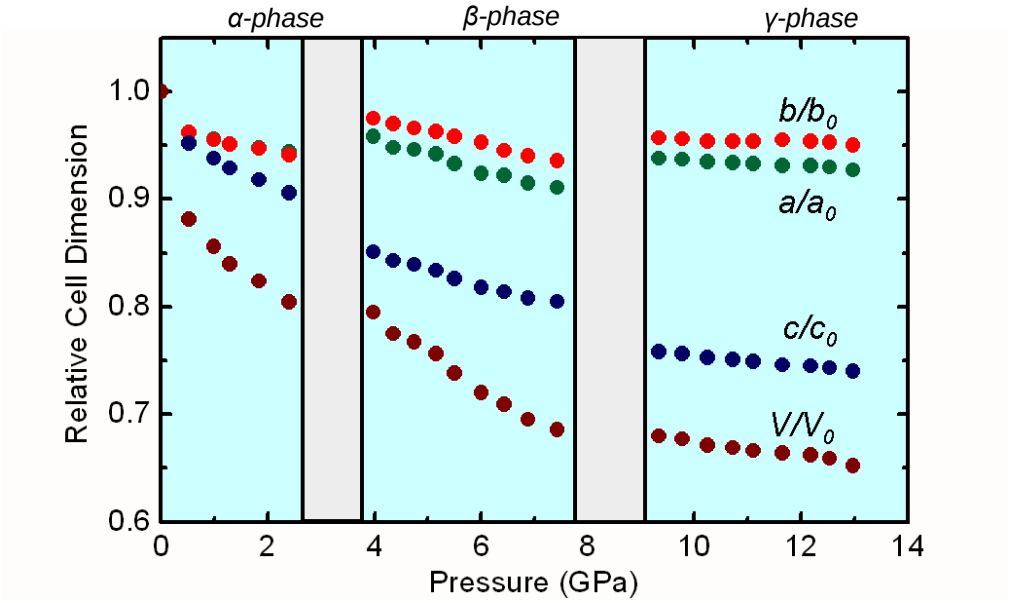

Figure 3.9 - Relative cell dimensions of **3-3a** as a function of pressure at room temperature, where a_o, b_o, c_0, and v_0 are crystal dimensions of **3-3a** at ambient pressure. The *a*- and *b*-axis of the β- and γ-phase are scaled to allow comparison to the α-phase.

Further compression to 8 GPa gave rise to a third phase transition where the unit cell continues its pancake-like collapse. However, the compressibility of the γ-phase decreases as it is produced, with little change in the cell dimensions as a function of pressure. While there is no change in the space group ($Pbn2_1$) between the crossover of the β- and γ-phase, the differences reside in the arrangement of the π-stacks.

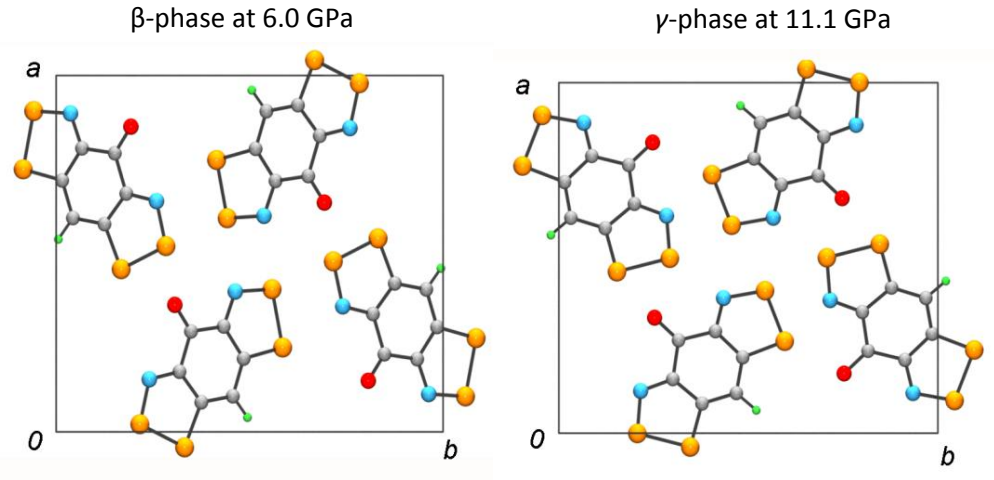

Figure 3.10 - Representative cell drawing of the β-phase at 6.0 GPa and γ-phase at 11.1 GPa of **3-3a**.

To further characterize the differences between the three phases, the degree of slippage in the π-stacks for each phase was analyzed. To this end, the mean intermolecular separation between the π-stacks, δ, and the inclination angle relative to the *c*-axis, τ, are summarized in Table 3.2. As pressure is applied, the mean intermolecular spacing δ decreases as expected, with a remarkable decline from the α-β transition. However, the differences between τ are more subtle. A small increase is seen from the α- to β-phase transition followed by a much larger decrease in the β- to γ-phase transition.

Table 3.2 - Supramolecular metrics for **3-3a**.

Phase	Pressure (GPa)	δ (Å)	τ (°)	Φ_{bc} (°)	Φ_{ac}(°)
α	0	3.47	29.8	135.7	142.4
α	1.84	3.23	28.5	137.7	143.6
β	4.4	2.84	32.8	177.5	114.5
β	6.0	2.80	31.1	179.9	117.8
γ	9.8	2.83	20.8	138.6	169.5
γ	11.1	2.80	21.0	139.1	170.6
γ	13.0	2.77	20.6	140.5	168.7

To illustrate the structural differences between the β- and γ-phase, unit cell drawings at 6.0 and 11.1 GPa are shown in Figure 3.11. In the β-phase, slipped cross-braced π-stacks are formed perpendicular to the *bc*-plane. The near 180° dihedral angle $\Phi_{bc,}$ defined in section 3.2.3, suggests the presence of superimposed π-stacks along the ribbon-like arrays. In contrast, the transition to the γ-phase yields slipped cross-braced π-stacks perpendicular to the *ac*-plane.

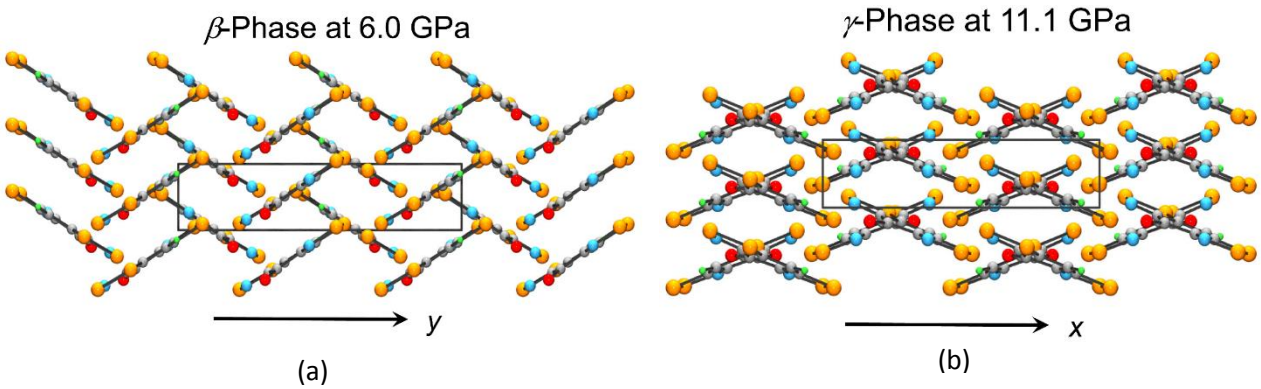

Figure 3.11 – (a) Cross-braced slipped π-stacks of **3-3a** perpendicular to the *bc*-plane of the β-phase and (b) slipped π-stacks of the γ-phase perpendicular to the *ac*-plane.

While there is no definitive explanation for the switching of the cross-braced π-stacks perpendicular to *bc*-plane in the β-phase to the *ac*-plane in the γ-phase, a large offset in the neighbouring radicals in the *y*-direction can be readily seen in the β-phase, but are not present in the γ-phase in the *x*-direction, possibly as a result of more efficient packing at higher pressures.

3.2.7 - High Pressure Conductivity

The ambient pressure, variable-temperature four-probe conductivity (σ) was reported earlier in section 3.2.5, peaking at 6 x 10^{-3} S cm^{-1} with an activation energy E_{act} of 0.16 eV. To explore the effects of pressure on these two parameters, high pressure variable-temperature conductivity was carried out using a 3000 ton cubic anvil press (CAP) to scan over the range 0 – 12 GPa.

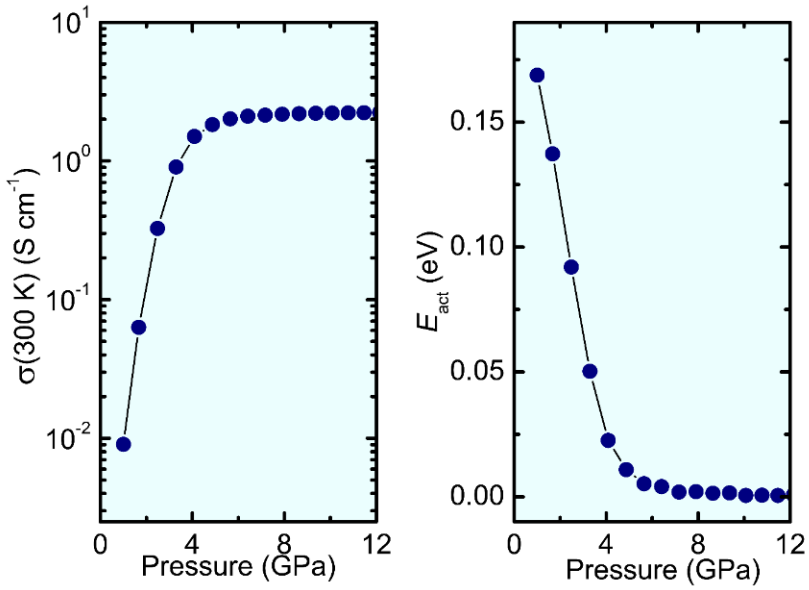

Figure 3.12 - Variable temperature conductivity (left) and activation energy (right) of **3-3a** as a function of pressure.

As can be seen in Figure 3.12, the conductivity increases rapidly peaking at 2 x 10^{0} S cm^{-1} at 6 GPa before plateauing with little change at higher pressures. At the same time, the activation energy E_{act} was monitored over the same range of pressures. Upon compression, the activation energy drops sharply, reaching zero at 6 GPa suggestive of the formation of a weakly metallic state. We interpret these changes in terms of a conversion from a Mott insulator to a weak metallic state, which can be seen during the α-β transition.

3.2.8 - High Pressure Infrared Spectroscopy

To investigate the pressure-induced metallization of **3-3a**, the solid-state infrared absorption and reflectance spectra was obtained using Diamond Anvil Cell (DAC) techniques as shown in Figure 3.13. At low pressures, distinct molecular vibrational modes are visible, with the carbonyl C=O at 1600 cm^{-1} being the most prominent. As higher pressure is applied, the peaks gradually broaden and eventually disappear at 4.1 GPa, as would be expected with the approach of a metallic state.

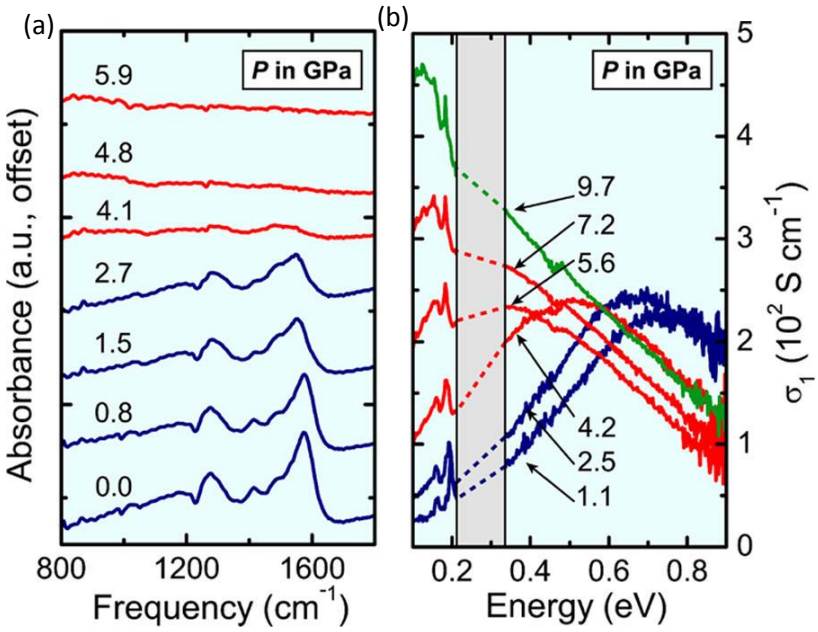

Figure 3.13 – (a) Ambient temperature absorption spectra of **3-3a** as a function of pressure and (b) ambient temperature optical conductivity of **3-3a** as a function of pressure. The various colours indicate the different phases: blue – α-phase, red – β-phase, green – γ-phase.

The ambient temperature optical conductivity was obtained by measuring the reflectivity as a function of pressure. Below 4 GPa (blue), the optical conductivity approaches 0 at low frequencies, consistent with insulating behaviour. Upon compression of the β-phase between 4-7 GPa, a significant increase in conductivity is observed at low frequencies, suggestive of closure of the Mott-gap and the onset of a correlated metallic state. In this present experiment, Drude-like features expected for metallic metals are not present over the frequency range monitored. Commonly, these Drude-like features appear below ~ 200 cm^{-1} (25 meV),[9] although thermal fluctuations may broaden and smear out these peaks.[10]

3.3 – Molecular Electronic Structure

To understand the remarkable differences of the oxobenzene-bridged radicals **3-3** relative to the pyridine-bridged bisdithiazolyl radicals **3-2**, the electronic structure of both systems were probed by a series of calculations using Density Functional Theory (DFT) at the (U)B3LYP/6-311G(d,p) level. The origin of the set of HOMO, LUMO, and SOMO molecular orbitals can be imagined as coupling between two dithiazolyl (DTA) SOMOs through the p_π orbital of the basal carbon. In C_{2v} symmetry, there are two SOMO combinations of a_2 and b_1 symmetry. However, only orbitals of b_1 symmetry can mix with the p_π of the carbon, also of b_1 symmetry. Consequently, mixing affords an in-phase (bonding) combination and an out-of-phase (antibonding) combination above and below the unperturbed a_2 orbital, which becomes the SOMO of the hypothetical acyclic precursor in Figure 3.14.

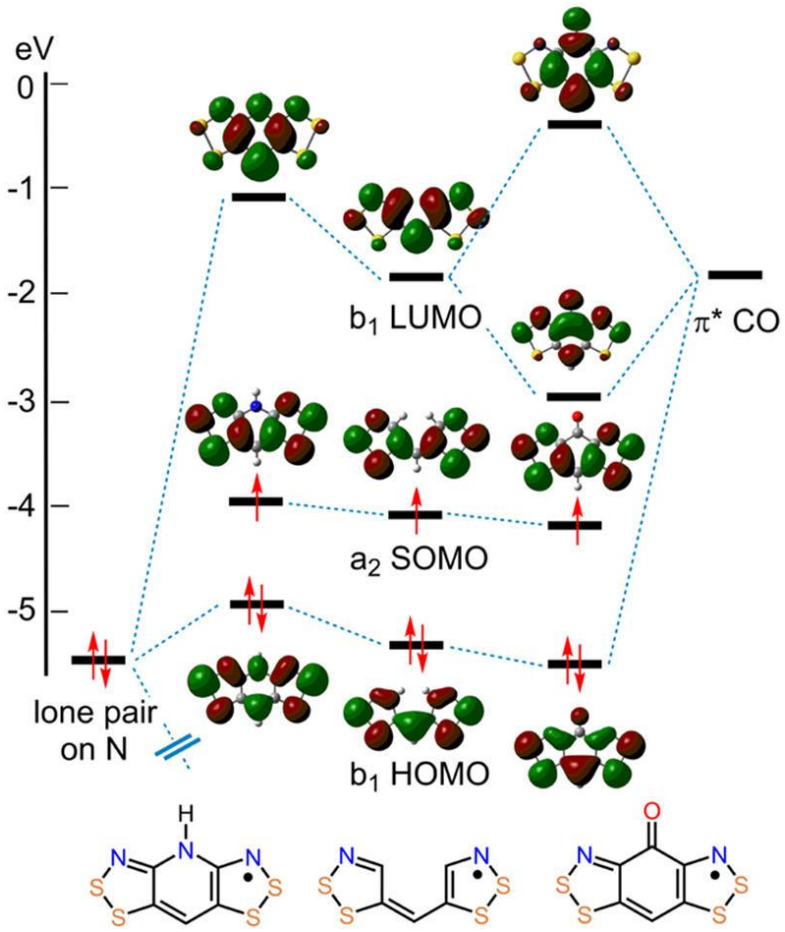

Figure 3.14 – Molecular correlation diagram using (U)B3LYP/6-311(d,p) showing the frontier orbitals of pyridine-bridged **3-2** (left), oxobenzene-bridged radicals **3-3** (right), starting from a common acyclic radical precursor (center).

The electronic effects of incorporating an N-R and carbonyl fragment was then probed by a series of DFT calculations at the (U)B3LYP/6-311G(d,p) level. Little change was observed, to first-order approximation, in the SOMOs of either fragments relative to the precursor. As such, the spin distributions and EPR spectra of both **3-2** and **3-3** radicals are fairly similar, with hyperfine coupling constants, a_N, one-half of those found in mono-dithiazolyl (DTA) systems, as expected for coupling between two DTA rings.[11] Moreover, the presence of a nodal plane at the basal carbon allows any substituent to be at this position with little variation in the a_N values. However, there are some subtle changes to orbital energies when electron repulsion effects are taken into account. For example the pyridine-bridged **3-2** SOMO is slightly higher in energy than the oxobenzene-bridged **3-3** SOMO.

The differences between the two systems are more evident in their excited state ion energetics. Incorporation of a nitrogen lone pair into the precursor allows strong mixing between the HOMO and LUMO of the precursor and the nitrogen lone pairs, forming antibonding combinations which are both higher in energy. In contrast, inclusion of a carbonyl moiety introduces an empty π* orbital, which strongly mixes with the LUMO of the precursor, lowering its energy substantially to form a low-lying LUMO. The carbonyl π-orbital is also capable of mixing with the LUMO of the precursor, however, it is much lower in energy and thus does not contribute much to the orbital energies. At the same time, the π* orbital also mixes weakly with the HOMO of the precursor, dropping in energy and thus widening the SOMO-HOMO gap. This is readily apparent in the absorption optical spectra of the cations of both systems, which will be discussed in more detail in Chapter 5, where the previously occupied SOMO is now empty. Excitation from the HOMO-LUMO is considerably red-shifted for the pyridine-bridged **3-2** cations compared to the oxobenzene-bridged bisdithiazolyl **3-3** cations, consistent with a much smaller optical gap for the latter system.

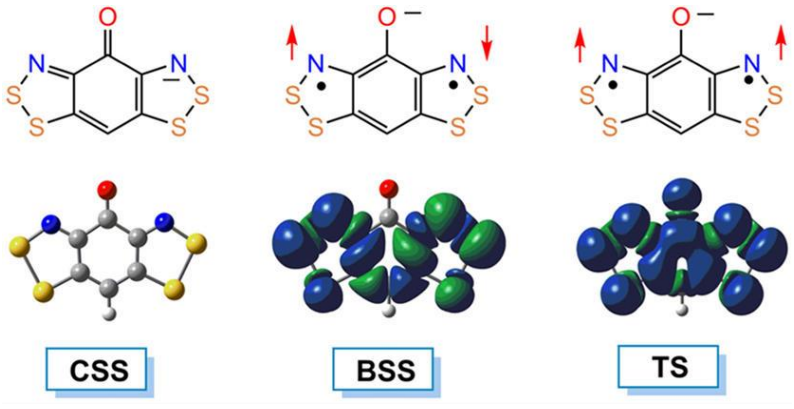

Figure 3.15 - Closed-shell singlet, broken symmetry singlet, and triplet state ions of **3-3a**.

The consequences of the presence of a low-lying LUMO and, as such, a small SOMO-LUMO gap, suggests the reduction of the radical to the anion may afford an open-shell triplet state, as seen with related antiaromatic biscyanine dyes.[12] To explore this possibility, DFT calculations were done on the closed-shell singlet (CSS) and the triplet state (TS) at the (U)B3LYP/6-311G(d,p) level (Figure 3.15). The open-shell singlet (OSS) could not be calculated directly, but was accessed by utilizing the broken symmetry singlet state method to calculate the broken symmetry singlet state (BSS), as described in Chapter 1.

Table 3.3 - Relative State Energies[a] of **3-3a**$^-$ (TS) for the BSS, OSS, and CSS in kcal mol^{-1}.

	E^{TS} ($<S^2>$)	E^{BSS}($<S^2>$)	E^{OSSb}	E^{CSS}
Gas phase	0 (2.024)	0.70 (0.830)	1.17	4.79
PCM (MeCN)[c]	0 (2.027)	2.70 (0.956)	5.05	9.50

[a](U)B3LYP/6-31G(d,p) energies in kcal mol^{-1} of the CSS, BSS, and OSS states, relative to the TS state. The $<S^2>$ states are given in parenthesis [b]$E_{OSS} = E_{TS} - 2[E_{TS}-E_{BSS}]/<S^2>_{BSS}-<S^2>_{BSS}]$. [c]PCM with MeCN solvent.

Table 3.3 displays the energies of all four states relative to that of the triplet state, as obtained from gas phase and polarized continuum model (PCM) calculations (the latter with acetonitrile as the solvent, as in the electrochemical work). The data indicate a substantial increase in stability in the open-shell states relative to the closed-shell singlet. The lowest energy state is predicted to be the open-shell triplet state which, an effect which is enhanced when solvation effects are applied, as expected from its large molecular dipole moment (μ = 5.80 D, gas phase) compared to the CSS anion (μ = 3.25 D, gas phase)**.** The extra stabilization of the anion can be attributed to the low-lying b_1 orbital, not present in the corresponding anion of the N-alkyl systems. Moreover, additional stabilization arises from Hund's rule coupling between the a_2 and b_1 orbitals, another feature not present in the pyridine-bridged **2-2** systems, which typically possess CSS ground states.

Using the calculated values in Table 3.3, the electron affinity (EA) was calculated for each of the 4 states, both with and without solvation (PCM) effects. These numbers, together with the calculated ionization potential (*IP*) data, were then used to calculate the disproportionation energy ΔH_{disp} of the CSS, OSS, and TS states, and hence to estimate the energy barrier *U* to charge transport. In the case of the pyridine-bridged **3-2** molecular systems, the absence of a low-lying π-LUMO allows only the closed-shell anion to be accessed. However, in the case of the oxobenzene-bridged radicals **3-3**, OSS and triplet anions are plausible by virtue of a low-lying LUMO, with the latter being stabilized by strong Hund's rule coupling,[13] giving rise to a high electron affinity (EA) and hence a low ΔH_{disp} (Table 3.4).

Table 3.4 - Calculated Ion Energetics (eV) and Electronic Potentials (V) for N-R and C=O Radicals.

	3-1		**3-3**	
	Gas phase	PCM (MeCN)	Gas phase	PCM (MeCN)
IP	6.16	4.41	6.51	4.61
EA^{CSS}	1.58	3.24	1.83	3.38
EA^{OSS}	---	---	1.99	3.57
EA^{TS}	---	---	2.04	3.79
$\Delta H_{disp}{}^{CSS}$	4.59	1.17	4.68	1.23
$\Delta H_{disp}{}^{OSS}$	---	---	4.52	1.04
$\Delta H_{disp}{}^{TS}$	---	---	4.47	0.82
$E_{1/2}$ (0/+1)	-0.130 (-0.170)[b]		0.061 (0.035)[b]	
$E_{1/2}$ (-1/0)	-0.946[c]		-0.525[c]	
E_{cell}	0.78[d]		0.56[d]	

[a]DFT calculations at the (U)B3LYP/6-311G(d.p) level for IP, EA, and disproportionation enthalpies (ΔH_{disp} = IP – EA) all in eV for CSS, OSS, and TS. [b]Cathodic peak potential in parenthesis. [c]Irreversible reduction, E_{Pc}. [d]E_{cell} estimated by $|E_{pc}(0/+1) – E_{pc}(-1/0)|$

While the differences between the two systems are only marginal in the gas phase, inclusion of solvation effects (MeCN) amplifies the differences, and reproduces at least qualitatively, the experimental E_{cell} values. Overall, the oxobenzene-bridged radicals are softer by virtue of the higher electron affinity which can be attributed to the presence of a low-lying LUMO.

3.4 - Discussion

Incorporation of a carbonyl moiety to afford the oxobenzene-bridged bisdithiazolyl radicals provides a new family of radicals forming ribbon-like arrays held together by S---N' and S---O' supramolecular synthons. The differences in charge transport properties can be attributed to the way these molecular ribbons are packed, ranging from strongly 1D, as in **3-3e** (R = Ph), to strongly 2D, as seen in **3-3b** (R = F). In the case of **3-3a**, the ribbons are ruffled due to the additional CH---C' interaction not present in the other RBBO radicals, giving rise to a more 1D electronic structure. Consistently, its ambient pressure conductivity and activation energy do not place it at the top of the pack. However, when subjected to pressure, structural changes accompanied by an α-to-β phase transition eliminates the ruffling and forms crossbraced, coplanar ribbons akin to those seen in **3-3c**·MeCN, giving rise to a significant decrease in activation energy E_{act}. Further compression of the β-phase to the γ-phase forces a crossover of the ribbons from the *b*-glides to the *n*-glides of the space group $Pbn2_1$. At the same time, neighbouring radicals in the ribbon-like arrays slide pass one another to allow a much more efficient packing at higher pressures than

the β-phase. Thus, while at ambient pressure, the α-phase does not perform as well as other RBBO radicals, formation of the β and γ-phase improves its transport properties significantly.

The larger question, is however, not the difference amongst the oxobenzene-bridged radicals **3-3**, but rather the common features which set them apart from other thiazyl radical conductors, notably the pyridine-bridged materials **3-2**. While packing differences (herringbone versus ribbon-like arrays) can be attributed to improvements in bandwidth, W, the notably lower cell potential, E_{cell}, of all oxobenzene-bridged radicals suggest they are electronically softer than the closely related pyridine-bridged radicals. This feature arises from the energetically favourable anionic states, attributed to the presence of a low-lying LUMO. Consequently, the higher electron affinity by virtue of the low-lying LUMO reduces the disproportionation enthalpy by 0.22 eV (in solution), and in the case of **3-3a**, is sufficient to permit the formation of a metallic state under mild pressures.

Pressure induced insulator-to-metal transitions have been reported previously in many organic materials. One particular example is the BEDT-TFF or ET salts, which possess the chemical formula $[ET]_2X$, where X is variations of $Cu(NCS)_2Cl$.[14] In these materials, the frontier π and π* orbitals from the bonding and antibonding combinations of the HOMO and LUMO of a neutral ET molecule are weakly separated. Due to the close proximity in energy of the frontier orbitals, removal of an electron forms the dication possessing open-shell states (Figure 3.16), opposed to a closed-shell singlet state, which lies much higher in energy. The ability of ET salts to accommodate an extra charge on each monomer permits a lower ionization potential (IP) and thus a lower ΔH_{disp} of 0.4 eV, responsible for the metallic state formed for these salts.

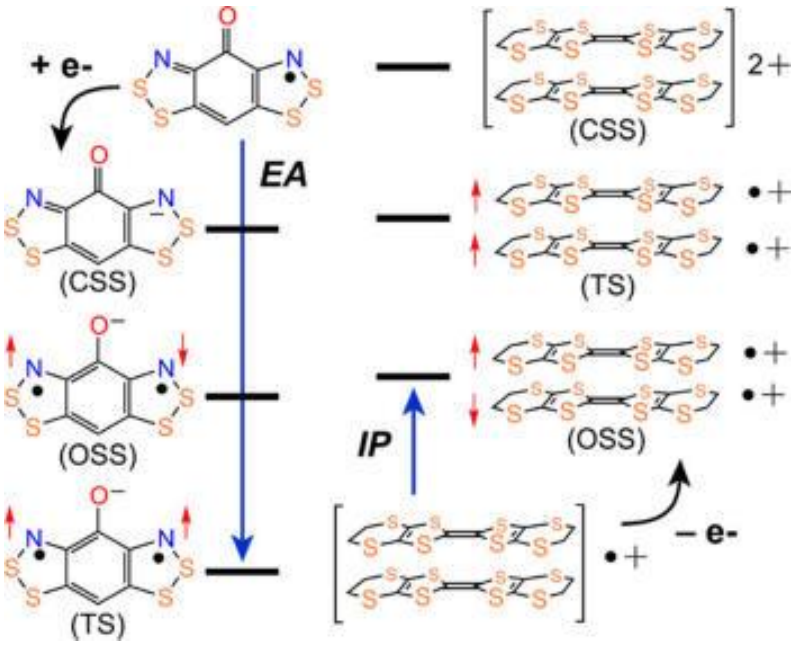

Figure 3.16 – Energetic ordering of closed shell and open shell states of **3-3a** and $[ET]_2^{\cdot+}$, where addition of an electron favours the triplet ground state for **3-3a** and removal of an electron favours the open-shell singlet. In both cases, the closed-shell singlet is higher in energy.

While the ET salts had the ability to lower the ionization potential to lower the disproportionation enthalpy, the oxobenzene-bridged radicals increase the electron affinity (EA) to decrease ΔH_{disp}. That is, an addition of an electron results in an increase in stability of the open-shell anionic states by virtue of the low-lying LUMO such that a triplet ground state is favoured. In that sense, its three structural changes and electronic structure provide many new areas to be explored. Further exploration of these oxobenzene-bridged radicals and related materials may be an interesting avenue for condensed matter physicists.

3.5 – Summary and Conclusion

The challenge of improving the bandwidth *W* to overcome the onsite Coulomb repulsion energy *U*, has proven almost an insurmountable task for a spin *f* = ½ system. While conventional methods for reducing *U* include the well-known strategy of traversing away from spin *f* = ½ systems, such as in spiro-biphenalenyls, as well as doping, the oxobenzene-bridged bisdithiazolyl radicals provide another method for decreasing *U*. The injection low-lying π-acceptor levels by the seemingly innocuous replacement of the N-R group in **3-2** with a carbonyl moiety opens the possibility of energetically favourable open-shell anodic

states and a consequently higher electron affinity. As a result, the oxobenzene-bridged radicals **3-3** are electronically softer and have a higher conductivity than the pyridine-bridged analogues **3-2.**

In theory, the prototypal radical **3-3a** represents a good building block for neutral radical conductors, but the hydrogen atom at the basal site forces the molecule to adopt ruffled ribbon-like arrays, offsetting the possibility of a two-dimensional electronic structure. However, the ruffled ribbons are highly susceptible to structural changes upon compression below 10 GPa, as seen with the additional two phase changes. The exact pressure of metallization is difficult to pinpoint, as different experiments suggest different values, but it is evident it occurs during the α-to-β transition near 4 GPa. Overall, the effects of pressure on the other derivatives (R = Cl, Ph) have yet to be explored, which may lead to new electronic structures. More importantly, the discovery of the low-lying π-acceptor LUMO allows new molecular systems to be designed where conductivity may be achieved without the use of physical pressure, which will be explored in Chapter 5.

3.6 - Experimental Section

Preparation of 2-methoxy-1,3-dinitrobenzene 3-9. 1,3-dinitrochlorobenzene (8.90 g, 43.92 mmol) was added to freshly prepared solution of $NaOCH_3$ (43.92 mmol of Na metal) in dry MeOH (100 ml) at room temperature with stirring. The mixture was gently refluxed for 3 hours, hot filtered to remove a white precipitate (*c.f.* NaCl), and the solvent removed *in vacuo* to afford a yellow solid. Recrystallization from MeOH afforded pale yellow needles (7.82 g, 39.48 mmol, 90% yield). ^{1}H NMR (δ, $CDCl_3$): 8.04 (d, 2H, Ar-H, *J* = 8.2 Hz), 7.36 (t, 1H, Ar-H, *J* = 8.2 Hz), 4.07 (s, 3H, -OCH_3).[15]

Preparation of 2-methoxybenzene-1,3-diamine 3-10. Stannous chloride dihydrate (10.82 g, 47.96 mmol) was added to a suspension of 2-methoxy-1,3-dinitrobenzene (9.30 g, 46.96 mmol) in a 100 mL of concentrated HCl. The mixture was cooled to 0 °C on an ice water bath and tin powder (14.20 g, 119.58 mmol) was added in small increments with vigorous stirring. The reaction was allowed to gradually warm to room temperature after one hour and the clear yellow solution was filtered through glass wool, washed with water, and concentrated *in vacuo* to 40 mL. HCl gas was passed through the solution for 2 minutes at 0-5 °C to give a white powder, which was collected by filtration, washed 2 x 20 mL conc. HCl and air dried. The product was recrystallized from 50:50 H_2O/HCl to give white needles. The bishydrochloride was dissolved in 250 mL of distilled water, freebased with sodium carbonate to pH 8-9. The mixture was extracted twice with 300 mL of DCM, dried and concentrated *in vacuo* to afford an orange-red oil, which solidified on standing. The product was recrystallized in toluene:hexane mixture to afford white needles (5.21 g, 37.75 mmol, 80% yield). mp: 54-56 °C; ^{1}H NMR (δ, $CDCl_3$): 6.70 (t, 1H, Ar-H, *J* = 7.9 Hz), 6.16 (d, 2H, Ar-H, *J* = 7.9 Hz), 3.79 (s, 3H, -OCH_3).

Preparation of 2,6-diaminoanisole-3,5-dithiocyanuric ester 3-11. 2,6-Diaminoanisole **3-10** (2.50 g, 18.1 mmol) and ammonium thiocyanate (11.0 g, 14.4 mol) was dissolved in 150 mL MeOH at 0 °C. A solution of Br_2 (3.75 mL, 14.6 mmol) in 20 mL MeOH was added dropwise over 30 min to give a cream colored precipitate. The mixture was stirred at 0 °C for one h, then poured onto 100 mL crushed ice and the cream colored precipitate was collected by filtration. Recrystallization from EtOH afforded lustrous cream needles of **3-11**. (3.20 g, 1.28 mmol, 70% yield). mp: 153-156 °C; IR: 3475 (w), 3429 (w), 3374 (w), 3322 (w), 2358 (w), 2151 (w), 1608 (m), 1235 (w), 992 (w), 721 (w) cm^{-1}. ^{1}H NMR (δ, C_6D_6): 6.72 (s, 1H, Ar-H), 3.89 (s, 2H, NH_2), 2.91 (s, 3H, -OCH_3). Anal. Calcd for $C_9H_8N_4OS_2$: C, 42.84; H, 3.20; N, 22.21. Found: C, 42.73; H, 3.34; N, 22.07.

Preparation of 2,6-diamino-3,5-dithioanisole 3-12. 2,6-Diaminoanisole-3,5-dithiocyanuric ester **3-11** (2.13 g, 8.43 mmol) and sodium sulfide nonahydrate (8.11 g, 33.8 mmol) were dissolved in 250 mL of degassed water and warmed to 60 °C under a flow of nitrogen. The mixture was hot filtered, cooled on an

ice-water bath and acetic acid was added dropwise to pH ~ 6 to give a yellow precipitate which was filtered off, dried in vacuo and used in subsequent steps without further purification (1.51 g 7.44 mmol, 89% yield). IR: 3401 (w), 2724 (w), 2508 (w), 1602 (m), 1217 (m), 1152 (w), 1030 (m), 872 (w), 722 (w) cm^{-1}. ^{1}H NMR (δ, C_6D_6): 7.49 (s, 1H, Ar-H), 4.01 (s, 2H, NH_2), 3.34 (s, 3H, -OCH_3), 2.49 (s, 1H, SH).

Preparation of 3-13. 2,6-Diamino-3,5-dithioanisole **3-12** (2.04 g, 10.1 mmol) was dissolved in 100 mL freshly distilled MeCN. Thionyl chloride (6.45 g, 54.2 mmol) was added dropwise to the yellow solution, which was heated a gentle reflux for 2 h. The dark purple precipitate was collected by filtration, washed with 20 mL MeCN, then refluxed with 20 mL of DCE, hot filtered and washed 2 × 20 mL DCM to give crude [**3-3a**][Cl] as a purple-black powder (2.60 g , 9.26 mmol, 92% yield). IR: 1657 (m), 1320 (s), 1046 (w), 1021 (w), 769 (w), 747 (w) cm^{-1}.

Preparation of 3-14. Crude [**3-3a**][Cl] (2.60 g, 9.26 mmol) was added to solution of silver nonafluorobutanesulfonate, AgONf (3.76 g, 9.23 mmol) in 100 mL of freshly distilled MeCN, and the mixture heated under gentle reflux for 30 min. The mixture was hot filtered and the solvent flashed distilled to leave a deep red solid. This solid was triturated with CH_2Cl_2:AcOH (10:1) and the dark purple precipitate so formed collected by filtration (3.09 g, 5.68 mmol, 61% yield). Subsequent recrystallization of this material from MeCN and EtCN afforded lustrous dark green shards of analytically pure [**3-3a**][ONf] (1.54 g , 2.83 mmol, 50% yield). mp: > 250 °C. IR: 1485 (s), 1467 (s), 1396 (m), 1327 (s), 1274 (s), 1223 (s), 1135 (s), 1058 (s), 766 (s), 657 (m) cm^{-1}. UV-vis: λmax 554 nm, ε = 1.5 × 104 L mol^{-1} cm^{-1}. Anal. Calcd for $C_{10}HF_9N_2O_4S_4$: C, 22.06; H, 0.19; N, 5.45. Found: C, 22.21; H, 0; N, 5.45.

Preparation of 3-3a Radical for conductivity and magnetic measurements. *Method I.* A solution of [**3-3a**][ONf] (450 mg, 0.827 mmol) in 120 mL of degassed (three freeze-pump-thaw cycles) MeCN was filtered into a stirred solution of OMFc (320 mg, 1.07 mmol) in 50 mL of similarly degassed MeCN, yielding a dark purple solution over a dark purple microcrystalline solid. After 1 h the product was filtered off, washed with 3 × 20 ml of dry MeCN, and dried in vacuo (0.200 g, 0.815 mmol, 99%). IR: 3401 (w), 2724 (w), 2508 (w), 1602 (s), 1217 (m), 1152 (w), 1100 (w), 1030 (m), 938 (w), 872 (w),722 (w) cm^{-1}. Anal. Calcd for $C_6HN_2OS_4$: C, 29.37; H, 0.41; N, 11.42. Found: C, 29.30; H, 0.61; N, 11.25.

Method 2. Slow Diffusion for Single Crystals. A solution of [**3-3a**][ONf] (54 mg, 0.99 mmol) in 13 mL degassed (4 freeze-pump-thaw cycles) MeCN was allowed to diffuse slowly into a similarly degassed solution of OMFc (60 mg, 2.01 mmol) over a 6 h period, affording **3-3a** as very fine, hairlike needles.

Chapter 4

Pyridone Chemistry

4.1 – Introduction

In previous chapters, the synthesis and characterization of various oxobenzene-bridged radicals **4-1** was presented. These radicals are appealing systems as they exhibit an intrinsically low barrier to charge transport, *U*, as a result of a low-lying π-LUMO. While the value of *U* is not expected to change significantly by altering the basal substituent, the solid-state packing can be modified accordingly to increase the electronic bandwidth *W*. As we have seen with the fluoro- and proto-oxobenzene-bridged radical (**4-1a, 4-1b**, R = F, H), compression under mild pressures generated significant bandwidth to overcome the barrier to charge transport *U* and afford a metallic state.[1]

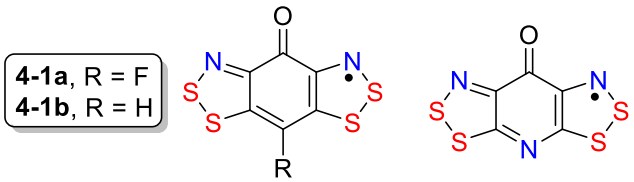

4-1 **4-2**

In pursuit of new derivatives with potentially improved solid-state packing, we have considered the possibility of incorporating a pyridine (or pyridine-quinone) core in place of the oxobenzene-bridge found in **4-1**. This would afford the framework of a pyridone-bisdithiazolyl radical **4-2**. The idea behind this project was discussed in Chapter 2, where it was shown that an endocyclic nitrogen can be used as a structure maker to interlace the molecular ribbons by S---N supramolecular contacts. In addition, its small nature holds potential for a much more tightly bound structure, hence increasing the electronic bandwidth *W*. The first attempts to synthesize **4-2** followed conventional synthetic procedures established for the other oxobenzene-bridged radicals. The proposed synthesis is shown in Scheme 4.1. However, many challenges were encountered in the initial stages of the synthesis arising from the peculiar chemistry afforded by the pyridine system. While significant progress has been made to synthesize **4-2**, the radical was never attained. However, a variety of new novel species were produced, which will be highlighted in this chapter.

Scheme 4.1 - Proposed Synthetic Scheme

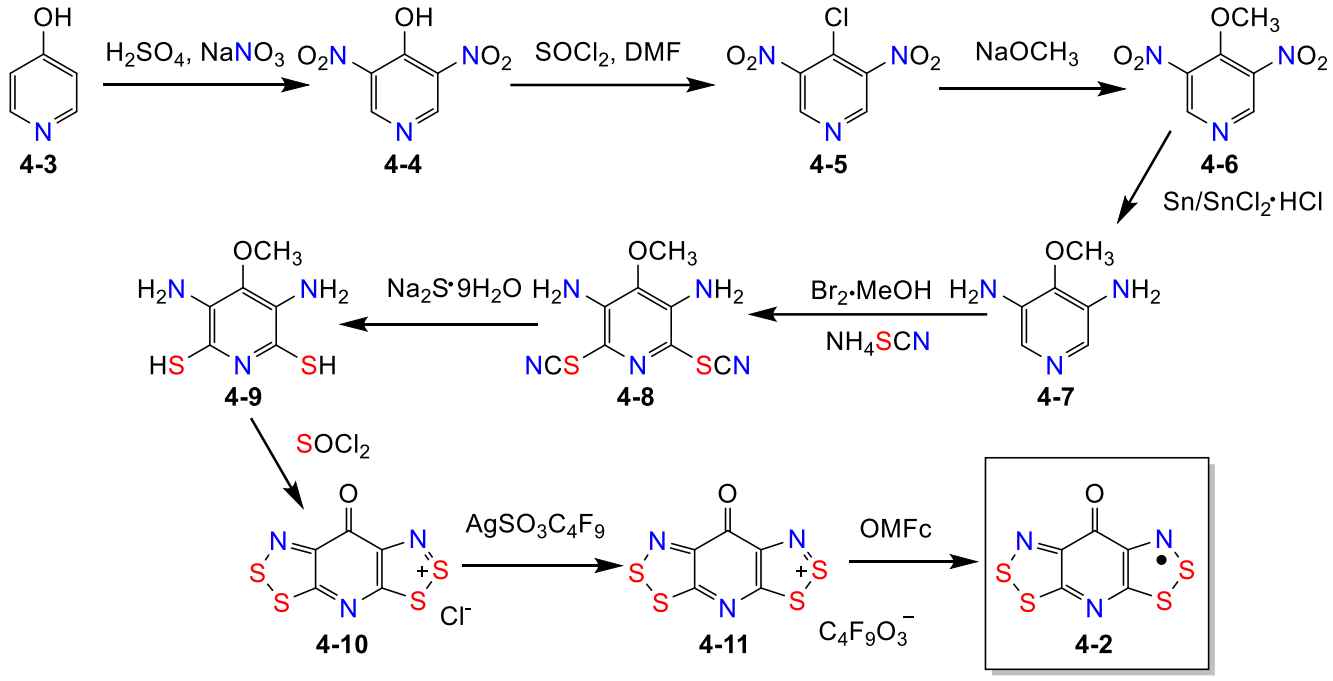

4.2 Synthesis

4.2.1 Conventional Synthetic Procedure

Following the conventional synthetic procedure developed for the other oxobenzene-bridged radicals, the first step involved the nitration of commercially available 4-hydroxylpyridine **4-3**. While literature procedures indicate the need for fuming nitric acid with concentrated sulfuric acid,[2] the nitration can be performed under milder conditions with sulfuric acid and sodium nitrate heated at 100 °C for 16 hours. After the allotted reaction time, the solution was poured onto ice to afford a yellow precipitate of 3,5-dinitro-4-hydroxylpyridine **4-4**, which was used without further purification in subsequent steps. The resulting filtrate can be neutralized with ammonium hydroxide to yield 3-nitro-4-hydroxylpyridine **4-13**. A shorter reaction time (3 hours) can also be used to synthesize **4-13** cleanly (scheme 4.4).

Chlorination of **4-4** with various chlorination reagents such as thionyl chloride (in dry toluene/heptane), phosphoryl chloride and phosphorus pentachloride afforded a mixture of 4-chloro-3,5-dinitropyridine **4-5** and **4-4** at best (scheme 4.2). The difficulty in chlorination can be attributed to the tautomerism exhibited by **4-4** with **4-4b**, in which the keto-tautomer predominates in equilibrium. Many literature procedures[3] also claim **4-5** as an unstable intermediate, in which isolation resulted in significant hydrolysis back to 3,5-dinitropyridone **4-4b**, and thus was used immediately without isolation. To this end,

4-5 was generated using thionyl chloride, and then immediately treated with a dried solution of sodium methoxide. Unfortunately, a brown oil was obtained which could not be recrystallized.

Scheme 4.2

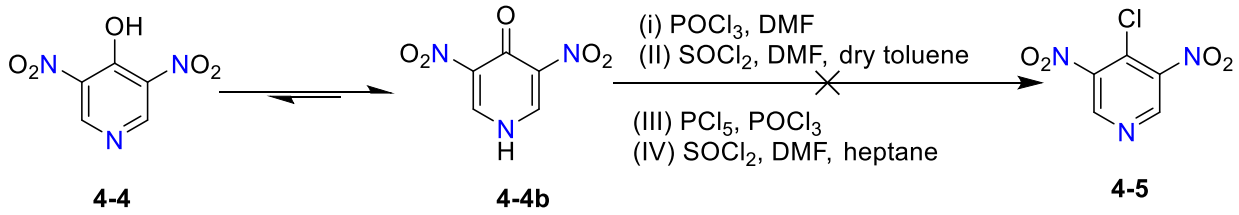

Interestingly, successful chlorination and isolation of **4-5** was finally obtained using thionyl chloride (neat) and DMF, heated at reflux for 48 hours (Scheme 4.3).[3] Although 3,5-dinitropyridone **4-4b** is not overly soluble in thionyl chloride at room temperature, elevation of the temperature to reflux afforded a homogenous yellow solution. After the allotted reaction time, excess thionyl chloride was removed *in vacuo* to afford a yellow powder, which was used without further purification.

Scheme 4.3

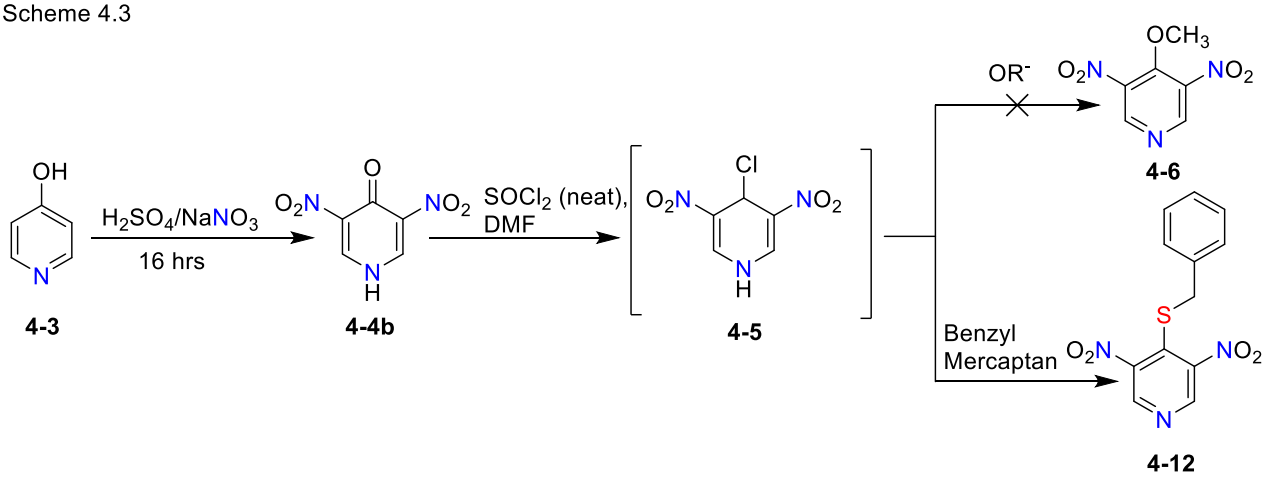

Once we were satisfied with the isolation of **4-5**, the next step involved its nucleophilic substitution with sodium methoxide solution in dichloroethane. It has been reported that 3,5-dinitro-4-methoxypyridine **4-6** is also unstable, decomposing upon standing.[4] Nevertheless, the reaction was carried out and precipitation of a white powder was observed after 30 minutes with gentle heating. This material was later isolated and identified as 2,6-dinitropyridone **4-4b**. Identical results were observed using dried butanol. Uncertain if the solvent (dichloroethane) was the source of hydrolysis, benzyl mercaptan was added to **4-5** in dichloroethane. To our surprise, a bright yellow solid was isolated as **4-12** in good yields.

Scheme 4.4

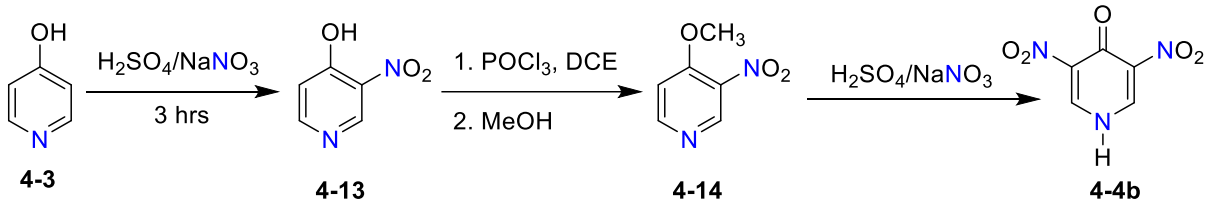

4-3 **4-13** **4-14** **4-4b**

While we were unable to incorporate a methoxy-substituent into 4-chloro-3,5-dinitropyridone **4-5** from 3,5-dinitropyridone **4-4b**, it can easily be obtained with phosphoryl chloride and methanol from 3-nitro-4-phenolpyridine **4-13** affording a white powder (Scheme 4.4).[5] However, strong acidic conditions during nitration with sulfuric acid and sodium nitrate results in cleavage of the methoxy-substituent, reverting back to 3,5-dinitropyridone **4-4b**.

With little success in obtaining 3,5-dinitro-4-methoxypyridine **4-6**, we attempted simply to reduce the dinitro groups of **4-4b** (scheme 4.5) using iron and hydrochloric acid. However, attempts to isolate the free base using sodium carbonate resulted in rapid decomposition of the free-base product. Remarkably, reduction with tin(II)dichloride in concentrated hydrochloric acid heated at 110 °C, followed by treatment with sodium carbonate, gave rise to a stable free base as a result of chlorination at the 2 and 6-positions.

Scheme 4.5

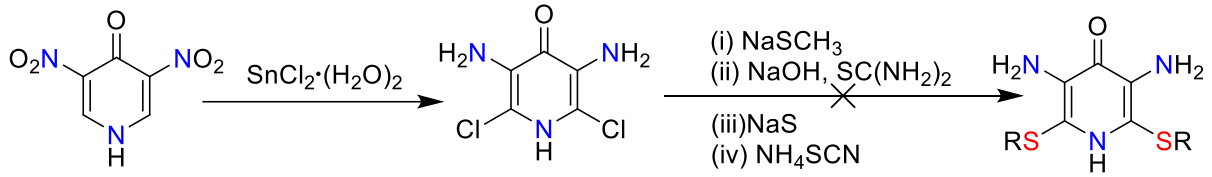

4-4b **4-15** **4-16**

The next challenge involves replacement of the chlorine atoms with a sulfur to form a dithiol **4-16**. Many thiolating reagents have been tried, but many were either unreactive or produced a material which were insoluble and cannot be fully characterized. Unable to synthesize a framework suitable for closure, our focus turned towards another route.

4.2.2 - N-oxide Route

As seen from the previous section, the challenge in synthesizing 3,5-dinitro-4-methoxypyridine **4-6** and 3,5-dinitro-2,6-dithiolpyridone **4-16** eventually led to an alternate route to obtain a suitable framework for closure. The proposed synthetic scheme is illustrated below (scheme 4.6). Although the

chemistry described in this section utilizes the dibromo-derivative, similar chemistry can be and has been done with the dichloro-variant.

Scheme 4.6

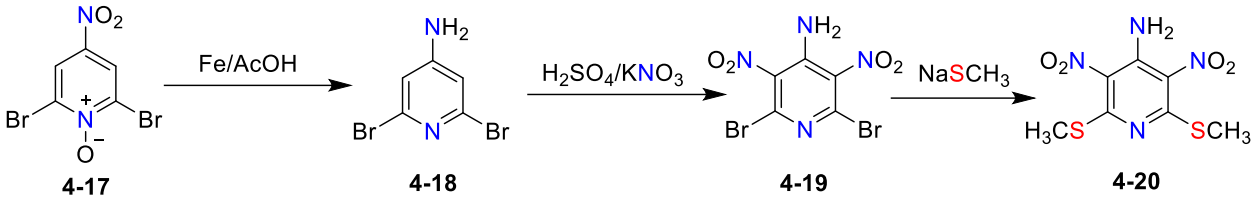

4-17 **4-18** **4-19** **4-20**

4-Nitro-2,6-dibromo-N-oxide **4-17** can be easily synthesized according to literature procedures.[6] Subsequent addition of iron and acetic acid resulted in the reduction of both the nitro and N-oxide to give 4-amino-2-6-dibromopyridine **4-18**, a much more efficient method than described in other literature procedures.[7] Subsequently, **4-18** could be nitrated using potassium nitrate in minimal amount of concentrated sulfuric acid, to afford a yellow precipitate **4-19** in good yields.[8] The next step involved incorporating sulfurs to the 2 and 6-positions, which can be easily accomplished using sodium thiomethoxide solution, yielding **4-20** as a yellow powder. However, diazotization with nitrous acid (generated in situ by sodium nitrite and *p*-sulfonic acid) resulted in predominately starting material **4-20**, an effect which may be accounted for by deactivation of the aromatic ring by the nitro substituents[9] as well as the significant decrease in solubility (scheme 4.7).

Scheme 4.7

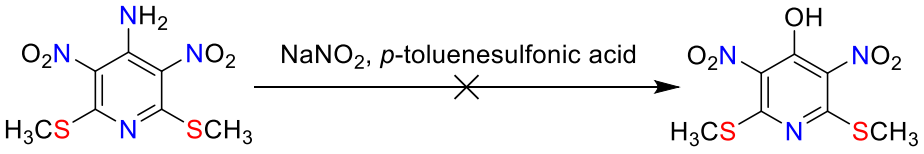

4-20 **4-21**

Consequently, diazotization was attempted on a non-nitrated complex, **4-18**, with *p*-toluene-sulfonic acid (*p*-TSA) and 3 mL of H_2O (Scheme 4.8). The slurry was stirred until homogenous before sodium nitrite was added to afford an immediate yellow precipitate. The reaction was stirred at room temperature for 2.5 hours before the solid was filtered, washed with H_2O and dried in air. The isolated product was recrystallized in MeOH, and mass spectroscopy of the obtained product indicated the formation of **4-22**.

Scheme 4.8

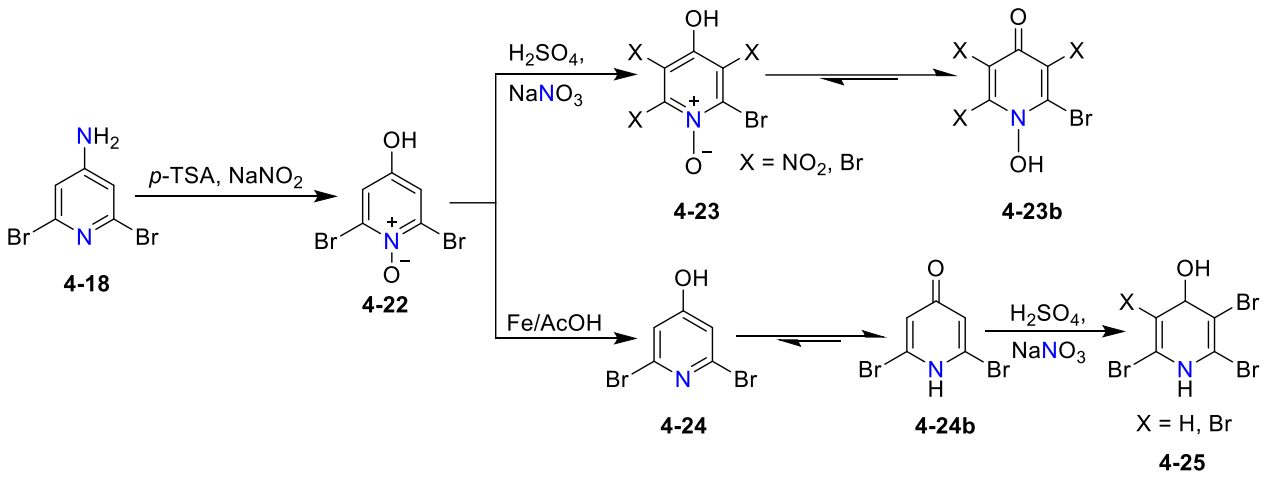

However, nitration of the N-oxide **4-22** with sodium nitrate and sulfuric acid resulted in a mixture of di-, tri-, and tetrabromopyridine **4-23**. In efforts to control the nitration, the N-oxide **4-22** was reduced with iron powder and acetic acid. The solution was stirred at room temperature for 2 hours, then concentrated *in vacuo* before being poured onto 300 mL of water, to afford a white powder of **4-24**. Unfortunately, successful nitration with sulfuric acid and sodium nitrate was never achieved, which can be attributed to the tautomerism between **4-24** and **4-24b**. Instead, the tautomers **4-24** and **4-24b**, react to form only mixtures of tri- and tetrabromo-4-hydroxylpyridine **4-25** (*m/z* = 411, 373).

While in the first case with **4-20** (Scheme 4.7), we were unable to successfully diazotize with nitro groups at the 3 and 5-position, the latter case with **4-18** indicated successful diazotization (Scheme 4.8), but nitro groups on the 3- and 5-positions could not be prepared. Consequently, another route to obtain the framework akin to **4-21** must be developed.

4.3 – Conclusion

The challenge associated with pyridone chemistry has led us to explore a variety of different synthetic routes to obtain a suitable framework for closure. While we were unable to obtain the desired framework, many new molecules were synthesized and characterized. Moreover, we have developed improved synthetic methods for obtaining 3,5-dinitropyridone **4-4b** and 2,6-dibromo-4-hydroxylpyridine **4-24** by a simple diazotization.

4.4 – Experimental Section

Preparation of 3,5-dinitropyridin-4-ol 4-4b. Sodium nitrate (28.0 g, 329.45 mmol) was added to a suspension of 4-hydroxylpyridine in sulfuric acid (60 mL) at 0 °C periodically. The reaction was heated to 100 °C for 16 hours, cooled to RT, then poured onto 400 mL of ice water, affording a yellow precipitate (5.11 g, 36.47 mmol, 67%). The obtained product was use without any further purification. ^{1}H NMR (δ, DMSO): 8.88 (s, 2H, Ar-H). IR: 1639 (s), 1607 (s), 1539 (s), 1242 (w), 1156 (s), 1021 (w), 969 (w), 840 (m), 771 (s), 722 (w), 663 (w), 559 (m), 516 (m) cm^{-1}.

Preparation of 4-chloro-3,5-dinitropyridine 4-5. 2 drops of DMF was added to a suspension of **4-4b** (5.0 g, 27.01 mmol) in thionyl chloride (10 mL, 137.85 mmol) and heated at reflux for 48 hours. After the alotted reaction time, the yellow solution was cooled to RT and excess thionyl chloride removed, affording a yellow oil which solidified upon standing. This material readily undergoes hydrolysis and must stored in cold conditions. ^{1}H NMR (δ, $CDCl_3$): 9.20 (s, 2H, Ar-H).

Preparation of 4-(benzylthio)-3,5-dinitropyridine 4-12. Benzyl mercaptan (2.5 mL, 21.34 mmol) was added to a solution of 4-chloro-3,5-dinitropyridine **4-5** in dichloroethane (25 mL), affording an immediate yellow precipitate. The reaction was stirred at RT for 2 hours, the yellow solid filtered off, washed with DCE and dried in air (2.408 g, 8.24 mmol, 56% yield). ^{1}H NMR (δ, $CDCl_3$): 9.10 (s, 2H, Ar-H), 7.33 (m, 5H, Ar-H), 3.82 (s, 2H, Bn-H).

Preparation of 3,5-diamino-2,6-dichloropyridin-4(1H)-one 4-15. Tin(II) chloride dihydrate (19.5 g, 86.41 mmol) was added to a solution of **4-4b** (4.0 g, 21.61 mmol) and concentrated hydrochloric acid (150 mL). The solution was heated to 110 °C and another equivlent of tin(II) chloride dihydrate (19.5 g, 86.41 mmol) was added. The reaction was stirred until cooled to RT, in which a fine grey powder was isolated. The fine grey powder was dissolved in H_2O (10 mL), and precipitated out with HCl (30 mL) to afford silver flakes (2.5 g, 9.44 mmol, 43% yield). IR: 3489 (m), 3434 (m), 3391 (m), 3356 (m), 1602 (w), 1551 (m), 1551 (w), 1308 (w), 1242 (s), 1147 (w), 1103 (w), 1061 (w), 927 (w), 755 (m) 722 (m) cm^{-1}.

Preparation of 2,6-methylthio-3,5-dinitropyridin-4-amine 4-20. Sodium thiomethoxide solution (4.00 mL, 11.986 mmol) was pipetted into a solution of 4-amino-3,5-dinitro-2,6-dibromopyridine (1.00 g, 2.92 mmol) and acetone (20 mL) to afford a red solution. The reaction was stirred at rt for 2 hours then poured onto ice to afford a yellow precipitate (0.614 g, 2.22 mmol, 76% yield). ^{1}H NMR (δ, DMSO): 9.33 (s, 2H, NH_2), 2.54 (s, 3H, SCH_3). IR: 3400 (w), 3293 (w), 1620 (m), 1581 (m), 1553 (m), 1330 (w), 1228 (s), 1122 (w), 1002 (s), 935 (m), 779 (m), 617 (m) cm^{-1}.

Preparation of 2,6-dibromo-4-hydroxypyridine 1-oxide 4-22. Sodium nitrite (1.70 g, 24.64 mmol) was added to a solution of 4-amino-2,6-dibromopyridine (2.0 g, 7.94 mmol) and *p*-toluenesulfonic acid

(9.0 g, 47.31 mmol) in 3 mL of H_2O affording an immediate yellow precipitate. The reaction was stirred for 2.5 hours before the precipitate was filtered, washed with H_2O and air dried. The obtained product was hydrolyzed in methanol (50 mL), concentrated to 20 mL and precipitated with H_2O (20 mL) (1.08 g, 4.016 mmol, 51% yield). *m/z* = 359; ^{1}H NMR (δ, DMSO): 7.70 (s, 2H, Ar-H). IR: 1553 (m), 1203 (m), 1147 (m), 1123 (w), 1036 (m), 1011 (w), 970 (w), 818 (w), 722 (w), 567 (m) cm^{-1}.

Preparation of 4-hydroxy-2,6-dibromopyridine 4-24. Iron powder (1.66 g, 29.74 mmol) was added in small aliquots to a solution of 4-hydroxylpyridine N-Oxide (4.060 g, 15.09 mmol) and acetic acid (100 mL). The yellow solution was stirred at RT for 2 hours, filtered, and concentrated in vacuo to 50 mL, then poured into 300 mL of H_2O. The white solid was collected by filtration and air dried (3.095 g, 12.23 mmol, 81% yield). *m/z* = 253; ^{1}H NMR (δ, $CDCl_3$): 8.16 (s, 2H, Ar-H). IR: 3105 (w), 1542 (s), 1346 (s), 1170 (w), 1158 (w), 1143 (m), 983 (w), 884 (m), 769 (m) 732 (m) cm^{-1}.

Chapter 5

Designing Multiple Band Systems

5.1 – Introduction

The need for partial charge transfer in charge transfer salts to achieve metallic conductivity, by avoiding a half-filled band (f = ½) electronic structure, was well established in the 1970s.[1] However, by their very nature, conventional neutral radical materials are based on a ½-filled energy band, and the Coulomb repulsion energy U is large in comparison to the electronic bandwidth, W. As a result Mott insulating states prevail. Typically, systems such as the pyridine-bridged bisdithiazolyl radicals **5-1**[2] can be described by the single band Hubbard model (Figure 5.1a) in the strong correlation limit. Curiously, many high T_c-superconductors also adopt a nominally ½-filled band structure, in which the Coulomb repulsion energy is small ($U > W$). These systems can be modelled to a multiple band system in which migration of an electron to an adjacent low-lying vacant orbital is energetically more favorable than transfer to a neighboring SOMO. As described in previous chapters, the oxobenzene-bridged bisdithiazolyl radicals **5-2**[3] can also be modelled to the multiple band system (Figure 5.1b), as a result of a low-lying LUMO originating from the carbonyl moiety. This increases the electron affinity of the radical, and also allows the possibility of energetically favorable open-shell anionic states.

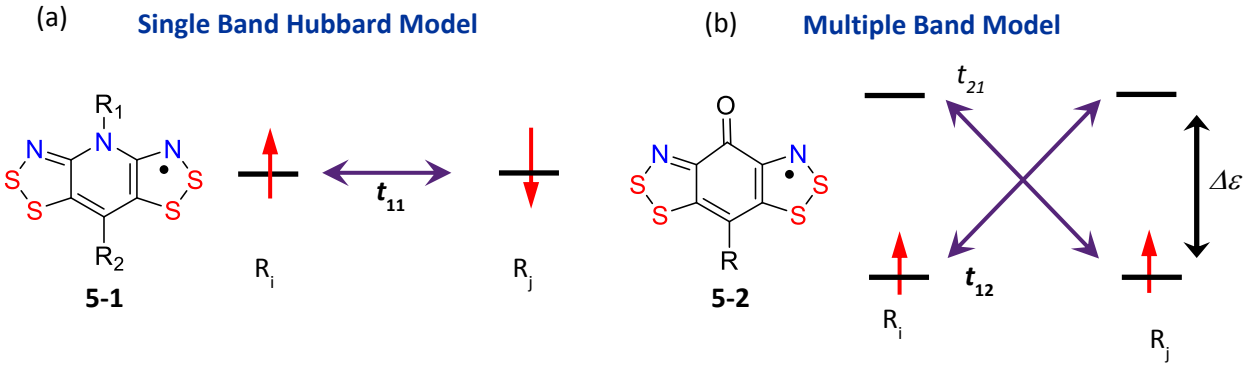

Figure 5.1 – (a) Single-band model exhibited by many pyridine-bridged bisdithiazolyl radicals and (b) multiple band model exhibited by the oxobenzene-bridged radical as a result of the low-lying LUMO from the carbonyl moiety.

Chart 5.1

5-2a, R = F
5-2b, R = Cl
5-2c, R = Br
5-2d, R = I
5-2e, R = H

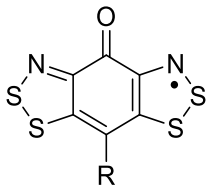

5-2

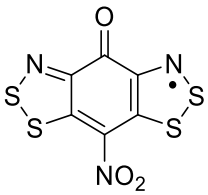

5-3

In order to identify other potential multiple band radicals, density functional theory (DFT) calculations were performed on various model oxobenzene-bridged (RBBO) radicals at the (U)B3LYP/6-311(d,p) level (Figure 5.2). As we recall from Chapter 1, the disproportionation enthalpy ΔH_{disp} can be approximated by the difference between the ionization potential (*IP*) and electron affinity (*EA*), such that $\Delta H_{disp} \sim U \sim IP - EA$. Total electronic energies of closed-shell singlet (CSS) and open-shell triplet states (TS) were computed using the PCM model with acetonitrile as the solvent, and the results are shown in Figure 5.2. Of particular note is the fact that the calculated disproportionation enthalpy for existing RBBO radicals **5-2a-e** range between 0.80 – 0.95 eV, however, incorporation of a π-acceptor such as NO_2 at the basal site **5-3** affords a *U* of near 0.70 eV, a significant decrease compared to the other RBBO radicals. This value drops even further, to near 0.40 eV, when E = $C(CN)_2$.

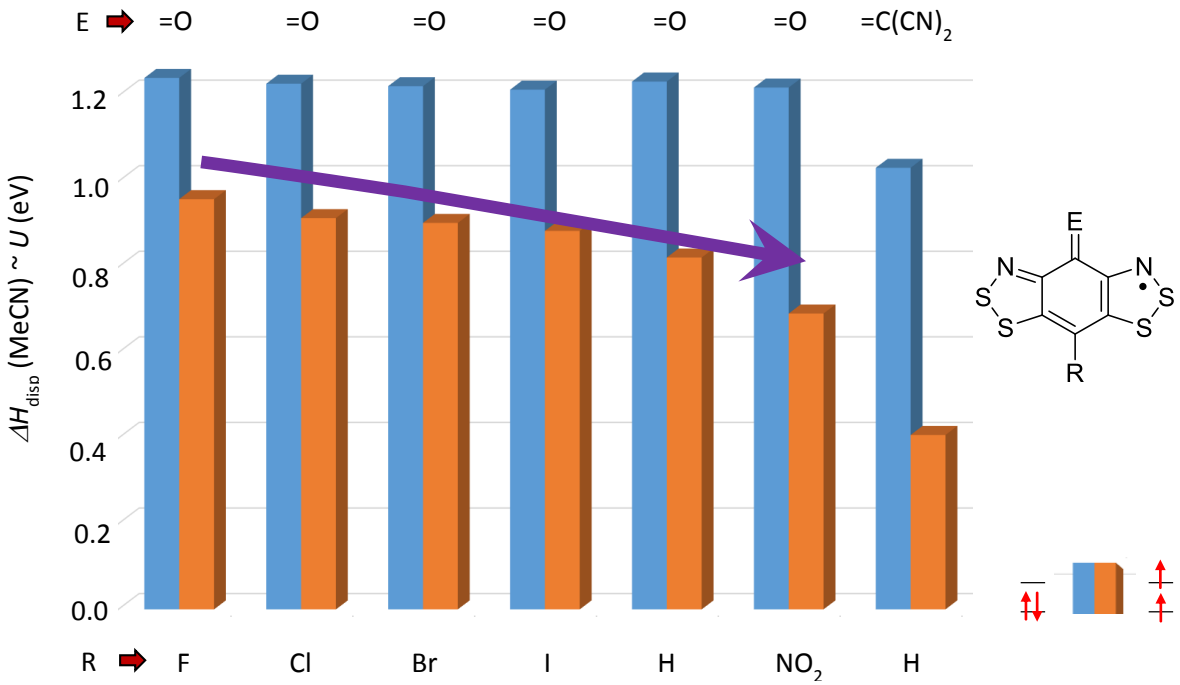

Figure 5.2 – (U)B3LYP/6-311G(d,p)/PCM calculated disproportionation energies ΔH_{disp} (= *IP* – *EA*), with MeCN as solvent, for model oxobenzene-bridged radicals **5-2**. Blue represents ΔH_{disp} values derived using a closed-shell singlet state for the anion, while orange represents the valued derived from the anion with a triplet state.

The focus of this chapter will be on the preparation and characterization of the nitro-oxobenzene-bridged radical **5-3**. While this work is still ongoing, preliminary results including the synthesis, crystallography, and magnetic and conductive properties will be presented.

5.2 – Results

5.2.1 – Building Block Synthesis

Unlike the other oxobenzene-bridged radicals, the nitro-oxobenzene-bridged bisdiathiazolyl radical **5-3** is synthesized *via* an approach (scheme 5.1) involving selective, stepwise reduction of picric acid **5-4** with ammonium sulfide to form an ammonium salt. While literature procedures suggested the use of hydrogen sulfide in aqueous ammonia to give **5-6** directly,[4] we were only able to attain an ammonium salt. The salt was subsequently dissolved in water and protonated with acetic acid and isolated as the mono-amine **5-5** as dark red needles. Initial attempts to reduce the second nitro-substituent with tin(II) chloride resulted in reduction of both nitro groups in **5-5**. Selective reduction of the other nitro-substituent was achieved following a German patent using L-ascorbic acid and a catalytic amount of $FeSO_4 \cdot 7H_2O$.[5] However, the reaction must be done in sodium hydroxide solution (rather than the cited ammonium hydroxide solution) to give the corresponding 2,6-diaminophenol, which was recrystallized in water to afford fine brown hairs **5-6**. Condensation with sulfur monocloride afforded an insoluble chloride salt **5-7**, which was converted to a more soluble triflate with silver trifluoromethanesulfonate.

Scheme 5.1

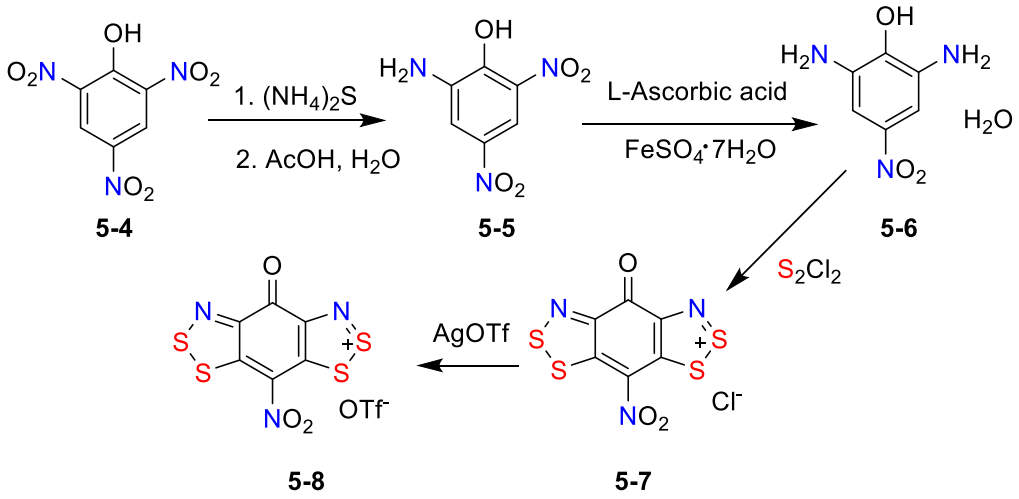

5.2.2 – Electrochemistry

To determine a suitable reducing agent, the electrochemical behaviour of the triflate salt **5-8** was explored using cyclic voltammetry (CV), starting with a solution of **5-8** in MeCN with 0.1 M *n*-Bu_4NPF_6 as a supporting electrolyte and Pt wire electrodes. As can be seen from Table 5.1, variations in the halogens (R = Br, Cl, F, H) have systematic effect on the E_{cell} potentials; fluorine, the strongest π-donor, affords the largest E_{cell} value (0.69 V), while the proto-derivative displays a much smaller E_{cell} value of 0.56 V. Incorporation of a π-acceptor, such as NO_2, in **5-3** further decreases the E_{cell} potential to 0.45 V, the lowest ever observed for a neutral radical.

Table 5.1 – Electrochemical potentials[a] for selected oxobenzene-bridged radicals **5-2.**

R	E_{pc}(-1/0)[b]	$E_{½}$(0/+1)[b]	E_{cell}[c]
Ph	-0.529	0.108 (0.071)[d]	0.60
Br	-0.481	0.191(0.158)[d]	0.64
Cl	-0.481	0.195 (0.158)[d]	0.64
F	-0.479	0.208(0.241)[d]	0.69
H	-0.525	0.061(0.035)[d]	0.56
NO_2	-0.249(-0.215)[e]	0.233(0.197)[d]	0.45

[a]In volts, measured in MeCN. [b]Referenced to SCE, all irreversible except for R = NO_2. [c]E_{cell} estimated as E_{pc}(0/+1) – E_{pc}(-1/0). [d]$E_{½}$; E_{Pc} is given in parenthesis. [e]reversible, $E_{½}$ (-1/0) given in parenthesis.

In all oxobenzene-bridged radicals the first reduction wave, corresponding to the 0/+1 couple, is reversible. However, the second reduction, corresponding to the -1/0 couple, is strongly irreversible for many of these RBBO radicals. This can be attributed to the comproportionation of the electrochemically produced anion in a large excess of cation, frequently observed in the electrochemistry of monocyclic dithiazolylium cations[6] and related materials.[7] In the case of **5-3**, both processes are reversible, which suggest the increase in stability of the anion by the nitro-substituent.

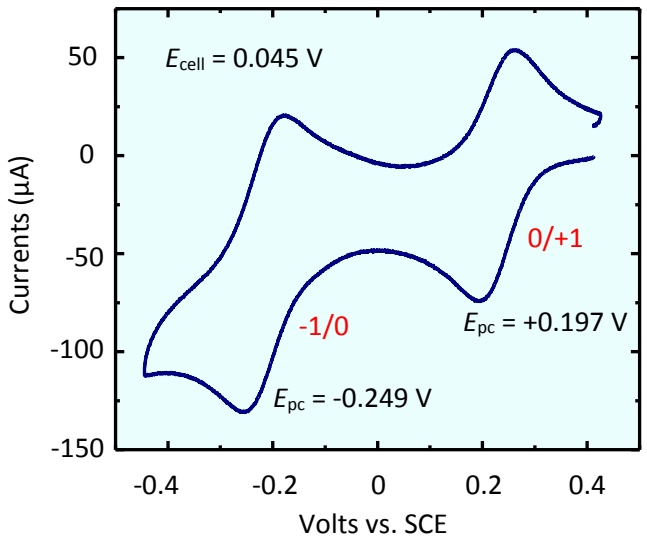

Figure 5.3 – Cyclic voltammetry (CV) scan of **5-8** in MeCN with Pt electrodes, 0.1 M n-Bu_4NPF_6 electrolyte, scan rate 100 mV s^{-1}.

5.2.3 – Isolation of Radicals

Based on the half-wave potential from the electrochemistry experiments, octamethylferrocene (OMFc) was selected as the reducing agent [$E_{½}$(ox) = -0.038 V vs SCE][8] to afford the respective radical **5-3**. This afforded lustrous black needles by slow co-diffusion of MeCN solutions of OMFc and **5-8** using H-cell methods. Although preliminary FTIR experiments revealed the absence of any solvate bands near 2200 cm^{-1}, single X-ray crystallography revealed the formation of an acetonitrile solvate, discussed in section 5.2.5**.** Satisfied with the isolation of [**5-3**]·MeCN, focus turned towards obtaining the non-solvated radical. To this end, many solvents were considered, but we eventually settled with propionitrile (EtCN), which, to our surprise, also formed a solvate with a completely different structure. Next, we tried methyl ethyl ketone (MEK), in which preliminary powder analysis reveals yet another structure. Further work on the MEK phase is currently being pursued.

We also explored the use of milder reducing agents such as dimethylferrocene (DiMFc), whose potential (0.264 V vs SCE)[9] appears to be insufficient to reduce the cation **5-8** to the radical **5-3**. However, in practice, with the aid of lattice energies, crystals can be formed as in the case with [**5-2c**]·MeCN (R = Cl).[3b] Crystals grown in this fashion afforded small black diamonds; these hold the potential to be yet another phase. Single x-ray crystallography for crystals obtained from reductions performed with OMFc

in MEK and DiMFc in MeCN are currently being investigated. Currently, there are at least 3 phases, [**5-3**]·MeCN, [**5-3**]·$(EtCN)_{0.25}$, and the crystals obtained from DiMFc, however, transport property measurements have focused principally on [**5-3**]·MeCN. The results will be presented in the following sections.

5.2.4 – EPR Spectra

The spin distribution of **5-3** has been probed by electron paramagnetic (EPR) spectroscopy. The EPR spectra of **5-3** in toluene displays the conventional 5-line pattern nominal for radicals of this type arising from coupling between the two equivalent ^{14}N nuclei (a_N = 3.306) with small hyperfine coupling to the basal nitrogen of the nitro-substituent (a_N = 0.323). As expected, the a_N values are approximately one-half those found in monofunctional-DTDA discussed in Chapter 2.

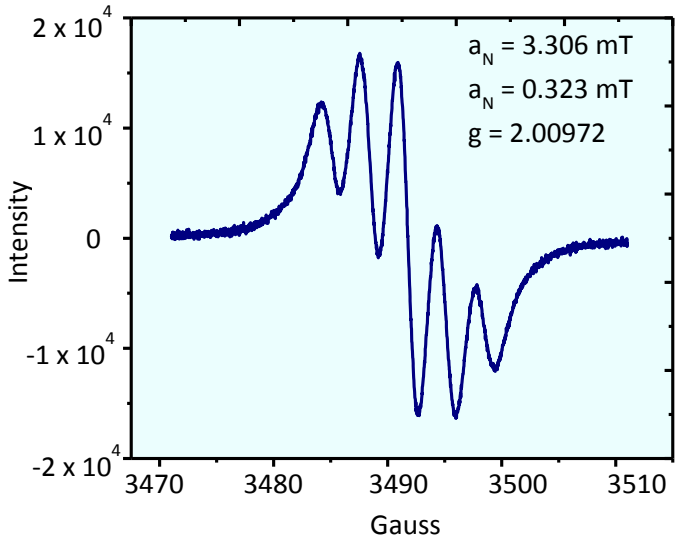

Figure 5.4 - Electron paramagnetic resonance of **5-3** in toluene; hyperfine coupling constants in mT are shown.

5.2.5 – Crystallography & Magnetic Properties of [5-3]·MeCN

X-ray diffraction analysis on single crystals of **5-3** reduced with OMFc in acetonitrile revealed the structure crystallizes as an acetonitrile solvate, belonging to the monoclinic space group $P2_1/n$ with 4 molecules in the unit cell (Z = 4). A representative unit cell is shown in Figure 5.5 and crystal metrics are provided in Table 5.2. Similar to the other RBBO radicals, the molecules are linked laterally by S---O′ and S---N′ intermolecular contacts that are inside the respective van der Waals separations.[10] However, each

radical is also coordinated to an acetonitrile (MeCN) molecule forming superimposed π-stacks along the *a*-axis. Lateral interactions are largely buffered by the acetonitrile molecules and thus a highly one-dimensional (1D) structure predominates.

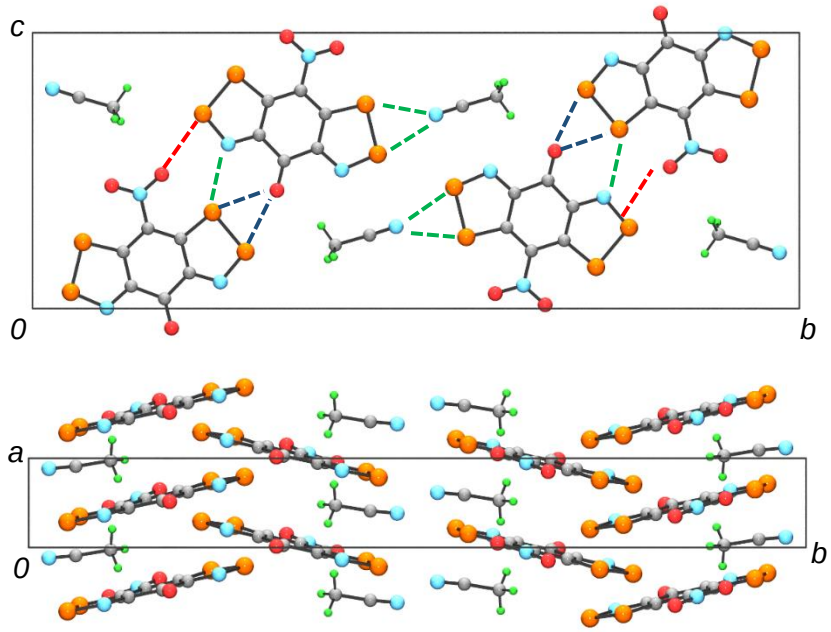

Figure 5.5 - Crystal structure of [**5-3**]·MeCN viewed along the *c*-axis and (top) and the superimposed π-stacks formed along the *a*-axis (bottom).

Table 5.2 – Preliminary crystal metrics for [**5-3**]·MeCN and [**5-3**]·$(EtCN)_{0.25}$.

Formula	$C_8H_3N_4O_3S_4$ [**5-3**]·MeCN	$C_{29}H_5N_{11}O_{12}S_{16}$ [**5-3**]·$(EtCN)_{0.25}$
M	331.38	1212.40
a, Å	3.54310(10)	25.0500(2)
b, Å	30.8063(6)	23.9595(3)
c, Å	11.1230(2)	14.9342(2)
β, deg	90.0835(11)	117.7780(5)
V, Å	1214.07(5)	7930.36(16)
ρ_{calcd} (g cm^{-1})	1.813	2.031
space group	$P2_1/n$	*C2/c*
Z	4	24
temp (K)	296(2)	296(2)
μ (mm^{-1})	0.790	0.954
λ (Å)	0.71073	0.71073
data/restr/parameters	2858/0/174	9553/0/613
solution method	direct methods	direct methods
R, R_w (on F^2)	0.0583, 0.1507	0.0483, 0.0950

Magnetic susceptibility (χT) measurements on [**5-3**]·MeCN were collected over the temperature range 2 – 300 K. Cooling curve plots of χ and χT versus temperature (Figure 5.6), measured using an external field of *H* = 1 kOe, indicate Pauli paramagnetic behaviour, the first time such an effect has been observed for these kinds of radicals. The data were fitted to a nonlinear function, affording a Pauli paramagnetic term of 6.56 x 10^{-4} emu mol^{-1} and a free (defect) spin concentration of 1.6%. There is no evidence for any structural or magnetic phase transitions upon cooling the material to 2K.

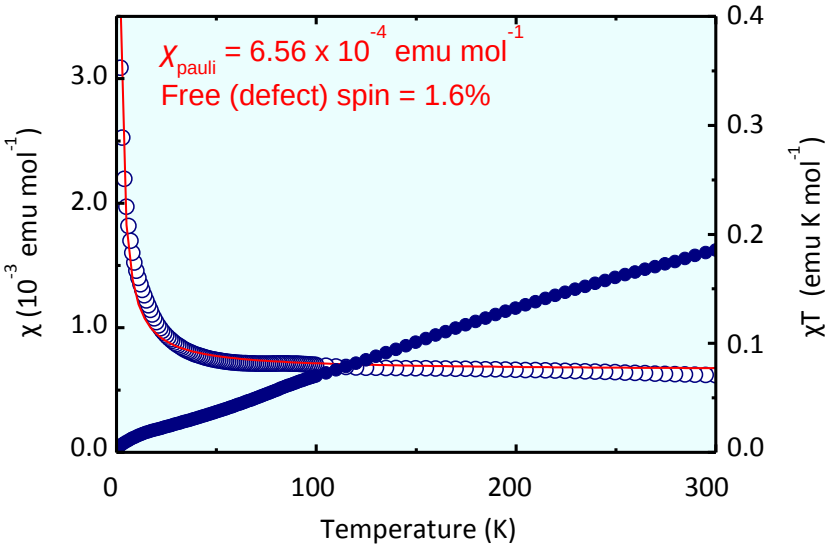

Figure 5.6 - Magnetic measurements χ and χT on [**5-3**]·MeCN over the temperature range 2 - 300 K, illustrating Pauli paramagnetic behavior. A non-linear fit of the data afforded a Curie (defect) spin concentration of 1.6%.

5.2.6 – Crystallography & Magnetic Properties of [5-3]·$(EtCN)_{0.25}$

In pursuit of a non-solvated structure, crystals for single X-ray crystallography were grown from propionitrile (EtCN). To our surprise, this gave rise to another solvated structure, this time crystallizing in the monoclinic space group C2/*c* with 32 molecules in the unit cell (*Z* = 8). Crystal metrics are shown in Table 5.2 and a representative cell drawing is shown in Figure 5.7. Indeed, the conventional S---O and S---N intermolecular contact are present, but unlike [**5-3**]·MeCN, 4 unique radicals are coordinated to one EtCN molecule resulting in a highly complex structure (Figure 5.7b). The peculiar arrangement of the radicals allows for many close S---S intermolecular contacts, which suggest the possibility of spin pairing. This was later confirmed by magnetic measurements, which indicated diamagnetic behaviour over the temperature range 2 – 300 K, shown in Figure 5.8.

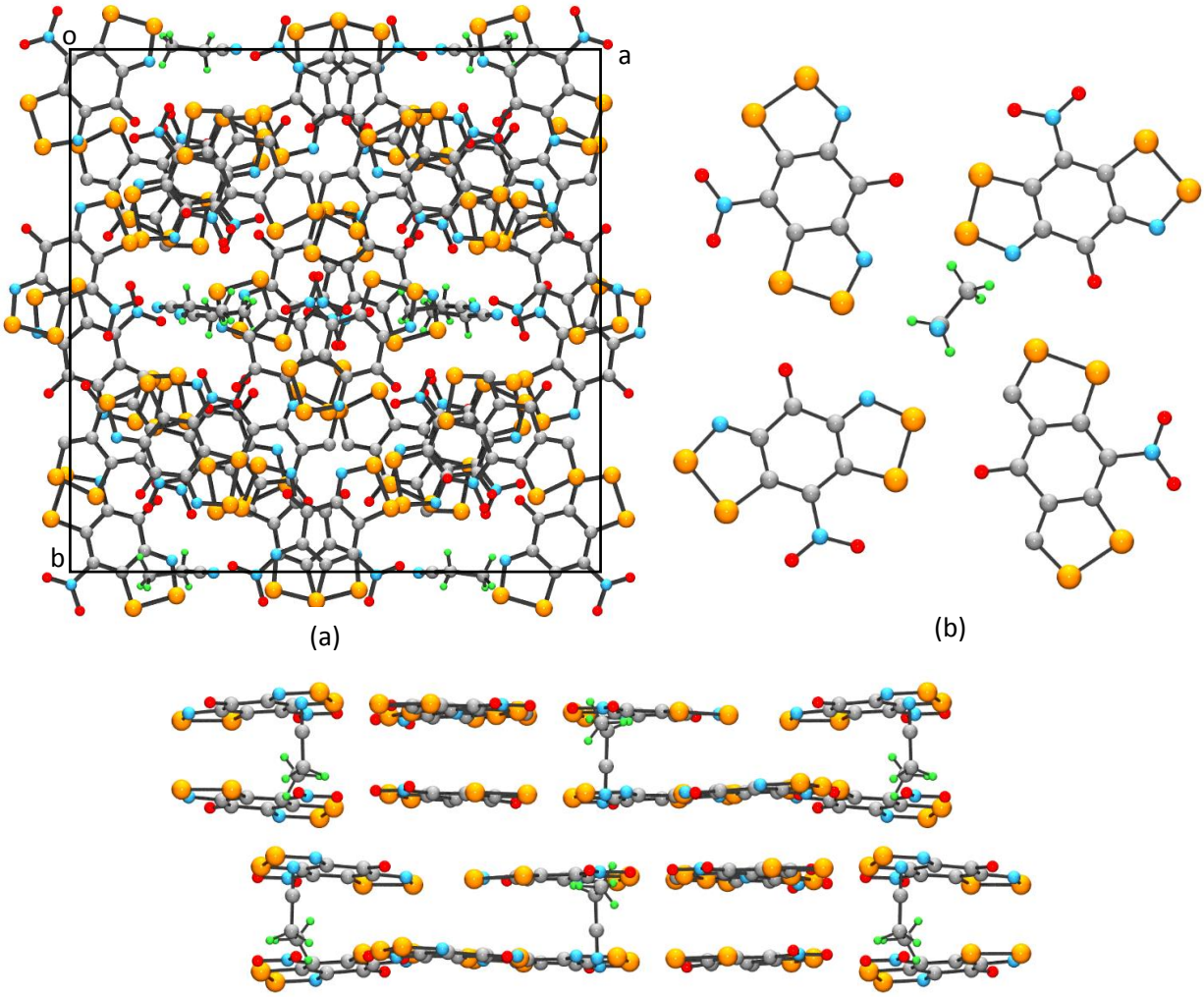

Figure 5.7 – (a) Top view of the unit cell down the *c*-axis of [**5-3**]·$EtCN_{0.25}$. (b) Asymmetric unit with 4 radicals coordinating to one EtCN molecule. (c) View along the *a*-axis of the complex molecular packing.

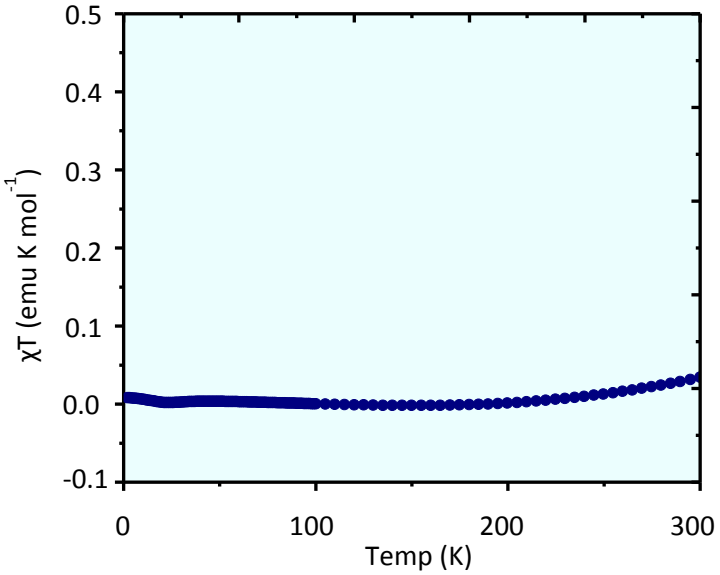

Figure 5.8 - Magnetic susceptibility measurements on [**5-3**]·$EtCN_{0.25}$, illustrating diamagnetic behavior over the temperature range 2-300 K.

5.2.7 – Variable Temperature Conductivity

Variable temperature 4-probe conductivity (σ) measurements on [**5-3**]·MeCN and [**5-3**]·$EtCN_{0.25}$ using cold-pressed pellets over the temperature range 300 to 130 K are shown in Figure 5.9, in the form of plots of log σ versus 1/*T*. Preliminary results from the pressed pellet data on [**5-3**]·MeCN and [**5-3**]·$EtCN_{0.25}$ indicate conductivities around 10^{-2} S cm^{-1} at ambient temperature, with activation energies of 0.09 eV and 0.12 eV, respectively. We were also able to wire and measure the 2-probe conductivity of a single crystal of [**5-3**]·MeCN, which afforded a marginal improvement in the room temperature conductivity but a much lower activation energy of 0.05 eV. Attempts to gain a more accurate measurement using a 4-probe single-crystal conductivity are currently underway.

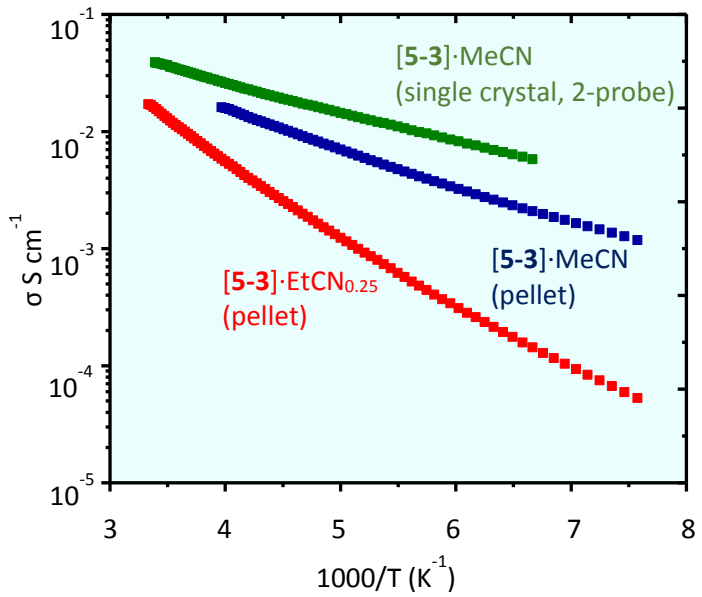

Figure 5.9 - Variable temperature conductivity on [**5-3**]·MeCN and [**5-3**]·$EtCN_{0.25}$, as well as single-crystal 2-probe conductivities.

In comparison to the other oxobenzene-bridged radicals, both phases, that is [**5-3**]·MeCN and [**5-3**]·$EtCN_{0.25}$, lie near the top of the pack, matching the fluoro-oxobenzene-bridged radical **5-2a** with an ambient temperature conductivity of 10^{-2} S cm^{-1}. Although a much lower *U* is exhibited by **5-3** than the fluoro-variant **5-2a**, its one-dimensional structure leads to much more anisotropic behavior. In the case of diamagnetic [**5-3**]·$EtCN_{0.25}$, while the structure may be spin-paired, the electronic bandwidth is still large enough to produce a reasonably small band-gap semiconductor. Overall, these oxobenzene-bridged radicals uniformly perform better in terms of conductivity and activation energies than the pyridine-bridged radicals **5-1** as a result of a combination of its improved molecular packing and electronic structure.

5.2.8 – UV-Vis spectroscopy

In previous chapters we established the importance of the low-lying LUMO in radicals **5-2** in determining their electrochemical and hence solid state transport properties. In the present chapter we have shown how the attachment of a NO_2 group on the basal site of these radicals leads to a further reduction in E_{cell} value, and hence improvement in charge transport. To complement these studies we have measured the UV-vis spectra of the pyridine-bridged cation [**5-1**]$^+$ (R_1 = R_2 = H) and the corresponding fluoro-, proto-, and nitro-cations [**5-2**]$^+$, and tracked the differences in the HOMO-LUMO excitation energy

of the cations with changes in the R-substituents. As may be seen in Figure 5.10, there is a steady decrease in λ_{max} on moving from the pyridine-bridged cation [**5-1**]$^+$ to the oxobenzene-bridged cations [**5-2**]$^+$, illustrating a widening of the HOMO-LUMO gap. Incorporation of a π-acceptor group, NO_2, results in a further blue-shift of λ_{max}. These results are consistent with TD-DFT calculations on the cations [**5-2**]$^+$ (R = F, H, NO_2) and [**5-1**]$^+$ (R_1 = R_2 = H), presented in Table 5.3.

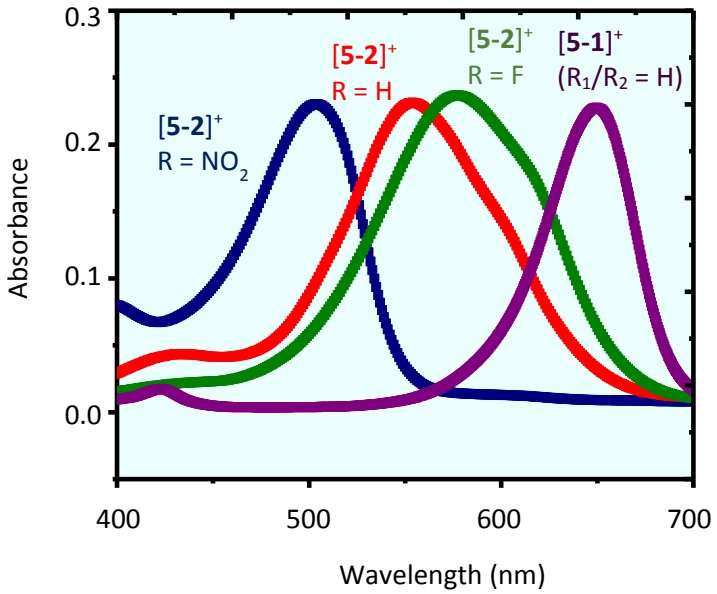

Figure 5.10 - (a) UV-vis spectra of the fluoro-, proto- and nitro- cations [**5-2**]$^+$ (R = F, H, NO_2) and pyridine-bridged cation [**5-1**]$^+$ (R_1 = H, R_2 = H) in acetonitrile. Absorbance maxima are normalized for ease of comparison.

To understand the variations in λ_{max} it is important to recall that replacement of the NH group in the radical [**5-1**] by a C=O moiety affects not only the b_1 LUMO (the SOMO+1), but also the b_1 HOMO (the SOMO-1). Both these orbitals are stabilized (lowered in energy) by the incorporation of the CO π* orbital, as illustrated in the correlation diagram in Figure 5.11. These changes in the SOMO-LUMO gap of the radical are mirrored in the HOMO-LUMO gap of the cation. To illustrate this effect Figure 5.11 shows the evolution of the frontier orbital energies of the cations [**5-1**]$^+$ (R_1 = R_2 = H) to [**5-2**]$^+$ (R = F, H, NO_2). The observed lowering of the upper and lower b_1 orbitals, and consequent increase in the HOMO-LUMO excitation energy of the cation, is readily understood in terms of the π-donor/acceptor properties of the basal R-group. Note also that in the case of R = NO_2 an additional low-lying orbital is introduced, to afford two low-lying b_1 virtual orbitals.

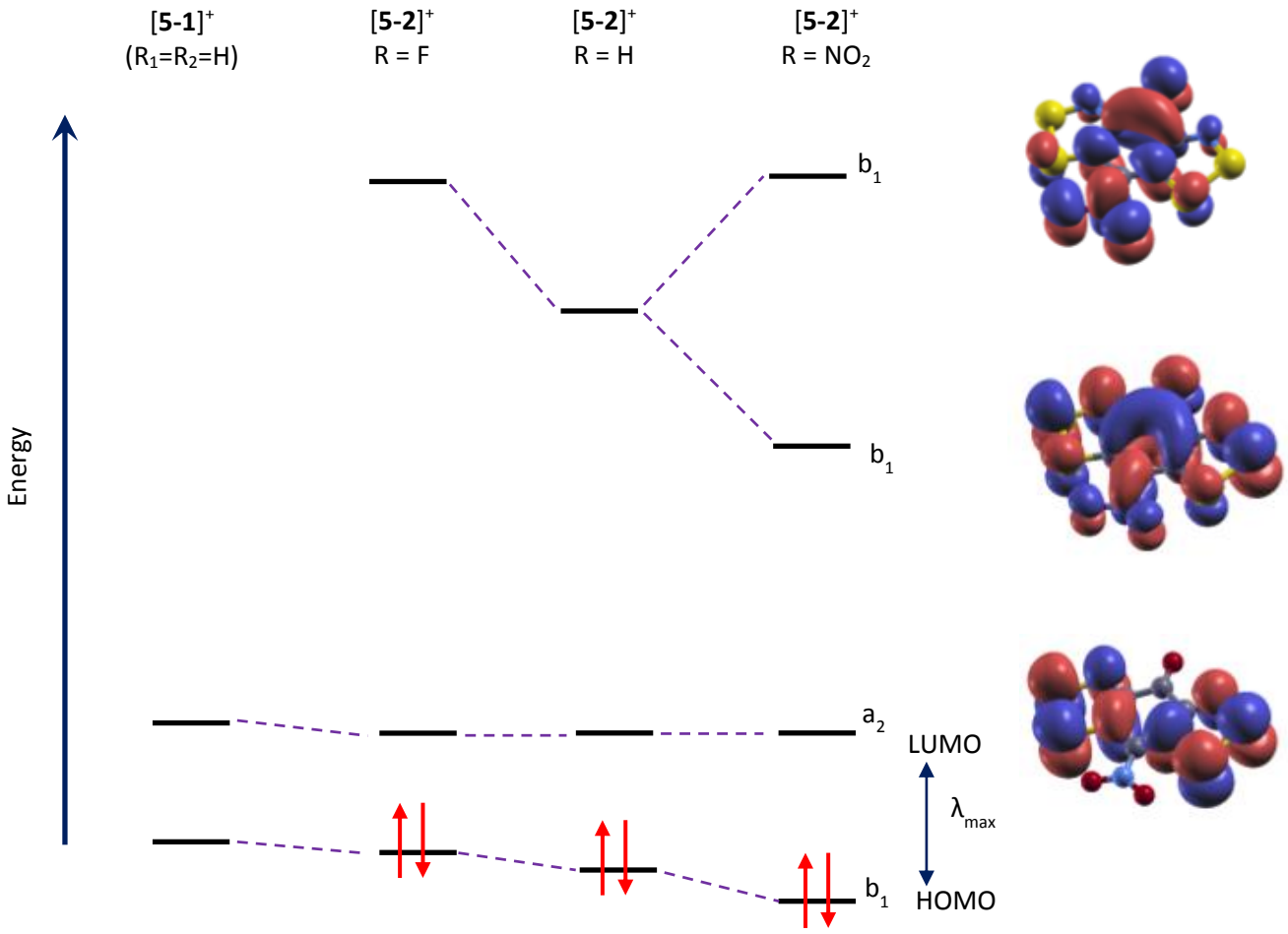

Figure 5.11 – Schematic orbital diagram of the HOMO-LUMO gap with various donor/acceptor molecules. The stabilization of the HOMO orbital is also seen in the higher b_1 virtual orbitals from [**5-1**]$^+$ to [**5-2**]$^+$ (R = NO_2).

Table 5.3 – Absorbance wavelengths obtained from the UV-vis spectra for the HOMO-LUMO excitation in [**5-2**]$^+$ (R = F, H and NO_2) and [**5-1**]$^+$ (R_1 = H, R_2 = H).

	λ_{max} [nm]	Calculated λ_{max} [nm]	Calculated Excitation Energy [eV]
[**5-1**]$^+$ (R_1= R_2 = H)	650	709	1.75
[**5-2**]$^+$ (R = F)	577	590	2.10
[**5-2**]$^+$ (R = H)	554	560	2.21
[**5-2**]$^+$ (R = NO_2)	505	504	2.46

5.2.9 – Band Calculations

Band calculations were performed on [**5-3**]·MeCN by a fellow student (Stephen Winter) using the Quantum Expresso package and atomic coordinates obtained from the crystal structure. The results, shown in Figure 5.12, displays two groups of four bands ($Z = 4$) arising from the SOMO (cyan), LUMO bands (red), and LUMO+1 bands (blue). As expected, a highly one-dimensional electronic structure with strong dispersion along the stacking axis (Γ → X) and negligible crystal orbital (CO) dispersion along the remaining two principle directions is observed. Consistently, the LUMO+1 band confirms the presence of another low-lying orbital discussed in the previous section. Moreover, the SOMO and low-lying LUMO bands overlap and track one another suggestive of minimal mixing between the two bands and congestion of the bands near the Fermi level suggest a ¼ bandfilling ($f = ¼$). Overall, the calculated bandwidth of 1 eV is exceptionally large, matching the calculated bandwidth of the chloro-oxobenzene-bridged radical (R = Cl) of 1.02 eV. However in the case of chloro-oxobenzene-bridged radical, the electronic structure is much more two-dimensional with its slipped-ribbon architecture.

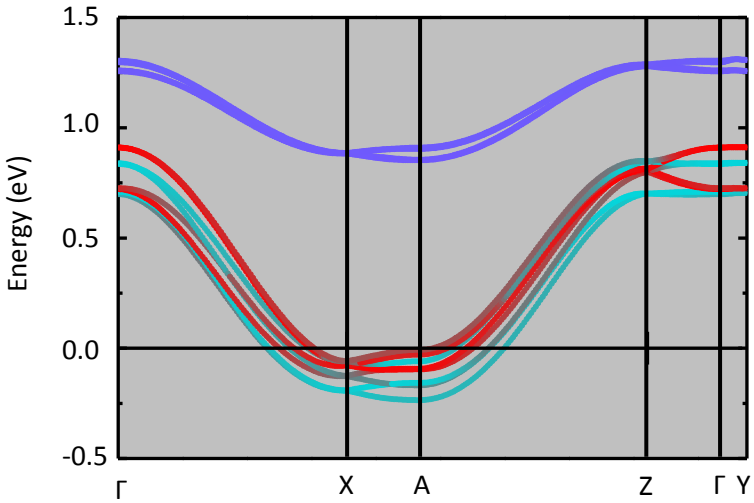

Figure 5.12 – Band calculations of the SOMO and LUMO bands of [**5-3**]·MeCN, suggestive of a highly one-dimensional electronic structure.

5.3 – Conclusion

We have successfully made the transition from the idea of a single-band radical to a multiple-band system with the recently developed oxobenzene-bridged radicals. The low-lying LUMO occasioned by the introduction of the carbonyl moiety makes these radicals electronically softer by virtue of an increase in their electron affinity. The design of new radicals of this type with improved solid-state packing and a decreased SOMO-LUMO gap is actively being pursued. In this chapter we have demonstrated that the

incorporation of a π-electron withdrawing group in the basal position is very effective in terms of reducing the electrochemical cell potential E_{cell}, and hence the onsite Coulomb barrier *U*. DFT calculations also indicate that the incorporation of a π-acceptor group decreases the SOMO-LUMO gap and hence the coulomb repulsion energy barrier *U*.

As mentioned earlier, this is still ongoing work, but we have successfully isolated two phases of the nitro-substituted radical, that is [**5-3**]·MeCN and [**5-3**]·$EtCN_{0.25}$; the ambient temperature conductivities both are the best within the oxobenzene-bridged radical family **5-2**. Although the solid-state packing of [**5-3**]·MeCN is highly one-dimensional, its 1D-electronic bandwidth is still large (1eV) affording near metallic conducting behavior. Further work on single crystal conductivity and magnetic measurements, as well as crystallography on the MEK phase are currently being pursued. High pressure work on [**5-3**] ·MeCN is also underway.

5.4 – Experimental Section

Preparation of ammonium 2-amino-4,6-dinitrophenolate. Ammonium sulfide solution (50 mL) was added slowly over 20 min to a yellow solution of picric acid (36.02 g, 157.0 mmol) in 600 mL of 20 % aq. NH_3 at 60 °C, never allowing the temperature to exceed 70 °C, to give a deep red mixture. The mixture was heated for 3 hrs, hot filtered on a large Buchner to remove a gray solid, and finally washed with 300 mL of hot distilled H_2O. The filtrate was concentrated to one third of the volume *in vacuo* at 60 °C, then cooled to 0 - 5 °C on an ice-bath for 2 hrs, and the dark purple needles were collected by filtration and air dried. The obtained product was boiled into 500 mL distilled H_2O, hot filtered and the filtrate concentrated *in vacuo* to 300 mL at 60 °C. The filtrate was cooled to RT before addition of 50 mL 28% aq. NH_3, which was left standing overnight to give dark purple black needles (28.10 g, 130.0 mmol, 83 % yield). ^{1}H-NMR (d^6-DMSO) δ: 8.153 (d, C-H, J_4 = 2.7 Hz, 1H), 7.012 (s, broad; NH_4^+, 4H), 6.955 (d, C-H, J_4 = 2.7 Hz, 1H), 5.087 (s, broad; N-H, 2H). IR (cm^{-1}): 3407 (m), 3313 (w), 3277 (br, m), 3158 (br, m), 1614 (sh, m), 1589 (m), 1537 (s), 1311 (s), 1262 (br, vs), 1189 (w), 1123 (w), 1069 (m), 997 (vw), 936 (w), 888 (w), 856 (w), 828 (w), 734 (m), 707 (w), 558 (w), 486 (m).

Preparation of 2-amino-4,6-dinitrophenol, 5-5. Glacial acetic acid (20 mL) was added dropwise to a stirred solution of ammonium 2-amino-4,6-dinitrophenolate (18.89 g, 87.39 mmol) in 250 mL of warm H_2O (~ 60 °C). The mixture was cooled on an ice-water bath and the orange precipitate was collected by filtration and air dried (15.68 g, 78.75 mmol, 79 %). The orange powder was boiled into EtOAc to give orange needles; mp = 169 - 171 °C. ^{1}H-NMR ($CDCl_3$) δ: 11.178 (s, O-H, 1H), 8.392 (s, C-H, 1H), 7.730 (s, C-H, 1H), 4.478 (s, broad; N-H, 2H). IR (cm^{-1}): 3485 (m), 3470 (m), 3250 (br, s), 3117 (w), 3104 (w), 3072 (w), 1783 (w), 1615 (s), 1595 (s), 1557 (vs), 1507 (s), 1401 (m), 1338 (vs), 1299 (vs), 1233 (vs), 1141 (s), 1110 (s), 1064 (s), 994 (s), 934 (s), 895 (m), 880 (w), 855 (w), 816 (m), 804 (m), 771 (w), 736 (m), 725 (w), 711 (m), 675 (s), 569 (vw), 491 (w).

Preparation of 2,6-diamino-4-nitrophenol, 5-6. A mixture of 2-amino-4,6-dinitrophenol (5.001 g, 25.12 mmol) L-ascorbic acid (22.18 g, 125.9 mmol), and a catalytic amount of $FeSO_4 \cdot 7H_2O$ (0.793 g, 2.85 mmol) in 400 mL of 1.0 M NaOH was heated at 70 °C for 5 hrs. The deep red mixture was hot filtered on a large Buchner and cooled to 0 – 5 °C on an ice-water bath. Glacial acetic acid was added dropwise to a rapidly stirred, cold mixture, until pH ~ 5 was obtained and after 2 hours a light brown solid was collected by filtration and air dried. Recrystallization from hot H_2O afforded dark orange needles (2.459 g, 14.54 mmol, 58 % yield). mp = 168-169 °C (decomp. > 170 °C), ESI+ (1:1 MeOH/H_2O + 0.1% formic acid) m/z = 170.08 ($M+H^+$). ^{1}H-NMR (d^6-DMSO) δ: 6.883 (s, C-H), 5.890 (broad, N-H). IR (cm^{-1}): 3489 (m), 3471 (m),

3250 (br, s), 3121 (w), 3105 (w), 3077 (w), 1783 (w), 1635 (m), 1615 (m), 1595 (m), 1554 (s), 1516 (s), 1444 (m), 1401 (m),1338 (vs), 1304 (s), 1237 (s), 1143 (m), 1112 (m), 1066 (m), 995 (m), 935 (m), 894 (w), 880 (w), 856 (vw), 817 (w), 806 (w), 771 (w), 736 (m), 712 (m), 676 (s), 590 (vw), 491 (w).

Preparation of 8-nitro-4-oxo-4H-benzo[1,2-d:5,4-d']bis([1,2,3]dithiazole)-2-ium chloride 5-7. A solution of sulfur monochloride (4.0 mL, 6.8 g, 50.1 mmol) in 25 mL MeCN was added drop wise to a suspension of 2,6-diamino-4-nitrophenol **5-6** (1.695 g, 10.02 mmol) in 200 MeCN and the mixture was heated under gentle refluxed for 6 hrs. The black precipitate was filtered off, washed thoroughly with MeCN, hot DCE, CS_2 / DCM mixture (1:4 v/v), DCM and dried *in vacuo* (2.290 g 7.029 mmol, 70 % yield). mp > 250 °C. IR (cm^{-1}): 1710 (s), 1626 (br, s), 1503 (vs), 1343 (m), 1291 (sh, m), 1277 (s), 1099 (vw), 1074 (w), 1017 (vw), 949 (w), 863 (w), 852 (w), 825 (w), 762 (m), 746 (w), 632 (vw), 613 (vw), 602 (vw), 568 (vw), 493 (m), 465 (w).

Preparation of 8-nitro-4-oxo-4H-benzo[1,2-d:5,4-d']bis([1,2,3]dithiazole)-2-ium 5-8 Silver triflate (4.101 g, 15.96 mmol) was added to a slurry of crude [**5-3**][Cl] (4.550 g, 13.97 mmol) in 200 mL anhydrous MeCN, to afford a deep red solution, which was gently heated at reflux for 90 min, then filtered to remove gray-black precipitate of AgCl. The deep red solution was concentrated to 45 mL MeCN and a dark green-black solid was obtained upon cooling, which was collected by filtration and repeatedly recrystallized from hot MeCN to give dark green shards of [**5-3**][OTf] (1.978 g, 4.501 mmol, 32 % yield); mp > 250 °C. IR (cm^{-1}): 1692 (vs), 1515 (vs), 1402 (m), 1290 (s), 1246 (br, vs), 1224 (m), 1181 (m), 1157 (m), 1102 (w), 1077 (w), 1024 (m), 954 (w), 886 (w), 863 (w), 833 (w), 781 (vw), 767 (m), 634 (s), 611 (w), 574 (w), 520 (w), 502 (vw), 488 (w), 470 (w).

Preparation of [5-3]·MeCN. Method 1. Bulk Material for Conductivity and Magnetic Measurements. A solution of [**5-3**][OTf] (0.270 g, 0.614 mmol) in 100 mL of degassed MeCN (4 freeze-pump-thaw cycles) was filtered onto a solution of OMFc (0.240 g, 8.047 mmol) in 85 mL of similarly degassed MeCN to yield a dark blue solution over a dark green-black microcrystalline precipitate. After 30 min of stirring at RT, the microcrystalline product was filtered off, washed with MeCN (4 x 20 mL) and dried *in vacuo* (0.145 g, 0.499 mmol, 81 % yield); mp = 250 °C (decomp.). IR (cm^{-1}): 1595 (br, vs), 1536 (br, s), 1490 (s), 1293 (br, vs), 1234 (s), 1129 (m), 1059 (m), 974 (w), 867 (m), 860 (sh, m), 812 (m), 758 (m), 738 (m), 635 (vw), 595 (w), 557 (w), 489 (m), 465 (w), 443 (w), 422 (w). **Method 2. Slow Diffusion for Single Crystals.** A solution of [**5-3**][OTf] (44 mg, 0.100 mmol) in 12 mL of degassed MeCN (5 freeze-pump-thaw cycles) was allowed to diffuse slowly into a similarly degassed 20 mL solution of OMFc (32 mg, 0.107 mmol) over 16 hr period, affording [**5-3**]·MeCN as long dark green-black needles.

Appendix A

General Experimental and Computational Methods

A.1 Procedures

A.1.1 General Procedures

Many of the reactions were performed under an inert atmosphere of nitrogen. Those reactions carried out in solution were handled by standard or modified Schlenk techniques using a double-manifold glass vacuum line (nitrogen/vacuum) with an Edwards E2M series rotary vacuum pump. Air sensitive solids were handled and stored in a nitrogen-filled Braun MB-150M dry box.

A.1.2 Diffusion H-cell Crystallizations

Diffusion H-cell experiments are especially useful for the preparation of air and/or moisture sensitive materials such as neutral radicals, as a thorough degassing of the solvent is possible. A diffusion H-cell apparatus is illustrated in Figure A.1 and a typical experiment proceeds as follows: two solutions containing each reactant are placed in each of the round bottom flasks and the cell is oriented as shown in Figure A.1a. The solutions undergo 5 freeze-pump-thaw cycles to ensure all the oxygen has been removed from the vessel. The apparatus may be kept under vacuum or flooded with an inert gas (argon or nitrogen). The H-cell is then inverted and tipped slightly askew as depicted in Figure A.1b, to allow the two solutions to combine slowly. One solution flows through the glass frit into the other resulting in crystal growth of the product at the interface of the two solutions.

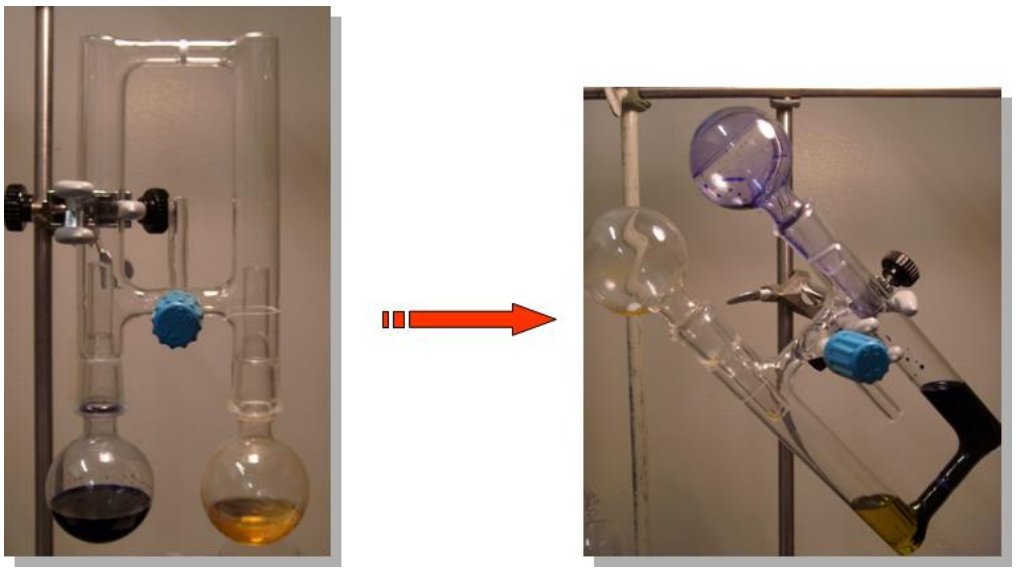

Figure A.1 – (a) Diffusion H-cell apparatus and (b) tipping of the apparatus for single crystal growth

A.2 Techniques

A.2.1 – DFT Calculations

DFT calculations were run on PC workstations using the UB3LYP method[1] available in the Gaussian 98W[2] and Gaussian 09W[3] suite of programs.

A.2.2 – NMR Spectra

^{1}H NMR spectra were collected on a Bruker Avance 300 MHz NMR spectrometer

A.2.3 – Infrared Spectral Analysis

Infrared spectra were recorded (at 2 cm-1 resolution) as Nujol mulls or neat liquids on KBr plates, on a Nicolet Avatar 320 FT infrared spectrometer.

A.2.4 – Mass Spectrometry

Low resolution mass spectra (70 eV, EI, DEI, and CI, DCI) were run on either a Micromass Q-TOF Ultima Global LC/Ms/MS system or a JEOL Hx110 double focusing mass spectrometer at the WATSPEC Mass Spectrometry Facility.

A.2.5 – Cyclic Voltammetry

Cyclic voltammetry experiments were performed using a PINE Bipotentiostat, Model AFCCIBPI, on dry acetonitrile solutions containing 0.1 M tetra-*n*-butylammonium hexafluorophosphate. Scan rates of 50 – 100 mV s-1 were employed. Potentials were scanned from -2.5 to 2.0 V with respect to the quasi-reference electrode in a single compartment cell fitted with Pt electrodes. The potentials were referenced to the ferrocenium/ferrocene couple at 038 V vs SCE and are cited relative to SCE in CH_3CN.[4]

A.2.6 – EPR Spectra

The X-band EPR spectra were recorded on toluene solutions of the radical at ambient temperature using a Bruker EMX spectrometer. Hyperfine coupling constants were obtained by spectra simulation using Simfonia[5] and WinSim.

A.2.7 – Elemental Analysis

Elemental analyses were performed by MHW Laboratories, Phoenix, AZ.

A.2.8 – Ambient Pressure Magnetic Susceptibility Measurements

DC magnetic susceptibility measurements were performed over the range 2 – 300 K on a Quantum Design MPMS Squid magnetomer. AC susceptibility were performed on an Oxford Instruments MagLab EXA. The results were corrected for diamagnetic contributions using Pascal's constants.[6]

A.2.9 – Ambient Pressure Conductivity Measurements

Ambient pressure conductivity on pressed pellet samples were made using a four-probe configuration on either a Quantum Design PPMS instrument or a home-made device, to measure the voltage drop under dynamic vacuum. Silver paint was used to apply the electrical contacts.

A.2.10 – Ambient Pressure Single Crystal and Powder X-ray Diffraction

Single crystal X-ray data were collected at ambient temperature using phi and omega scans with a (i) Bruker APEX I CCD detector on a D8 3-circle goniometer (University of Waterloo). All data were scanned using Bruker's SMART program and integrated using Bruker's SAINT software[7] or by the APEX II software package. The structure was solved by direct methods using SHELXS-90[8] and refined by least-squares methods on F^2 using SHELXL-97[9] incorporated into the SHELXTL suite of programs.[10] Agreement indices were calculated as follows:

$$R = \frac{[\sum |F_o| - |F_c|]}{[\sum (F_o)]}$$

$$R_w = \left\{ \frac{[\sum w(|F_o| - |F_c|)^2]}{[\sum w|F_o|]^2} \right\}^{1/2}$$

A single microcrystal of **3-3a** was mounted on a MiTeGen MicroMount using Fomblin oil. The data were measured on beamline I19 at the Diamond Light Source, collected using Rigaku CrystalClear software[11] and processed with Bruker APEX2 software and SADABS.[12]

Powder data were collected on an X-ray powder diffractometer with a position sensitive detector (INEL) at ambient temperature using Cu Kα radiation (λ = 1.5406 Å). The structures were obtained using DASH to index the unit cell and for simulated annealing to solve the structures, and GSAS to refine the solutions. Agreement indices were calculated as follows:

$$R_p = \frac{[\sum |I_o| - |I_c|]}{[\sum (I_o)]}$$

$$R_{wp} = \left\{ \frac{[\sum (I_o - I_c)^2]}{\sum w(I_o)^2} \right\}^{1/2}$$

A.3 Sources of Starting Materials

A.3.1 – Purchased Chemicals that were used as Received

Lithium bis(trimethylsilyl)amide	Aldrich
4-cyanopyridine	Aldrich
Tetrahydrofuran	Aldrich
Sulfur monochloride	Aldrich
Triphenylantimonyl	Aldrich
Tin (II) chloride dehydrate, 98%	Alfa Aesar
Tin powder, 100 mesh, 99.5% (metals basis)	Alfa Aesar
Ammonium thiocyanate	Alfa Aesar
Bromine	Fisher
Sodium sulfide nonahydrate	Alfa Aesar
Thionyl chloride	Acros
Sodium nitrate	Aldrich
4-hydroxylpyridine	Alfa Aesar
Benzyl mercaptan	Aldrich
Sodium thiomethoxide	Aldrich
Sodium nitrite	Fisher
p-toluenesulfonic acid	Aldrich
Picric acid	Aldrich
Silver trifluoromethanesulfonate	SynQuest
Acetic acid, glacial	Fisher
Ammonium hydroxide (aqueous)	Fisher
Calcium hydride	Fisher
Chloroform-*d*	Isotec
Dimethylsulfoxide-*d*	Isotec
Methanol	Fisher
Nitrogen gas	in-house supply
Octamethylferrocene	Aldrich
Carbon disulfide	Aldrich
Dimethylferrocene	Strem Chemicals

Ethanol-95%	Fisher
Hydrochloric acid, 36%	Fisher
Nitric acid, 68%	Fisher
Sulfuric acid, 98%	Fisher
Selenium powder, mesh, 99.5%	Aldrich

A.3.2 Solvents Purified Prior to Use

Acetonitrile (Caldeon) – distilled from P_2O_5 or CaH_2

Proponitrile (Fluka/Alfa Aesar) – Distilled from P_2O_5 and CaH_2 after purification

Purification of propionitrile. Propionitrile (1 L) was stirred with 20% HCl (200 mL) for 1 hour, washed with water and neutralized with K_2CO_3. The organic phase was collected and dried over molecular sieves and CaH_2. Propionitrile was distilled from P_2O_5 and CaH_2.

A.3.3 – Chemicals Prepared "In House"

Preparation of Selenium tetrachloride. Chlorine gas was bubbled into a solution of selenium powder (5.00 g, 63.32 mmol) in 120 mL of freshly distilled acetonitrile for 10 minutes. The vessel was flooded with nitrogen gas, then the solid was filtered, washed with dry acetonitrile and pumped dry (10 g, 36.22 mmol, 57% yield).

References

References for Chapter 1

(1) Tanko, J. M. *Annu. Rep. Prog. Chem*. Sect. B., **2006**, 102, 247. (b) Fleming, I. Frontier Orbitals and Organic Chemical Reactions, John Wiley & Sons, Ltd., Great Britain, 1976, 182.

(2) Griller, D.; Ingold, K. U. *Acc. Chem. Res*. 1976, 9, 13.

(3) (a) Hicks, R. G. *Org. Biomol. Chem*. **2007**, 5, 1321. (b) Power, P. *P. Chem. Rev*. **2003**, 103, 789. (b) Hicks, R. G. Ed. Stable Radicals: Fundamentals and Applied Aspects of Odd-Electron Compounds; J. Wiley and Sons, **2010**.

(4) Berliner, L. J. Spin Labelling: Theory and Applications, Academic Press, New York, 1979.

(5) (a) Perkins, M. J. Adv. Phys. Org. Chem. 1980, 17, 1. (b) Rehorek, D. *Chem. Soc. Rev*. **1991**, 20, 341. (c) Beckwith, A. L. J.; Bowry, V. W.; Ingold, K. U. *J. Am. Chem. Soc.* **1992**, 114, 4983. (d) Bowry, V. W.; Ingold, K. U. *J. Am. Chem. Soc*. **1992**, 114, 4992.

(6) (a) Yordanov, A. T.; Yamada, K.; Krishna, M. C.; Mitchell, J. B.; Woller, E.; Cloninger, M.; Brechbiel, M.W. *Angew. Chem. Int. Ed*. **2001**, 40, 2690. (b) Reddy, T. J.; Iwama, T.; Halpern, H. J.; Rawal, V. H. *J. Org. Chem.* **2002**, 67, 4635.

(7) (a) Hawker, C. J.; Bosman, A. W.; Harth, E. *Chem. Rev*. **2001**, 101, 3661. (b) Georges, M. K.; Veregin, R. P. N.; Kazmaier, P. M.; Hamer, G. K. Macromolecules. **1993**, 26, 2987.

(8) McCoy, H. N.; Moore, W. C. *J. Am. Chem. Soc*. **1911**, 33, 273.

(9) Mott, N. F. Metal-insulator Transitions; Taylor and Francis: London, 1990.

(10) Torrance, J.B.; *Acc. Chem. Res.* **1979**, 12, 79.

(11) Heisenberg, W. Z. Z. Phys. **1926**, 38, 411.

(12) Deumal, M.; Robb, M. A.; Novoa, J. J. Prog. *Theo. Chem. Phys*. **2007**, 16, 271.

(13) Noodleman, L.; Norman, J. G. *J. Chem. Phys.* **1979**, 70, 4903. (b) Noodleman, L. J. *Chem. Phys.* **1981**, 74, 5737.

(14) (a) Murugesu, M.; Wernsdorfer, W.; Christou, G.; Brechin, E. K. *Polyhedron,* **2007**, 26, 1845. (b) Nihei, M.; Yoshida, A.; Koizumi, S.; Oshio, H. *Polyhedron*, **2007**, 26, 1997. (c) Stamatotos, T. C.; Abboud, K. A.; Wrnsdorfer, W.; Christou, G. *Polyhedron*, **2007**, 26, 2042.

(15) (a) Rahman, B.; Kanbara, K.; Akutsu, H.; Yamada, J.; Nakatsuji, S. *Polyhedron*, **2007**, 26, 2287. (b) Koizumi, K.; Shoji, M.; Kitagawa, Y.; Takeda, R.; Yamanaka, S.; Kawakami, T.; Okumura, M.; Yamaguchi, K. *Polyhedron*, **2007**, 26, 2135. (c). Harvey, M. D.; Pace, J. T.; Yee, G. T. *Polyhedron*, **2007**, 26, 2037.

(16) (a) Sessoli, R.; Tsai, H. –L.; Schake, A. R.; Wang, S.; Vincent, J. B.; Folting, K.; Gatteschi, D.; Christou, G.; Hendrickson, D. N. *J. Am. Chem. Soc*. **1993**, 115, 1804. (b) Sessoli, R.; Gatteschi, D.; Caneschi, A.; Novak, M. A. *Nature* **1993** , 365, 141. (c) Lis, T. *Acta. Cryst*. **1980**, B36, 2042.

(17) G. Chaboussant, A. Sieber, S. Ochsenbein, H.-U. Güdel, and M. Murrie, A. Honecker and N. Fukushima, B. Normand. *Phys. Rev. B*, **2004**, 70, 104422.

(18) Fujita, W.; Awaga, K. *Chem. Phys. Lett*. **2002**, 357, 385.

(19) Allemand, P.; Khemani, K. C.; Koch, A.; Wudl, F.; Holczer, K.; Donovan, S.; Grunner, G.; Thompson, J. D. *Science* **1991**, 253, 301.

(20) (a) Takahashi, M.; Turek, P.; Nakazawa, Y.; Tamura, M.; Nozawa, K.; Shiomi, D.; Ishikawa, M.; Kinoshita, M. *Phys. Rev. Lett*. **1991**, 67, 746. (b) Tamura, M.; Nakazawa, Y.; Shiomi, D.; Nozawa, K.; Hosokoshi, Y.; Ishikawa, M.; Takahashi, M.; Kinoshita, M. *Chem. Phys. Lett.* **1991**, 186, 401.

(21) Chiarelli, R.; Novak, M. A.; Rassat, A.; Tholence, J. L. *Nature* **1993**, 363, 147.

(22) Alberola, A.; Less, R. J.; Pask, C. M.; Rawson, J. M.; Palacio, F.; Oliete, P.; Paulsen, C.; Yamaguchi, A.; Murphy, D. M.; Farley, R. D. *Angew. Chem., Int. Ed.*, **2003**, 42, 4782.

(23) (a) Palacio, F.; Antorrena, G.; Castro, M.; Burriel, R.; Rawson, J. M.; Smith, J. N. B.; Bricklebank, N.; Novoa J.; Ritters, C. *Phys. Rev. Lett.* **1997**, 79, 2336. (b) Banister, A. J.; Bricklebank, N.; Lavender, I.; Rawson, J. M.; Gregory, C. I.; Tanner, B. K.; Clegg, W.; Elsegood, M. R. J.; Palacio, F. *Angew. Chem. Int. Ed.* Engl. **1996**, 35, No. 21, 2533.

(24) (a) Robertson, C. M.; Myles, D. J. T.; Leitch, A. A.; Reed, R. W.; Dooley, D. M.; Frank, N. L.; Dube, P. A.; Thompson, L. K.; Oakley, R. T. *J. Am. Chem. Soc*. **2007**, 129, 12688. (b) Robertson, C. M.; Leitch, A. A.; Cvrkalj, K.; Reed, R. W.; Myles, D. J. T.; Dube, P. A.; Oakley, R. T. *J. Am. Chem. Soc*. **2008**, 130, 8414.

(25) (a) Okamoto, Y.; Brenner, W. Organic Semiconductors, Rheinhold (1964). (b) Akamatu, H.; Inokuchi, H.; Matsunaga, Y. *Nature* **1954**, 173, 4395.

(26) Shirakawa, H.; Louis, E. J.; MacDiarmid, A. G.; Chiang, C. K.; Heeger, A. *J. Journal of the Chemical Society, Chemical Communications* **1977**, 16, 578.

(27) Bechgaard, K.; Carneiro, K.; Rasmussen, F. B.; Rindorf, O. G.; Jacobsen, C. S.; Pedersen, H. J.; Scott, J. C. *J. Am. Chem. Soc.* **1981**, 103, 2440.

(28) Kobayashi, A.; Fujiwara, E.; Kobayashi. H. *Chem. Rev.* **2004**, 104, 5243.

(29) Cordes, A. W.; Haddon, R. C.; Oakley, R. T. *Phosphorous, Sulfur, and Silicon*. **2004**, 197, 673.

(30) (a) Ferraris, J.; Cowan, D. O.; Walatka, V. V., Jr.; Perlstein, J. H. *J. Am. Chem. Soc*. **1973**, 95, 948. (b) Coleman, L. B.; Cohen, M. J.; Sandman, D. J.; Yamagishi, F. G.; Garito, A. F. and Heeger, A. J. *Solid State Commun.* **1973**, 12, 1125.

(31) (a) Bendikov, M.; Wudl, F.; Perepichka, D. F. *Chem. Rev*. **2004**, 104, 4891. (b) Jérome, D. *Chem. Rev.* **2*0*04**, 104, 4891. (c) Geiser, U.; Schleuter, J. A. *Chem. Rev*. **2004**, 104, 5203. (d) Yamada, J.; Akutsu, H.; Nishikawa, H.; Kikuchi, K. *Chem. Rev.* **2004**, 104, 5057.

(32) Garito, A. F.; Heeger, A. J. *Acc. Chem. Res.*, **1974**, 7(7), 232.

(33) Bechgaard, K.; Jacobsen, C. S.; Mortensen, K.; Pedersen, H. J.; Thorup, N. *Solid State Commun.* **1980**, 33, 5347.

(34) (a) Williams, J. M.; Emge, T. J.; Wang, H. H.; Beno, M. A.; Copps, P. T.; Hall, L. N.; Carlson, K. D.; Crabtree, G. W. *Inorg. Chem.* **1984**, 23, 2558. (b) Shibaeva, R. P.; Yagubskii, E. B. *Chem. Rev*. **2004**, 104, 5347.

(35) Tanaka, H.; Okano, Y.; Kobayashi, H.; Suzuki, W.; Kobayashi, A. *Science*, **2001**, 291, 285.

(36) Kobayashi, A.; Fujiwara, E.; Kobayashi. H. *Chem. Rev.* **2004**, 104, 5243.

(37) (a) Haddon, R. C. *Nature* **1975**, 256, 394. (b) Haddon, R. C. *Aust. J. Chem.* **1975**, 28, 2343.

(38) Peierls, R. C. Quantum Theory of Solids; Oxford University Press: London, U. K., 1955, pp 108.

(39) Gomberg, M. *J. Am. Chem. Soc*. **1900**, 22, 757.

(40) Neuman, W. P.; Uzick, W.; Zarkadis, A. K. *J. Am. Chem. Soc*. **1986**, 108, 3762.

(41) (a) Sabacky, M. J.; Johnson, C. S.; Smith, R. G.; Gutowsky, H. S.; Martin, J. C. *J. Am. Chem. Soc*. **1967**, 89, 2054. (b) Reid, D. H. *Tetrahedron* **1958**, 3, 339. (c) Sogo, B. P.; Nakazaki, M.; Calvin, M. *J. Chem. Phys.* **1957**, 26, 1343.

(42) Neugebauer, F. A.; Umminger, I. *Chem. Ber*., **1980**, 113, 1205.

(43) Zaitsev, V.; Rosokha, S. V.; Head-Gordon, M.; Kochi, J. K. *J. Org. Chem*. **2006**, 71, 520.

(44) Reid, D. H. *Quart. Rev.* **1965**, 19, 274.

(45) O'Connor, G. D.; Troy, T. P.; Roberts, D. A.; Chalyavi, N.; Fückel, B.; Crossley, M. J.; Nauta, K.; Stanton, J. F.; Schmidt, T. W. *J. Am. Chem. Soc*. **2011**, 133, 14554.

(46) (a) Koutentis, P. A.; Haddon, R. C.; Oakley, R. T.; Cordes, A. W.; Brock, C. P. *Acta Crystallogr*. **2001**, B57, 680. (b) Koutentis, P. A.; Chen, Y.; Cao, Y.; Best, T. P.; Itkis, M. E.; Beer, L.; Oakley, R. T.; Cordes, A. W.; Brock, C. P.; Haddon, R. C. *J. Am. Chem. Soc*. **2001**, 123, 3864.

(47) (a) Goto, K.; Kubo, T.; Yamamoto, K.; Nakasuji, K. Sato, K.; Shiomi, D.; Takui, T.; Kubota, M.; Kobayashi, T.; Yakusi, K.; Ouyang, J. Y. *J. Am. Chem. Soc.* **1999**, 121, 1619. (b) Lu, J. M.; Rosokha, S. V.; Kochi, J. K. *J. Am. Chem. Soc.* **2003**, 125, 12161. (c) Small, D.; Zaitsev, V.; Jung, Y. S.; Rosokha, S. V.; Head-Gordon, M.; Kochi, J. K. *J. Am. Chem. Soc.* **2004**, 126, 13850. (d) Small, D.; Rosokha, S. V.; Kochi, J. K.; Head-Gordon, M. *J. Phys. Chem.* **2005**, 56, 109, 11261. (e) Zaitsev, V.; Rosokha, S. V.; Head-Gordon, M.; Kochi, J. K. *J. Org. Chem*. **2006**, 71, 520.

(48) Sitzmann, H.; Bock, H.; Boese, R.; Dezember, T.; Havlas, Z.; Kaim, W.; Moscherosch, M.; Zanathy, L. *J. Am. Chem. Soc.* **1993**, 115, 12003.

(49) Coulson, C. A. Valence, 2nd Ed.; Oxford University Press: London, **1961**. (b) March, J. Advanced Organic Chemistry: Reactions, Mechanisms, and Structure; McGraw-Hill, Inc.: New York, 1977.

(50) Griffith, O. H.; Waggoner, A. S. *Acc. Chem. Res*. **1969**, 2, 17.

(51) Kuhn, R.; Trischmann, H. *Angew. Chem., Int. Ed. Engl*. **1963**, 3, 155.

(52) Neugebauer, F. A.; Fischer, H.; Siegel, R. *Chem. Ber.* **1988**, 121, 815.

(53) Beer, L.; Reed, R. W.; Robertson, C. M.; Oakley, R. T.; Tham, F. S.; Haddon, R. C. *Org. Lett*. **2008**, 10, 3121.

(54) Beer, L.; Mandal, S. K.; Reed, R. W.; Oakley, R. T.; Tham, F. S.; Donnadieu, B.; Haddon, R. C. *Cryst. Growth Des.* **2007**, 7, 802.

(55) (a) Green, R. L.; Street, G. B.; Suter, L. *J. Phys. Rev. Lett.* **1975**, 34, 577. (b) Labes, M. M.; Love, P.; Nichols, L. F. *Chem. Rev*. **1979**, 79, 1. (c) Banister, A. J.; Gorrell, I. B. *Adv. Mater*. **1998**, 1415.

(56) Rawson, J. M.; Banister, A. J.; Lavender, I., in Advances in Heterocyclic Chemistry, **1995**, 62, 137.

(57) Rawson, J. M.; Alberola, A.; Whalley, A. *J. Mater. Chem*. **2006**, 16, 2560.

(58) Hicks, R. G. In Stable Radicals: Fundamentals and Applied Aspects of Odd-Electron Compounds; Hicks, R. G., Ed.; John Wiley & Sons, Ltd.: Wiltshire, U.K., **2010**; pp 317 – 380.

(59) Kennett, F. A.; MacLean, G. K.; Passmore, J.; Rao M. N. S*. J. Chem. Soc. Dalton Trans*. **1982**, 851.

(60) Höfs, H.U.; Bats, J.W.; Gleiter,R.; Hartmann, G. Mews, R.; Eckert M.; Maksić.; Oberhammer, H.; Sheldrick, G.M. *Chem. Ber.,* **1985**, 118.

(61) Haynes, D.A.; *CrystEngComm*, **2011**, 13.

(62) (a) Vegas, A.; Perezsalazar, A.; Banister, A. J.; Hey, R. G. *J. Chem. Soc., Dalton Trans.*, **1980**, 1812. (b) Cordes, A. W.; Bryan, C. D.; Davis, W. M.; Delaat, R. H.; Glarum, S. H.; Goddard, J. D.; Haddon, R. C.; Hicks, R. G.; Kennepohl, D. K.; Oakley, R. T.; Scott S. R.; Westwood, N. P. C. *J. Am. Chem. Soc.* **1993**, 115, 7232. (c) Cordes, A. W.; Haddon, R. C.; Hicks, R. G.; Kennepohl, D. K.; Oakley, R. T.; Palstra, T. T. M.; Schneemeyer, L. F.; Scott, S. R.; Waszczak, J. V. *Chem. Mater.* **1993**, 5, 820. (d) Cordes, A. W.; Haddon, R. C.; Hicks, R. G.; Kennepohl, D. K.; Oakley, R. T.; Schneemeyer, L. F.; Waszczak, J. V. *Inorg. Chem.* **1993**, 32, 1554. (d) Bryan, C. D.; Cordes, A. W.; Haddon, R. C.; Hicks, R. G.; Oakley, R. T.; Palstra, T. T. M.; Perel, A. J. *J. Chem. Soc., Chem. Commun.* **1994**, 1447. (e) Clarke, C. S.; Haynes, D. A.; Rawson, J. M.; Bond, A. D. *Chem. Commun.* **2003,** 2774.

(63) Cordes, A. W.; Haddon, R. C.; Hicks, R. G.; Oakley, R. T.; Palstra, T. T. M. *Inorg. Chem*. **1992**, 31, 1802.

(64) (a) Hofs, H. U.; Bats, J. W.; Gleiter, R.; Hartmann, G.; Mews, R.; Eckertmaksic, M.; Oberhammer, H.; Sheldrick, G. M. *Chem. Ber.* **1985**, 118, 3781. (b) Banister, A. J.; Hansford, M. I.; Hauptman, Z. V.; Wait, S. T.; Clegg, W. *J. Chem. Soc., Dalton Trans.* **1989**, 1705. (c) Cordes, A. W.; Goddard, J. D.; Oakley, R. T.; Westwood, N. P. C*. J. Am. Chem. Soc.* **1989**, 111, 6147.

(65) Cordes, A. W.; Haddon, R. C.; Hicks, R. G.; Oakley, R. T.; Palstra, T. T. M. *Inorg. Chem.* **1992**, 31, 1802.

(66) Barclay, T. M.; Cordes, A. W.; George, N. A.; Haddon, R. C.; Itkis, M. E.; Oakley, R. T. *Chem. Commun.* **1999**, 2269.

(67) Britten, J.F. Clements, O.P.; Cordes, A.W.; Haddon, R.C.; Oakley, R.T.; Richardson, J.F.; *Inorg Chem.* **2001.** 40, 6820.

(68) Feeder, N.; Less, R. J.; Rawson, J. M.; Oliete, P.; Palacio, F. *Chem. Commun*. **2000**, 2449.

(69) Awere, E. G.; Burford, N.; Mailer, C.; Passmore, J.; Schriver, M. J.; White, P. S.; Banister, A. J.; Oberhammer, M.; Sutcliffe, L. H. *J. Chem. Soc., Chem. Commun.* **1987**, 66.

(70) Barclay, T. M.; Cordes, A. W.; George, N. A.; Haddon, R. C.; Oakley, R. T.; Patenaude, G. W.; Reed, R. W.; Zhang, H. *J. Chem. Soc., Chem Commun.* **1997**, 873.

(71) (a) Mayer, R., Domschke, G., Bleisch, S., and Bartl, A. *Tetrahedron Lett.* **1978**, 4003. (b) Mayer, R., Domschke, G., Bleisch, S., Bartl, A., and Stãsko, A. *Z. Chem.* **1981**, 21, 146; *Z. Chem.* **1981**, 21, 264. (c) Mayer, R., Domschke, G., Bleisch, S., Fabian, J., Bartl, A., and Stãsko, A. *Collect. Czech. Chem. Commun.* **1984**, 49, 684. (d) Mayer, R., Bleisch, S., Domschke, G., Tkáè, A., Stãsko, A., and Bartl, A. *Org. Magn. Reson.* **1979**, 12, 532. (e) Tsveniashvili, V. Sh. *Collect. Czech. Chem. Commun*. **1982**, 47, 203. (f) Harrison, S. R., Pilkington, R. S., and Sutcliffe, L. H. *J. Chem. Soc., Faraday Trans.* 1 **1984**, 80, 669. (g) Preston, K. F. and Sutcliffe, L. H. *Magn. Reson. Chem*. **1990**, 28, 189. (h) Bagryansky, V. A., Vlasyuk, I. V., Gatilov, Y. V., Makarov, A. Y., Molin, Y. N., Shcherbukhin, V. V., and Zibarev, A. V. *Mendeleev Commun.* **2000**, 10, 5.

(72) Risto, M.; Assoud, A.; Winter, S. M.; Oilunkaniemi, R.; Laitinen, R. S.; Oakley, R. T. *Inorg. Chem.* **2008**, 47, 10100.

(73) Barclay, T. M.; Beer, L.; Cordes, A. W.; Oakley, R. T.; Preuss, K. E.; Taylor, N. J.; Reed, R. W. *Chem. Commun.* **1999**, 531.

(74) Beer, L.; Cordes, A. W.; Haddon, R. C.; Itkis, M. E.; Oakley, R. T.; Reed, R. W.; Robertson, C. M. *Chem. Commun.* **2002,** 1872.

(75) Robertson, C.M.; Leitch, A.A; Cvrkalj, K.; Reed, R.W.; Myles, D.J.T.; Dube, P.A.; Oakley, R.T. *J. Am. Chem.Soc.* **2008**, 130, 8414. (b) Robertson, C.M.; Leitch, A.A; Cvrkalj, K.; Myles, D. J.T.; Reed, R.W.; Dube, P.A.; Oakley, R.T. *J. Am. Chem.Soc.* **2008**, 130, 14791.

(76) Mito, M.; Komorida, Y.; Tsuruda, H. Tse, J.S.; Desgreniers, S.; Ohishi, Y.; Leitch A.A.; Cvrkalj, K.; Robertson, C.M.; Oakley, R.T.; *J. Am. Chem. Soc.,* **2009**, 131, 16012.

(77) Leitch, A. A.; McKenzie, C. E.; Oakley, R. T.; Reed, R. W.; Richardson, J. F.; Sawyer, L. D. *Chem. Commun*. 2006, 1088.

(78) Leitch, A. A.; Reed, R. W.; Robertson, C. M.; Britten, J. F.; Yu, X.; Secco, R. A.; Oakley, R. T. *J. Am. Chem. Soc*. 2007, 129, 7903.

(79) Yu, X.; Mailman, A.; Dube, P. A.; Assoud, A.; Oakley, R. T. *Chem. Commun*. **2011**, 47, 4655. (b) Yu, X.; Mailman, A.; Dube, P. A.; Assoud, A.; Oakley, R. T. *Chem. Commun*. **2011**, 47, 4655. (c) Yu, X.; Mailman, A.; Lekin, K.; Assoud, A.; Robertson, C. M.; Noll, B. C.; Campana, C. F.; Howard, J. A. K.; Dube, P. A.; Oakley, R. T. *J. Am. Chem. Soc*. **2012**, 134, 2264. (d) Mailman, A.; Winter, S. M.; Yu, X.; Robertson, C. M.; Yong, W.; Tse, J. S.; Secco, R. A.; Liu, Z.; Dube, P. A.; Howard, J. A. K.; Oakley, R. T. *J. Am. Chem. Soc*. **2012**, 134, 9886. (e) Wong, J. W. L.; Mailman, A.; Winter, S. M.; Robertson, C. M.; Holmberg, R. J.; Murugesu, M.; Dube, P. A.; Oakley, R. T. *Chem. Commun*. **2014**, 50, 785.

(80) Desiraju, G. R. *Angew. Chem., Int. Ed. Engl.* **1995**, 34, 2311.

(81) Yu, X.; Mailman, A.; Dube, P. A.; Assoud, A.; Oakley, R. T. *Chem. Commun*. **2011**, 47, 4655.

(82) Yu, X.; Mailman, A.; Lekin, K.; Assoud, A.; Robertson, C. M.; Noll, B. C.; Campana, C. F.; Howard, J. A. K.; Dube, P. A.; Oakley, R. T. *J. Am. Chem. Soc*. **2012**, 134, 2264.

(83) Yu, Xin.; Mailman, A.; Lekin, K.; Assoud, A.; Dube, P.A.; Oakley, R,T.; *Cryst. Growth. Des.* **2012**, 12, 2485.

(84) Mailman, A.; Winter, S. M.; Yu, X.; Robertson, C. M.; Yong, W.; Tse, J. S.; Secco, R. A.; Liu, Z.; Dube, P. A.; Howard, J. A. K.; Oakley, R. T. *J. Am. Chem. Soc*. **2012**, 134, 9886.

References for Chapter 2

(1) J. S. Miller, Adv. Mater., 1994, 6, 322–324; Stable Radicals: Fundamental and Applied Aspects of Odd-Electron Compounds, ed. R. G. Hicks, John Wiley & Sons, Chichester, West Sussex, UK, 2010.

(2) Peierls, R. C. Quantum Theory of Solids; Oxford University Press: London, U. K., **1955**, pp 108.

(87) Britten, J.F.; Clements, O, P.; Cordes, A.W.; Haddon, R,C.; Oakley, R.T.; Richardson, J.F. *Inorg. Chem.,* **2001**, 40, 6820.

(3) Vegas, A.; Pérez-Salazar, A.; Banister, A.J.; Hey, R.G. *J. Chem. Soc., Dalton Trans.,* **1980**, 1812.

(4) Höfs, H.U.; Bats, J.W.; Gleiter,R.; Hartmann, G. Mews, R.; Eckert M.; Maksić.; Oberhammer, H.; Sheldrick, G.M. Chem. Ber., 1985, 118.

(5) Cordes, A.W.; Goddard, J.D.; Oakley, R.T.; Westwood, N.P.C. *J.Am.Chem.Soc,* **1989**, 111, 6147.

(6) Bridson, J.N.; Copp, S.B.; Schriver, M.J.; Zhu, S.; Zaworotko, M.J. *Can. J. Chem.,* **1994**, 72, 1143.

(7) Schlemper, E.O.; Britton, D. *Acta Crystallogr.,* **1965**, 18, 419.

(8) Heiart, R.B.; Carpenter, G.B. *Acta Crystallogr.,* **1956**, 9, 889.

(9) Cordes, A.W.; Haddon, R.C.; Hicks, R.G.; Oakley, R.T.; Palstra, T.T.M.; *Chem. Commun.* **2000**, 2449.

(10) (a) Shuvaev, K.V.; Decken, A.; Grein, F. Abedin, T.S.M.; Thompson, L.K., Passmore, J. *Dalton Trans.,* 2008, 4029. (b) Lau, H.F.; Ng, V.W.L.; Koh, L.; Tan, G.K.; Goh, L.Y.; Roemmele, T.L.; Seagrave, S.D.; Boeré, R.T. *Angew. Chem. Int. Ed.,* 2006, 4498. (c) Hearns, N.G.R.; Clérac, R.; Jennings, M.; Preuss, K.E. *Dalton Trans.,* **2009**, 3193.

(11) Banerjee, Anamitro and Ngwendson, Julis N. US 20070179311 A1 (2007).

References for Chapter 3

(1) Yu, X.; Mailman, A.; Dube, P. A.; Assoud, A.; Oakley, R. T. *Chem. Commun.* **2011**, 47, 4655. (b) Yu, X.; Mailman, A.; Lekin, K.; Assoud, A.; Robertson, C. M.; Noll, B. C.; Campana, C. F.; Howard, J. A. K.; Dube, P. A.; Oakley, R. T. *J. Am. Chem. Soc.* **2012**, 134, 2264. (c) Yu, Xin.; Mailman, A.; Lekin, K.; Assoud, A.; Dube, P.A.; Oakley, R,T.; *Cryst. Growth. Des*. **2012**, 12, 2485. (d) Mailman, A.; Winter, S. M.; Yu, X.; Robertson, C. M.; Yong, W.; Tse, J. S.; Secco, R. A.; Liu, Z.; Dube, P. A.; Howard, J. A. K.; Oakley, R. T. *J. Am. Chem. Soc.* **2012**, 134, 9886.

(2) Desiraju, G. R. *Angew. Chem. Int. Ed. Engl.* **1995**, 34, 2311.

(3) (a) Wong, J. W. L.; Mailman, A.; Winter, S. M.; Robertson, C. M.; Holmberg, R. J.; Murugesu, M.; Dube, P. A.; Oakley, R. T. *Chem. Commun.* **2014**, 50, 785. (b) Wong. J.W.L.; Mailman. A.; Lekin, K.; Winter, S.M.; Yong, W.; Zhao, J.; Garimella, S.V.; Tse, J.S.; Secco, R.A.; Desgreniers, S.; Ohishi, Y.; Borondics, F.; Oakley, R.T. *J. Am. Chem. Soc.* **2014**, 136, 1070.

(4) J. M. D. Coey, Magnetism and Magnetic Materials, Cambridge. University Press, **2010**.

(5) (a) S. M. Winter, K. Cvrkalj, P. A. Dube, C. M. Robertson, M. R. Probert, J. A. K. Howard and R. T. Oakley, *Chem. Commun*., **2009**, 7003; (b) W. Fujita, K. Takahashi and H. Kobayashi, *Cryst. Growth Des*., **2011**, 11, 575. (c) H. Nagashima, S. Fujita.; H. Inoue.; N. Yoshioka. *Cryst. Growth Des.*, **2004**, 4, 19; (d) Ishida, T.; Tomioka, K.; Nogami, T.; Yoshikawa, H.; Yasui, M.; Iwasaki, F.; Takeda, N.; Ishikawa, M. *Chem. Phys. Lett*., **1995**, 247,7.

(6) (a) Catilla, G.; Chakravarty, S.; Emery, V.J. *Phys. Rev. Lett., **1995,*** 75, 1823. (b) Hase, M.; Kuroe, H.; Ozawa, K.; Suzuki, O.; Kitazawa, H.; Kido, G.; Sekine, T. *Phys. Re. B: Condens. Matter Mater Phys.,* **2004**, 70, 104426. (c) Kumar, M.; Dutton, S.E.; Cava, R.J.; Soos, Z.G.; *J. Phys. Condens. Matter,* **2013**, 25, 136004.

(7) Rietveld, H.M. *J. Appl. Cryst.* **1969**, 2, 65.

(8) Le Bail, A. *Powder Diffraction*, **2005**, 20, 4.

(9) (a) Dumm, M.; Faltermeier, D.; Drichko, N.; Dressel, M.; Meziere, C.; Batail, P. *Phys. Rev. B*. **2009**, 79, 195106. (b) Faltermeier, D.; Barz, J.; Dumm, M.; Dressel, M.; Drichko, N.; Petrov, B.; Semkin, V.; Vlasova, R.; Meziere, C.; Batail*, P. Phys. Rev. B.* **2007**, 76, 165113.

(10) Merino, J.; Mackenzie, R. H. *Phys. Rev. B.* **2000**, 61, 7996.

(11) Harrison, S. R.; Pilkington, R. S.; Sutcliffe, L. H. *J. Chem. Soc*., *Faraday Trans. 1* **1984**, 80, 669. (b) Preston, K. F.; Sutcliffe, L. H. *Magn. Reson. Chem*. **1990**, 28, 189 (c) Barclay, T. B.; Beer, L.; Cordes, A. W.; Oakley, R. T.; Preuss, K. E.; Taylor, N. J.; Reed, R. W. Chem. Commun. **1999**, 531

(12) (a) Constantinides, C. P.; Koutentis, P. A.; Schatz, J. *J. Am. Chem. Soc*. **2004**, 126, 16232. (b) Constantinides, C. P.; Ioannou, T. A.; Koutentis, P. A. *Polyhedron* **2013**, 64, 172. (c) Langer, P.; Amiri, S.;

Bodtke, A.; Saleh, N. N. R.; Weisz, K.; Gorls, H.; Schreiner, P. R. *J. Org. Chem*. **2008**, 73, 5048. (d) Amiri, S.; Schreiner, P. R. *J Phys. Chem. A* 2009, 113, 11750. (e) Barone, V.; Boilleau, C.; Cacelli, I.; Ferretti, A.; Monti, S.; Prampolini, G. *J. Chem. Theory Comput.* **2013**, 9, 300. (f) Winter, S. M.; Roberts, R. J.; Mailman, A.; Cvrkalj, K.; Assoud, A.; Oakley, R. T. *Chem. Commun*. **2010**, 46, 4496.

(13) Cordes, A.W.; Goddard, J.D.; Oakley, R.T.; Westwood, N.P.C. *J. Am. Chem. Soc.* **1989**, 111, 6147.

(14) (a) Kino, H.; Fukuyama, h. *J. Phys. Soc. Jpn.* **1996**, 65, 2158. (b) McKenzie, R. H.; *Comments Cond. Matt. Phys.* **1998**, 18, 309. (c) Toyota, N.; Lang, M.; Muller. *Low-Dimensional Molecular Metals;* Springer: Berlin, **2007**.

(15) (a) Goodenough, J.B. *Phys. Rev.* **1955**, 100,564. (b) Kahn, O. *Molecular Magnetism;* VCH publications, Inc.: New York, **1993**, p 199.

(16) Jaramillo, R.; Sieu, D.H.; Silevitch, D.M.; Ramanathan, S. *Nature Physics.* **2014**, 1.

(17) Banerjee *et. al*. US 0179311 A1 (**2007**).

References for Chapter 4

(1) (a) Wong, J.W.L.; Mailman, A.; Lekin, K.; Winter, S.M.; Yong, W.; Zhao, J.; Garimella, S.V.; Tse, J.S.; Secco, R.A.; Desgreniers, S. Ohishi, F.; Borondics, F. and Oakley, R.T. *J. Am. Chem. Soc.* **2014**, 136, 1070. (b) Mailman, A.; Winter, S.M.; Yu, X.; Robertson, C.M.; Yong, W.; Tse, J.S.; Secco, R.A.; Liu, Z.; Dube, P.A.; Hward, J.A.K. and Oakley, R.T. *J. Am. Chem. Soc.* **2012**, 134, 9886.

(2 (a) Lam, W. W.; Martin, G. E.; Lynch, V. M.; Simonsen, S. H.; Lindsay, C. M.; Smith, K. *J. Heterocycl. Chem.* **1986**, 23, 785–791. (b) Okafor, C. O., *J. Org. Chem*. **1967**, 32, 2006-2007.

(3) Kempson, J.; Spergel, S.H.; Guo, J.; Quesnelle, C.; Gill, P.f; Belanger, D.; Dyckman, A.J.; Li, T.; Watterson, S.H.; Langevine, C.M.; Das, J.; Moquin, R.V.; Furch, J.A.; Marinier, A.; Dodier, M.; Martel, A.; Nirschl, D.; Kirk, K.V.; Burke, J.R.; Pattoli, M.A.; Gillooly, K.; McIntyre, K.W.; Chen, K.; Yang, Z.; Marathe, P.H.; Wang-Iverson, D.; Dodd, J.H.; McKinnon, M.; Barrish, J.C. and Pitts, W.J. *J. Med. Chem.* **2009**, 52, 1994-2005. (b) Rycke, N. D.; Berionni, G.; Couty, F.; Mayr, H.; Goumont, R.; David, O.R.P. *Org. Lett.* **2011**, 13, 530-533.

(4) Bemporad, P.; Illuminati, G.; Stegel, F. *J. Am. Chem. Soc.* **1969**, 6742-6745.

(5) Provencal, D. P.; Gesenberg, K.D.; Wang, H.; Escobar, C.; Wong, H.; Brown, M.A.; Staab, A.J.; Pendri, Y.R. *Organic Process Research & Development*. **2004**, 8, 903 – 908.

(1) Hay, D. A.; Adam, F.M.; Bish, G.; Calo, F.; Dixon, R.; Fray, M.J.; Hitchin, J.; Jones, P.; Paradowski, M.; Parsons, G.C.; Proctor, K. J.W.; Pryde, D.C.; Smith, N.N.; Tran, T. *Tetrahedron Letters***. 2011**, 52, 5728-5732.

(6) (a) Waki, M.; Abe, H.; Inouye, M. *Chem. Eur. J.* **2006**, 12, 7839-7847. (b) Inouye, M.; Takahashi, K.; Nakazumi, H. *J. Am. Chem. Soc.* **1999**, 121, 341-345.

(7) Coburn, M.D.; Singleton, J.L. *J. Heterocycl. Chem.* **1972**, 9, 1039-1044.

(8) Krasnokutskaya, E.A.; Semenischeva, N.I.; Filimonov, V.D.; Knochel, P. *Synthesis*. **2007**, 1, 81-84.

References for Chapter 5

(1) Torrance, J.B.; *Acc. Chem. Res.* **1979**, 12, 79.

(2) (a) Lekin, K.; Winter, S.M.; Downie, L.E.; Bao,X.; Tse, J.S.; Desgreniers, S.; Secco, R.A.; Dube, P.A.; Oakley, R.T. *J. Am. Chem. Soc* **2010**. 132, 16212-16224. (b) Lekin, K.; Wong, J.W.L.; Winter, S.M.; Mailman, A.; Dube, P. A.; Oakley, R.T. **2013**. *Inorg. Chem.* 2188-2198. (c) Brusso, J.L.; Cvkalj, K.; Leitch, A.A.; Oakley, R.T.; Reed, R.W.; Robertson, C.M. *J .Am.Chem.Soc.* **2006**, 128, 15080-15081.

(3) Yu, X.; Mailman, A.; Dube, P. A.; Assoud, A.; Oakley, R. T. *Chem. Commun*. **2011**, 47, 4655. (b) Yu, X.; Mailman, A.; Lekin, K.; Assoud, A.; Robertson, C. M.; Noll, B. C.; Campana, C. F.; Howard, J. A. K.; Dube, P. A.; Oakley, R. T. *J. Am. Chem. Soc*. **2012**, 134, 2264. (c) Yu, Xin.; Mailman, A.; Lekin, K.; Assoud, A.; Dube, P.A.; Oakley, R,T.; *Cryst. Growth. Des.* **2012**, 12, 2485. (d) Mailman, A.; Winter, S. M.; Yu, X.; Robertson, C. M.; Yong, W.; Tse, J. S.; Secco, R. A.; Liu, Z.; Dube, P. A.; Howard, J. A. K.; Oakley, R. T. *J. Am. Chem. Soc.* **2012**, 134, 9886.

(4) English, J. Jr.; Mead, J.F.; and Niemann, C. *Contributed from the Gates and Crellin Laboratories of Chemistry, California Institute of Technology.* **1940**, 62, 351.

(5) Konrad, E.; and Clausen, D. *process for production of aromatic homo cyclic or heterocyclic amino-nitro compounds.* German Patent, 33 28 002.

(6) Beer, L.; Cordes, A. W.; Haddon, R. C.; Itkis, M. E.; Oakley, R. T.; Reed, R. W.; Robertson, C. M. *Chem. Commun.* **2002**, 1872.

(7) (a) Boeré, R. T.; Roemmele, T. L. Coord. *Chem. Rev.* **2000**, 210, 369.(b) Boeré, R. T.; Moock, K. H. *J. Am. Chem. Soc.* **1995**, 117, 4755.

(8) (a) Robertson, C. M.; Leitch, A. A.; Cvrkalj, K.; Reed, R. W.; Myles, D. J. T.; Dube, P. A.; Oakley, R. T. *J. Am. Chem. Soc.* **2008**, 130, 8414. (b) Reported as −0.02 V vs SCE by: Hobi, M.; Ruppert, O.; Gramlich, V.; Togni, A. *Organometallics* **1997**, 16, 1384.

(9) Reported as 0.241 V vs SCE by: Hoh, G. L. J.; McEwen, W. E.; Kleinberg, J. *J. Am. Chem. Soc.* **1961**, 83, 3949.

References for Appendix A

(1) (a) Beck, A. D. J. Chem. Phys., 1993, 98, 5648. (b) Lee, C.; Yang, W.; Parr, R. C. *Phys. Chem. Rev. B*, **1988**, 37, 785.

(2) Frisch, M. J.; Trucks, G. W.; Schlegel, H. B.; Scuseria, G. E.; Robb, M. A.; Cheeseman, J. R.; Zakrzewski, V. G.; Montgomery Jr., J. A.; Stratmann, R. E.; Burant, J. C.; Dapprich, S.; Millam, J. M.; Daniels, A. D.; Kudin, K. N.; Strain, M. C.; Farkas, O.; Tomasi, J.; Barons, V.; Cossi, M.; Cammi, R.; Mennucci, B.; Pomelli, C.; Adamo, C.; Clifford, S.; Ochterski, J.; Petersson, G. A.; Ayala, P. Y.; Cui, Q.; Morokuma, K.; Malick, D. K.; Rabuck, A. D.; Raghavachari, K.; Foreman, J. B.; Cioslowski, J.; Ortiz, J. V.; Stefanov, B. B.; Liu, G.; Fox, D. J.; Keith, T.; Al-Laham, M. A.; Peng, C. Y.; Nanayakkara, A.; Wong, M. W.; Andres, J. L.; Gonzalez, C.; Head-Gordon, M.; Repogle, E. S.; Pople, J. A. Gaussian 98, Revision A:6. Gaussian, Inc.: Pittsburg, PA, **1998**.

(3) Gaussian 09, Revision A.02, Frisch, M. J.; Trucks, G. W.; Schlegel, H. B.; Scuseria, G. E.; Robb, M. A.; Cheeseman, J. R.; Scalmani, G.; Barone, V.; Mennucci, B.; Petersson, G. A.; Nakatsuji, H.; Caricato, M.; Li, X.; Hratchian, H. P.; Izmaylov, A. F.; Bloino, J.; Zheng, G.; Sonnenberg, J. L.; Hada, M.; Ehara, M.; Toyota, K.; Fukuda, R.; Hasegawa, J.; Ishida, M.; Nakajima, T.; Honda, Y.; Kitao, O.; Nakai, H.; Vreven, T.; Montgomery, Jr., J. A.; Peralta, J. E.; Ogliaro, F.; Bearpark, M.; Heyd, J. J.; Brothers, E.; Kudin, K. N.; Staroverov, V. N.; Kobayashi, R.; Normand, J.; Raghavachari, K.; Rendell, A.; Burant, J. C. Iyengar, S. S.; Tomasi, J.; Cossi, M.; Rega, N.; Millam, N. J.; Klene, M.; Knox, J. E.; Cross, J. B.; Bakken, V.; Adamo, C.; Jaramillo, J.; Gomperts, R.; Stratmann, R. E.; Yazyev, O.; Austin, A. J.; Cammi, R.; Pomelli, C.; Ochterski, J. W.; Martin, R. W.; Morokuma, K.; Zakrzewski, V. G.; Voth, G., A.; Salvador, P.; Dannenberg, J. J.; Dapprich, S.; Daniels, A. D.; Farkas, O.; Foresman, J. B.; Ortiz, J. V.; Cioslowski, J.; Fox, D. J., Gaussian, Inc., Wallingford CT, **2009**.

(4) Boeré, R. T.; Moock, K. H.; Parvez, M. Z. *Anorg. Allg. Chem*., **1994**, 620, 1589.

(5) WinEPR Simfonia, version 1.25; Bruker Instruments, Inc.: Billerica, MA, **1966**.

(6) Carlin, R. L. Magnetochemistry; Springer-Verlag: New York, **1986**.

(7) SAINT, version 6.22; Bruker Advanced X-ray Solutions, Inc.: Madison, WI, **2001**.

(8) Sheldrick, G. M. SHELXS-90. *Acta Crystallogr.* A **1990**, 46, 467.

(9) Sheldrick, G. M. SHELXL-97. Program for the Refinement of Crystal Structures; University of Göttingen, Göttingen, Germany, **1997**.

(10) SHELXTL, VERSION 6.12 Program Library for Structure Solution and Molecular Graphics; Bruker Advanced X-ray Solutions, Inc.: Madison, WI, **2001**.

(11) CrystalClear; Rigaku Corporation: Tokyo, Japan, **2005**.

(12) SADABS; Bruker AXS Inc.: Madison, WI, **2001**.